

Lawrence Berkeley National Laboratory

Recent Work

Title

Phase Transitions and Equation of State of CsI under High Pressure and the Development of a Focusing System for X-Rays

Permalink

<https://escholarship.org/uc/item/8wx6k2gk>

Author

Wu, Y.

Publication Date

1990-11-01



Lawrence Berkeley Laboratory

UNIVERSITY OF CALIFORNIA

Accelerator & Fusion Research Division

Center for X-Ray Optics

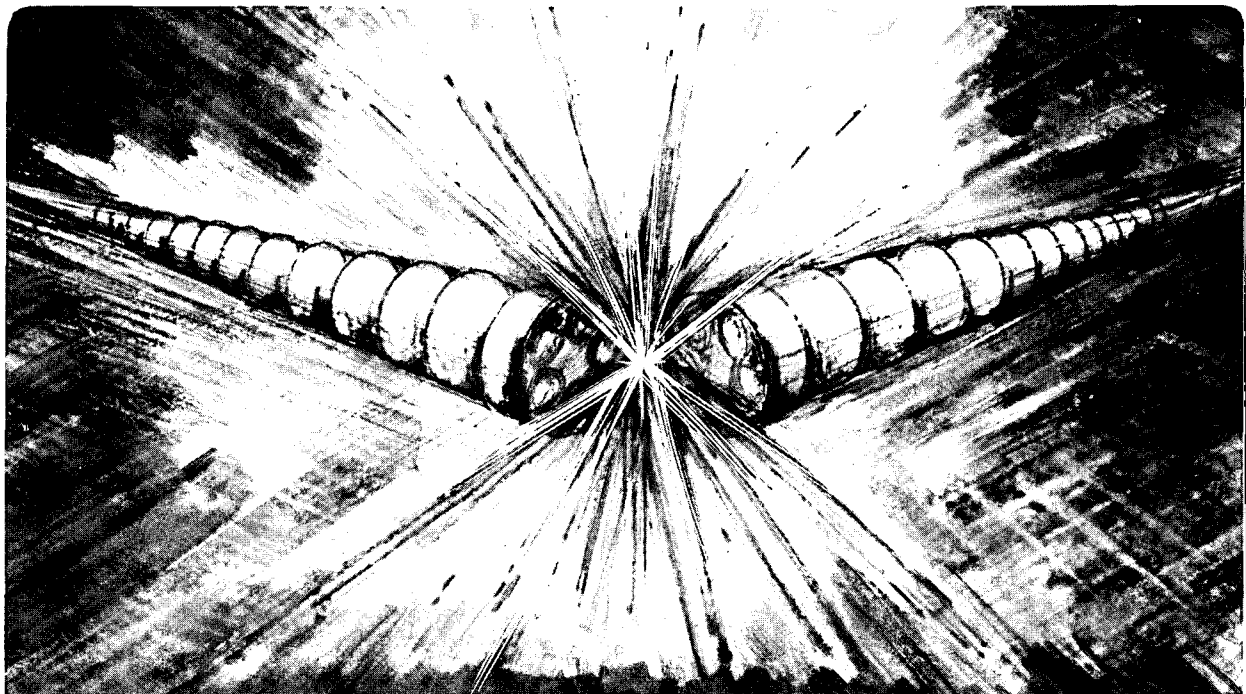
**Phase Transitions and Equation of State of CsI
under High Pressure and the Development of a
Focusing System for X-Rays**

Y. Wu
(Ph.D. Thesis)

November 1990

For Reference

Not to be taken from this room



LBL-29844
Copy 1
Bldg. 50 Library.

DISCLAIMER

This document was prepared as an account of work sponsored by the United States Government. While this document is believed to contain correct information, neither the United States Government nor any agency thereof, nor the Regents of the University of California, nor any of their employees, makes any warranty, express or implied, or assumes any legal responsibility for the accuracy, completeness, or usefulness of any information, apparatus, product, or process disclosed, or represents that its use would not infringe privately owned rights. Reference herein to any specific commercial product, process, or service by its trade name, trademark, manufacturer, or otherwise, does not necessarily constitute or imply its endorsement, recommendation, or favoring by the United States Government or any agency thereof, or the Regents of the University of California. The views and opinions of authors expressed herein do not necessarily state or reflect those of the United States Government or any agency thereof or the Regents of the University of California.

LBL-29844

Phase Transitions and Equation of State of CsI under High
Pressure and the Development of a Focusing System for X-rays

Yan Wu
Ph.D. Thesis

Accelerator and Fusion Research Division
Lawrence Berkeley Laboratory
University of California
Berkeley, CA 94720

November 1990

This work was supported by the U.S. Department of Energy under
Contract No. DE-AC03-76SF00098.

Phase Transitions and Equation of State of CsI under High Pressure and the Development of a Focusing System for X-rays

By
Yan Wu

ABSTRACT

The phase transitions and equation of state of ionic solid cesium iodide were studied under high pressure and room temperature in a diamond anvil cell. The studies were carried out using both energy dispersive and angular dispersive diffraction methods on synchrotron radiation sources over the pressure range from atmospheric pressure to over 300 gigapascals (3 million atmospheres). CsI undergoes a distinct phase transition at about 40 GPa, a pressure that is much lower than the reported insulator-metal transition at 110 GPa, from the atmospheric pressure B2(CsCl) structure to an orthorhombic structure. At higher pressures, a continuous distortion in the structure was observed with a final structure similar to a hcp lattice under ultra high pressure. No volume discontinuity was observed at the insulator-metal transition.

Using an ionic pair potential model, the phase transition sequence can be explained as a result of a continuous change of the relative strength of the repulsive interaction due to charge overlapping and the attractive Coulomb interaction. Such a transition sequence is expected to be rather general and should occur in other heavy ionic solids as well.

The newly found transition sequence is different from the result of previous static compression studies. The current structure has a smaller unit cell volume than the previous assignment. This has resolved a long existing controversy among

the previous static compression studies, the dynamic compression studies, and the theoretical studies. The current results also explain the apparent discrepancy between the present study and the previous static studies. Therefore, all previous static, dynamic compression studies and also existing theoretical calculations are now in good agreement with each other.

We also present the development of a focusing system for high energy x-rays (> 12 keV) that is particularly suited for high pressure diffraction studies. This system uses a pair of multilayer coated spherical mirrors in a Kirkpatrick-Baez geometry. A focused beam size less than 10 micron in diameter can be readily achieved with sufficient intensity to perform diffraction studies. Such a system extends the high pressure x-ray diffraction studies in two regards. (1) The possibility of achieving an even smaller beam size without much loss in intensity will enable study of materials at ultra high pressures. (2) The resolution offered by this method is several times better than currently available methods and therefore will greatly widen the materials and phenomena that can be studied.

Dedication

To Diane

Contents

1	Introduction	1
2	Diamond Anvil Cell Technique in High Pressure Structural Studies	4
2.1	Generation of high pressures using diamond anvil cells	4
2.2	Pressure measurement	14
3	X-ray Diffraction Methods in High Pressure Studies	18
3.1	Scattering by a single electron	18
3.2	Scattering by an atom: coherent and incoherent scattering	20
3.3	Scattering by crystals	23
3.3.1	The Bragg law of diffraction	23
3.3.2	Integrated intensities	24
3.4	A comparison of EDXD and ADXD methods	26
3.4.1	Resolution	27
3.4.2	Intensity	29
3.5	Experimental setup for studies of crystal structures under high pressure	31
3.5.1	EDXD method	32
3.5.2	ADXD method	40
3.6	Data reduction	41

4	The Development of a Focusing System for X-rays	43
4.1	The requirement for a small beam size in high pressure studies	44
4.2	Advantages of using a focusing system	46
4.3	Focusing optics in the x-ray region	48
4.3.1	Fresnel zone plate focusing system	50
4.3.2	Focusing using crystals	50
4.3.3	Focusing using total reflection mirrors	52
4.3.4	A new possibility: focusing using multilayer coated mirrors . . .	53
4.4	An introduction to reflective optics	54
4.5	Multilayer reflective coatings for x-rays	57
4.5.1	Principles	58
4.5.2	Design and fabrication	59
4.6	The design and operation of the K-B focusing system	63
4.7	The performance of the x-ray focusing system	65
4.8	Applications to diffraction studies under high pressure	66
4.8.1	Ultra high pressure studies	68
4.8.2	High resolution studies	74
4.8.3	Effect of beam size on the quality of diffraction patterns	75
4.9	Conclusions and suggestions for further studies	78
5	On the Structure and Equation of State of CsI under High Pressure	82
5.1	Introduction	82
5.2	Previous studies on properties of CsI under high pressure	85
5.3	Experimental	89
5.4	Results	91

5.4.1	Crystal structure of CsI under ultra high pressures	91
5.4.2	Crystal structures of CsI in the intermediate pressure range	96
5.4.3	Nature of the phase transition in the low pressure range	103
5.5	Equation of State (EOS) of CsI	113
5.5.1	Quasi-hydrostatic compression and non-hydrostatic compression: comparisons with previous static compression studies	113
5.5.2	Implication to the validity of various EOS formulations at ultra high pressures	119
5.5.3	Comparison with previous studies	128
5.5.4	Implications to the insulator-metal transition	135
5.5.5	Comparison of EOS of CsI with that of Xe and BaTe	141
5.6	An ionic model for phase transitions of CsI under pressure	150
5.6.1	The pair potential model	150
5.6.2	Calculated phase transitions	154
5.6.3	Comparison with the experimental results	155
5.6.4	The nature of the phase transition	161
5.7	Conclusion	165

A Equation of State Fitting Procedure 167

List of Figures

2.1	A picture of a typical diamond anvil cell used in high pressure studies	7
2.2	Schematic drawing of the diamond anvils	9
3.1	Schematic of the Energy Dispersive X-ray Diffraction setup	33
3.2	Photographs of one of the EDXD experimental setup used in our studies	37
4.1	A typical pressure profile in ultra high pressure studies	45
4.2	Comparison of the allowable acceptance with the characteristics of the SSRL beamline VI synchrotron source in phase space	47
4.3	Comparison of the effective acceptance provided by a 10 μm pinhole with a focusing system	49
4.4	Focusing properties of a reflective concave spherical surface	56
4.5	Schematic drawing of the cross section of an ideal multilayer reflector for x-rays	60
4.6	Reflectivity versus glancing angle ($\times 2$) for a tungsten-carbon multi- layer mirror	61
4.7	Experimental setup for ADXD study on materials under very high pressure using the focusing device	67
4.8	Pictures of the ADXD experimental setup	71
4.9	A diffraction pattern of Fe under ultra high pressure recorded on an imaging plate	73

4.10	A high resolution diffraction pattern of CsI under quasi-hydrostatic pressure	77
4.11	The effect of beam size on the quality of diffraction patterns	80
5.1	An energy dispersive diffraction pattern of CsI under a pressure of 295 GPa	92
5.2	The variation of lattice spacings as a function of pressure for CsI in the ultra high pressure range	94
5.3	A series of diffraction patterns of CsI under increasing pressures	97
5.4	The result of a deconvolution shows five peaks in the region where the (110) of the B2 structure should occur	98
5.5	The orthorhombic unit cell of CsI under high pressure and its relation to the low pressure B2 and the ultra high pressure hcp structure	100
5.6	The (110) diffraction peak width (FWHM) of CsI as a function of pressure	106
5.7	A comparison of isothermal bulk moduli of CsI and Ne under high pressure	108
5.8	A series of angular dispersive x-ray diffraction patterns of CsI under different pressures	110
5.9	The identification of diffraction lines	111
5.10	Diffraction pattern of CsI at 26 GPa recorded on an imaging plate	112
5.11	Quasi-hydrostatic compression data of CsI	116
5.12	Non-hydrostatic compression data of CsI	118
5.13	Comparison of weighted least squares fits to the experimental data under 100 GPa with three different EOS formulas	123
5.14	Comparison of weighted least square fits to our experimental data up to 300 GPa with three different EOSes	124

5.15	Extrapolation property of the three EOSes	126
5.16	Comparison of calculated EOSes based on the ultrasonic values for the bulk modulus and its pressure derivatives with experimental data	127
5.17	The parameters for calculating zero point and thermal pressures in cesium iodide	131
5.18	Calculated zero point pressure plus thermal pressure as a function of static pressure	132
5.19	Comparison of the current equation of state data with various first principle theoretical calculations	134
5.20	Comparison of shock wave Hugoniot data with the low temperature isotherms and calculated Hugoniot obtained from the current study .	136
5.21	The polarizability as a function of frequency of excitation for a typical dielectrics	139
5.22	Comparison of metallization pressure according to the current EOS and the Herzfeld model with the experimental value	142
5.23	The equations of state of the isoelectronic compounds Xe, CsI, and BaTe	145
5.24	The differences between the normalized equations of state of Xe, CsI, and BaTe	148
5.25	The relative magnitude of total pressure over the Coulomb pressure for CsI under different volume compressions	149
5.26	The relation between the general orthorhombic unit cell and the cubic B2 unit cell	153
5.27	Energy contours for CsI under different compressions	157
5.28	The path of the structural phase transition path of CsI under high pressure	159

5.29	The calculated interplanar lattice spacings as a function of volume fraction for CsI under high pressure	160
5.30	A first order phase transition usually involve a discontinuous change in volume	163
5.31	The square root of the energy differences between the two new structures and the original B2 structure as a function of volume fraction .	164
A.1	Schematic drawing for solving the least square fitting of a non-linear model	169

List of Tables

4.1	Optical parameters for the focusing system	64
5.1	Bulk moduli (in GPa) for alkali halides	84
5.2	A comparison of the observed diffraction peak intensities with calculated values	93
5.3	Pressure-volume data for the ultra high pressure PTCSI run	95
5.4	The relationship among the diffraction peaks from the B2, the orthorhombic, and the hcp structures	101
5.5	A comparison of calculated interplanar spacings with observed values	102
5.6	Pressure-volume data for the CI run	104
5.7	Pressure-volume data for the ADXD run with Ne as the pressure medium	107
5.8	The zero pressure isothermal bulk moduli and its pressure derivatives of CsI derived from previous static studies and present results	117
5.9	The result of non-linear weighted least square fitting of two sets of experimental data to three different EOS formulas	122
5.10	Indices of refraction for alkali halides	143
5.11	Fractional volume at which insulator-metal transition is expected for the alkali halides	143

5.12	The approximate pressures (in GPa) corresponding to the volume fraction in the previous table	143
5.13	The parameters used to calculate the equations of state of Xe, CsI, and BaTe	144
5.14	Different crystal structures that can be described within our orthorhombic unit cell	152
A.1	The pressure volume data used in the fitting procedures	171
A.2	Fitted parameters for different error estimation methods	171

Acknowledgements

I would like to thank my research adviser Professor Sumner Davis for his constant support, understanding and encouragements. It was his moral support that made my graduate life bearable.

I am deeply indebted to Dr. Dave H. K. Mao of Geophysical Laboratory, Carnegie Institution of Washington for teaching me the science and techniques in high pressure physics and giving me opportunities to perform various high pressure experiments. Dave is also a great friend, a wonderful mentor.

I would like to thank Dr. James H. Underwood, my research supervisor, who led me into the world of x-ray optics and showed me that there are still new interesting sciences in this old field, who also gave me enough freedom to pursue my own research interest and endured with me through the difficult path leading to this thesis. I would also like to thank Dr. A. C. Thompson who first introduced me to the wonderful world of synchrotron radiation experiments.

Professors Peter Y. Yu and R. H. Bragg kindly served on my dissertation committee. I got to know Professor Yu as soon as I came to Berkeley, his encouragements over the years have been very important to me. Professor Marvin L. Cohen has always been willing to help, especially when it is most needed. I express my sincere thanks to all of them.

There are many people both at Lawrence Berkeley Laboratory and Geophysical Laboratory of Carnegie Institution of Washington who helped with the projects greatly. I would like to thank Dr. David Attwood for his consistent interest and

support over the years, Drs. Jeff Kortright, Eric Gullikson for their help and for many interesting discussions on a number of topics, and Dr. Rupert C. Perera for being a friend. The long nights of experiments at the synchrotrons was made less tedious and tiring and more enjoyable with the presence of Bob Giaouque and Karan Chapman. I would also like to thank Karen Chapman for reading part of my thesis and making useful comments. Phil Batson and Rene Deleno of LBL provided excellent mechanical support for this project. I am thankful for their quick response when certain parts are needed urgently. Of course, all the members at the Center for X-ray Optics have also been very helpful at times, many thanks to all of them. At Geophysical Laboratory, I would like to thank Drs. R. J. Hemley, L. W. Finger, and C. T. Prewitt for many interesting discussions. Drs. A. P. Jephcoat and C. S. Zha helped me to get started with the high pressure experiments. I would like also to acknowledge Drs. Y. W. Fei, J. Z. Hu, J. F. Shu, and J. V. Badding for helping me during the ADXD experiment.

Many fellow graduate students at Berkeley supported me through their friendship. It is impractical to compile a complete list here because there have been so many of them. My thanks goes to them as well.

The research for this dissertation was supported by the Director, Office of Energy Research, Office of Basic Energy Sciences, Materials Sciences Division, of the U.S. Department of Energy under Contract No. DE-AC03-76-SF00098 and by the U.S. Department of Defence, Air Force Office of Scientific Research through University Research Initiative Contract F49620-87-K-0001.

Finally, a special thanks to my wife, Shirley. My appreciation goes beyond language.

Chapter 1

Introduction

The study of properties of materials under static high pressure has undergone an explosive revolution in the past decade. This came about largely because the developments in the diamond anvil cell technique have enabled pressures exceeding 5 Mbar to be achieved statically. Many properties of materials are expected to show striking changes under these high pressures. Common among the experiments under ultra high pressure is that only a minute sample size can be used. Therefore to study these changes and new properties, various new techniques are needed. Some of them are simple adaptations of common experimental techniques to a smaller probe size, while new developments are needed for others.

Crystal structure is one of the fundamental properties of a material and its change under external conditions reflects directly the change in the interaction among the atoms. Often the change of other properties is related to a crystal structure change and vice versa. For example, the structure of crystalline Si changes from the diamond structure under ambient conditions to the β -Sn structure upon metalization under pressure. The crystal structure of materials under pressure also serves as an important check for and sometimes input to theoretical calculations.

We have examined the crystal structural changes of a prototypical ionic solid CsI under high pressure. CsI is the most compressible of the simple alkali-halide ionic compounds. Its behavior under high pressure is representative of the behavior

of other compounds under higher pressures. Extensive research on CsI under high pressure has been done during the last decade because of this. Metallization has been observed to occur at a pressure just above 100 GPa based on optical absorption and reflectivity measurements. However, crystal structural studies have been performed only in a somewhat restricted pressure range and seem to have a systematic deviation from the results of shock wave and theoretical studies. With the recent capability of generating very high pressures reliably, a detailed study of the crystal structure is therefore in order.

The study of materials under very high pressure requires the use of very small samples. To perform x-ray diffraction experiments on these samples requires the use of very intense x-ray beam with a very small beam size. This has only become possible largely because of the availability of synchrotron radiation sources. The unique properties of the synchrotron radiation also calls for special instrumentation to be developed. Although the recent use of the energy dispersive x-ray diffraction (EDXD) method has been highly successful, its shortcomings are also evident. Two major drawbacks are to be overcome in order to extend x-ray studies to even higher pressures than what is currently available and to higher resolution than what is afforded by the EDXD method, so materials with more complex structures and onset of phase transitions can be studied. It is clear that in order to maintain the level of x-ray flux when one pursues a smaller beam size, a focusing system rather than the presently used pinhole system is necessary. Also, higher resolution in the diffraction pattern can be achieved by using the angular dispersive x-ray diffraction (ADX) method. We have undertaken a study to extend the currently available techniques along these lines. A focusing system consisting of two multilayer coated spherical mirrors was used as a first step towards the above goal.

This dissertation is organized in the following manner. Chapter 2 deals with the techniques used to achieve high pressure, and procedures for pressure calibration. Chapter 3 presents the concepts of and comparisons among several x-ray experi-

mental techniques. Chapter 4 describes the development of a focusing system for x-rays and its application to high pressure studies. Finally, Chapter 5 presents a systematic study of the crystal structure of CsI under high pressure using both the EDXD technique and the ADXD technique with a focusing system.

Chapter 2

Diamond Anvil Cell Technique in High Pressure Structural Studies

This chapter gives a brief account of the diamond anvil cell method used in the work of this thesis. Since a nice detailed description of the operation of the diamond anvil cell has been given by Jephcoat *et al.*[43], this chapter only covers the more essential procedures. The first section below is general and describes the setup procedure necessary for any high pressure experiment using diamond anvil cells. The x-ray procedure will be described in a separate chapter. The second section deals with the pressure calibration method for high pressure experiments.

2.1 Generation of high pressures using diamond anvil cells

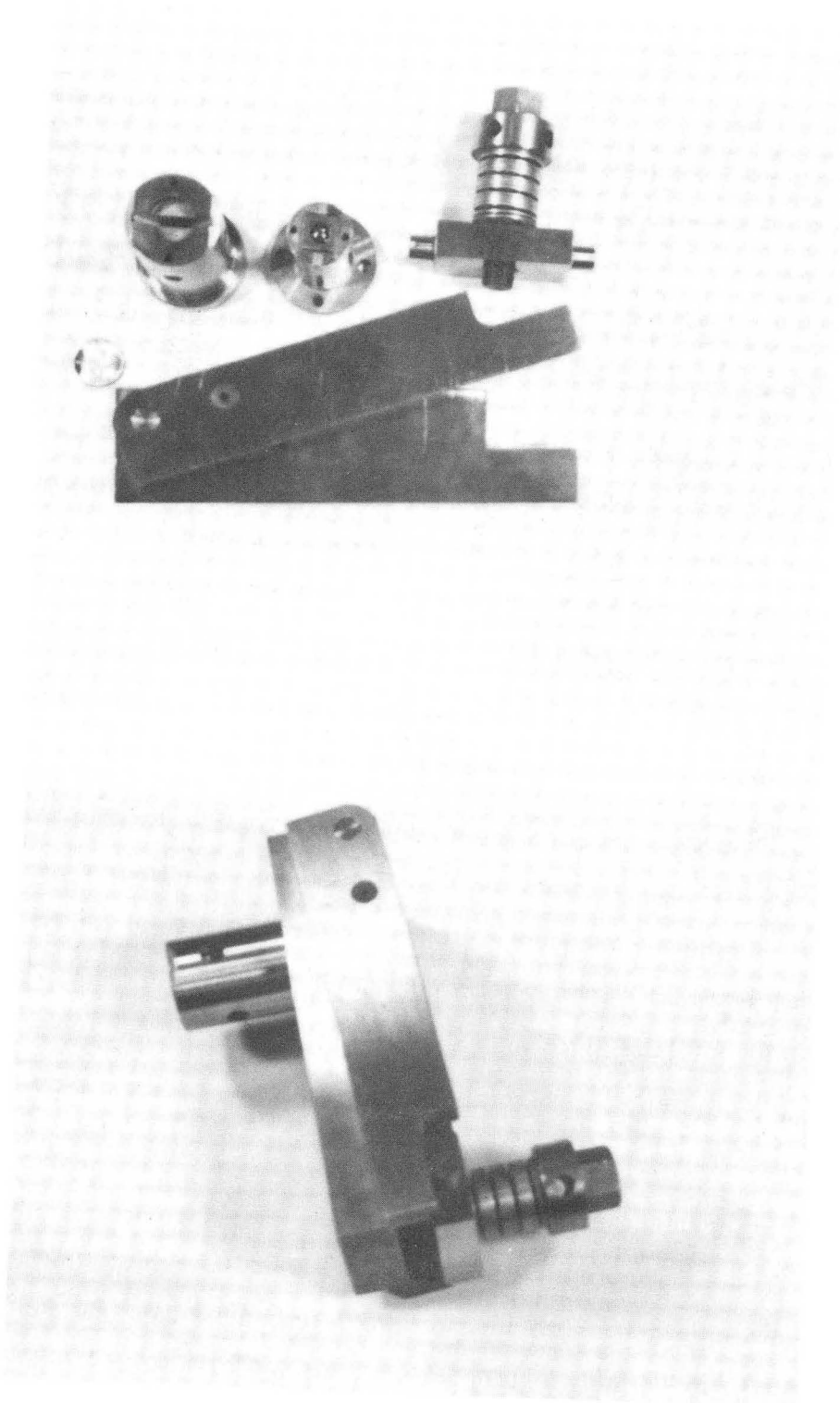
The pressure generated at a surface is directly proportional to the applied load and inversely proportional to the load bearing area. Therefore a tapered device can act as a pressure amplifier with the amplification given by the ratio of the area of the two end surfaces. The generation of high pressures ($> 10 \text{ GPa} = 10^{10} \text{ Pascal}$) for moderate loads (10^4 Newton) on mm sized surfaces requires a end surface with a size of a few hundred microns or less. The great pressure variation in the material calls for use of high yield strength material. Single crystal diamond is the best

candidate[2]. Diamond has the highest known yield strength of all materials and because of that there has been no quantitative information concerning its value. It is also the hardest material known, so it has found wide applications in generation of very high pressures. But it is also one of the most brittle materials[4], and is likely to fail by cleavage or by fracture. This makes diamond anvil cell experiments extremely delicate.

The designs of the diamond anvil cell used in this thesis work originated from an earlier design at the National Institute of Science and Technology (formerly, National Bureau of Standard) [5] with various modifications added[6, 7]. Improvements included an increased travel length of the piston within the cylinder to better maintain the alignment of the two diamond anvils. Loads are generated and maintained by compression of Belleville spring washers(0.975" outside diameter) through a 5:1 lever arm so a smoother pressure variation is possible.

The mechanical specifications for the diamond anvil cells used in the experiments described here can be found in Mao and Bell[6]. Alternative designs and variations and its applications in high pressure research in general can be found in Jayaraman[8]. Figure 2.1 shows a picture of one of the diamond cells. The piston cylinder assembly is disassembled to enable a better view of all the components. A more detailed description of each component and their assembling is described in the following paragraphs.

For each experimental run, one has to decide the pressure range to cover, because it is essential to use an appropriate diamond anvil pair to avoid premature failure of the diamonds. In general, a smaller working face (culets) can generate a higher pressure limit. For moderately high pressure experiments ($P < 100$ GPa), a normal cut anvil with culet size larger than $100 \mu\text{m}$ can be used. For higher pressures a smaller culet size is necessary and it is also necessary to make them beveled in order to have adequate support and reduce the pressure gradient on the diamond surface. Figure 2.2 shows schematics of the two kinds of anvils. In the case of beveled anvils,



XBB 905-3700

Figure 2.1

Figure 2.1: A picture of a typical diamond anvil cell used in high pressure studies. In the picture on top, the diamond anvil cell is disassembled to show its components. They are, in clockwise order, (a) the cylinder which holds one of the diamond anvils which is on the inside of the cylinder. The visible slot is for optical scattering and x-ray diffraction studies; (b) the piston, on its top, the other diamond anvil along with its seat, the rocker; (c) the Belleville spring washer assembly which is used to apply forces; and (d) The lever arm which holds everything together. On the bottom picture, the assembled diamond anvil cell is shown.

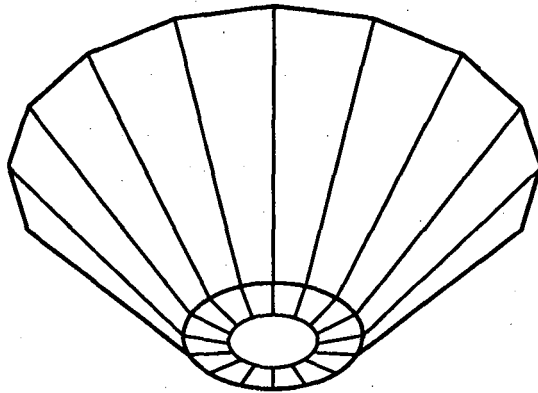
the central flat is usually less than 50 μm .

There are other considerations one has to take into account when one is doing spectroscopy work. Because diamond (natural or synthetic) usually comes with various levels of impurities therefore it's optical properties vary greatly. They are classified into two types(I and II). A type I diamond's absorption edge is near 300 nm and shows a complex system of absorption bands in the infrared. A type II diamond's absorption edge is located at about 230 nm and the absorption in the infrared is absent. They can be further divided into more detailed categories according to their impurity contents[2]. For x-ray work, the only possible needs for using visible light are viewing of the sample and pressure calibration using ruby fluorescence. For pressure calibration using the ruby fluorescence method that will be described later, the optical properties of the various types of diamonds do not affect the results very much and therefore all of them can be used. Since type I are usually less expensive most of the diamond anvils used in the experiments described here are of type I.

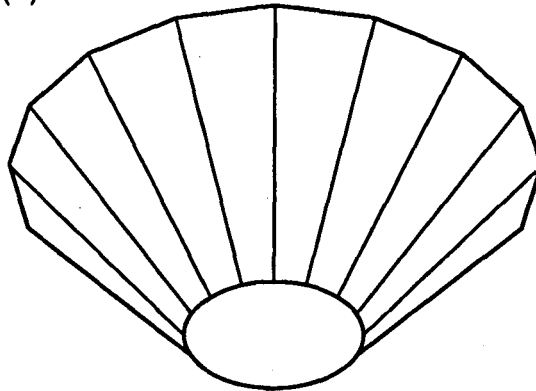
A visual check is made for flaws such as surface scratches due to polishing, inclusions, and regions of high birefringence indicative of internal stresses that produce anisotropy in the cubic structure, and could lead to earlier failure. The table face should be parallel to the culet to a high degree. The dimensions of the diamonds are then measured under a microscope. These include the culet diameter, table size, waist diameter, culet to table thickness, and bevel angle and central flat diameter in the case of beveled diamond anvils. A pair with closely matched flat size can then be used in the experiment. The thickness of the anvil on the cylinder side is an important parameter because it is used in the process of determining the lattice parameters.

The selected diamonds are then ready to be mounted onto tungsten carbide half cylinder seats or rockers. Both the diamonds and the rockers are cleaned ultrasonically after removal of any roughness and surface contamination with fine-grained corundum paper before they are mounted together. The rocker serves two purposes:

(a)



(b)



XBL 908-5917
lg/m

Figure 2.2: Schematic drawing of the diamond anvils. (A) shows a regular diamond anvil for moderate pressure studies; (B) shows a beveled diamond anvil used in ultra high pressure studies.

(1) it is a transition zone for the pressure distribution between the diamond anvils and stainless steel cylinder and piston parts; and (2) an alignment tool since it can be translated and rotated (hence the name rocker) with respect to the cylinder and piston. The rockers have tapered holes or slots in them to enable optical access along the loading axis. For X-ray work, a piston rocker was used with a 0.015" diameter hole tapered to 0.06" on the convex side, and a cylinder rocker with a tapered slot 0.015" by 0.14" at the mounting surface and wider on the convex side to enable a larger accessible angle for x-ray diffraction use. The typical opening angle of these cells is $2\theta < 40$ degrees. To reduce the effect of stress concentration between the contacts of the anvils and the rockers, a 25 μm thick zirconium foil with slightly larger size than the diamond table size is placed in between. The foil shims have holes punched in them to match the opening of the rocker. Each diamond and the corresponding rocker is then clamped together by the use of a miniature glass anvil that has been polished to provide optical access to the rocker surface. It is important to remove any small pieces of zirconium foil in the beam path in x-ray diffraction work (especially when the angular dispersive method is used) to prevent any complications due to the diffraction lines from them. Fine adjustments of the position of the diamonds are made under a binocular microscope until the diamonds are perfectly flat on the rocker and symmetric with respect to the hole or slot on the rocker. The diamonds are bonded to the rockers with an epoxy resin (Emersin and Cuming Stycat 2850 Black) which has good thermal properties and high hardness.

After the resin has set in about 10 hours, the rockers are removed from the miniature anvil holders and mounted in the piston or cylinder. The rockers are seated on a curved surface which matches the rocker outline to a high degree and are held in place with two set screws located on the axis of the rocker. The piston and cylinder are mated together with the axis of the rocker perpendicular to each other. This way, the relative translation between the two diamonds in both direction and the rotation around two orthogonal axis is possible to facilitate the alignment procedure. The purpose of alignment is to ensure that the center of both diamond

anvils are matched and the two flat surfaces parallel to each other. The relative position of the two diamonds is first adjusted by viewing from aside through the holes on the cylinder. At the same time, if the diamonds are too far away from parallel to each other, the two rockers are rotated as well to improve the parallelism. Once this is done, one can usually look along the loading axis and see the interference fringes between the surfaces of the two diamonds. Also, a better view of how the position of the two diamonds match each other is possible. Caution must be exercised during this process to avoid contact between the two diamonds because they can easily fracture when they hit each other. Even if no visible sign is produced, there are still possibilities that a microscopic fracture is caused and that will lead to premature failure of the anvils under pressure. The positions and orientations of both diamonds are further adjusted until less than half a fringe across the diamond surface remains. This gives a good indication that the two surfaces are parallel to each other to a high degree. Finally, it is also necessary to test that the alignment is maintained under pressure, which involves indenting a gasket to a trial pressure and repeating the above steps again if necessary.

After the diamond anvils are well aligned, we need to prepare gaskets for the experiments. The function of gasket is several fold: (1) it helps to reduce the pressure gradients in the sample area as well as around the diamond surface; (2) it provides additional support in addition to the sample itself, thus enabling experiments on fragile materials with low strength; (3) it also serves as a container when gas is loaded into the sample chamber either for quasi-hydrostatic experiments or experiments on those gases itself. Thus the general requirements for the gasket is that it should have high strength especially tensile strength, and suitable hardness, and be ductile. In the case of using it to contain gases, it also needs to be gas tight. In all the experiments described in this thesis, the gaskets used were fully hardened T301 stainless-steel of 250 μm initial thickness. To provide additional support under high pressure, all of them are indented to moderately high pressure (30 GPa or so) before a hole is driven. The exact pressure of indentation depends on the highest pressure

one expects to work with. The drilling is done by using a micro-drill system (Mini-Tool, National Jet Co. drills). Different hole sizes as small as 25 μm can be drilled. Again, the size of the hole depends on the size of the culet and the maximum pressure intended. In the case where a pressure medium is to be used, one need to pay extra attention to the size of the hole so a seal is possible upon loading. Of course, the hole has to be well centered with respect to the gasket depression, which is the same as the center of the diamond flat. Usually, a few gaskets need to be prepared before one gets a satisfactory one. The orientation of the gasket with respect to the piston is marked before the hole is driven so when the gasket is remounted onto the piston, the indented facets match exactly with the piston diamond. This way, it will ensure that there is no large free space between the gasket and diamonds so the sample loading is made easier. More importantly, it will reduce the possibilities of misalignment of the sample chamber with respect to the diamond anvil center.

For normal experiments without a pressure medium, the gasket hole is filled completely with the sample, which is usually in the powder form. If a pressure medium is to be used, it is necessary to make the powdered sample into a disk that is smaller than the anticipated chamber diameter under compression and thinner than the gasket thickness. It is extremely important that this is observed because if the sample is compressed directly either by direct contact of both anvils or gaskets, a very anisotropic stress condition appears and this destroys the whole purpose of using a pressure medium.

A good pressure medium should have very low strength and does not interfere with either the sample or the signals important to the experiment. A mixture of methanol - ethanol (in the ratio of 1:3 or 1:4) can be used for pressures which do not exceed 10 GPa. But above 10 GPa, it freezes into a solid and is not a very good pressure medium. Of course, all materials will become a solid under sufficiently high pressure therefore eventually lose its abilities as a pressure medium. Rare gases seem to be the last ones to become a solid, and they are suitable candidates. He

is probably the material with the highest transition pressure at which it transforms into its solid phase. Even so, solid phase of He has been observed at 21 GPa at room temperature[9]. Under these situations, the best pressure medium will be the material with the smallest yield strength. In general, all rare gas fluids or solids serve as very good pressure medium. Neon and argon are most widely used and is known to maintain quasihydrostatic conditions up to pressures approaching 100 GPa. Of course, the quality of the quasi-hydrostatic environment is relative. Depending on the sample, the same anisotropy can have very different effects. In our experiments on CsI described in Chapter 5, this point is made more obvious by the low strength of CsI itself.

Early work on using gases as pressure media is limited because it has to be loaded under cryogenic conditions. Recent developments of high pressure gas apparatus for loading gases at pressure around 0.2 GPa into the diamond anvil cell have led to much progress in experiments on these gases and those that utilize them as pressure media. The apparatus used in the experiments here was based on a design originally described by Mills *et al.*[10]

In the loading apparatus, the piston and cylinder assembly are enclosed in a closely matched aluminum mount which is tightly fitted into the pressure vessel. A gear mechanism is used for remote control of the tightening of the piston cylinder assembly and sealing the high pressure gas in the gasket.

In order to maintain the pressure in the sample chamber upon removing of the piston cylinder assembly, a subsidiary pair of drive screws is threaded into the cylinder through the piston base plate, the load is applied with 0.35" diameter Belleville washers. The amount of rotation that is necessary to seal the gas in the sample chamber is calibrated by using a separately prepared but identical gasket, filled with water and ruby chips and noting the point where the pressure starts to increase when the load is increased by rotating the loading screw.

A two stroke, air driven, diaphragm type compressor (Superpressure Inc., model

45-14021-1) was used to raise the pressure in the vessel up to 0.2 GPa. During a loading, the apparatus is flushed by pumping to a pressure of 100 atmospheres with the appropriate gas several times before the filling so any residual air or unwanted gas is flushed from the pressure vessel. The pressure is monitored closely and leaks checked at intermediate pressures. Upon the sealing of the piston cylinder assembly, the pressure in the vessel is released and piston and cylinder assembly removed and inspected. It is not unusual to find out that the sample is lost during the pumping process or the gas is lost in the sample chamber due to insufficient tightening. Under these circumstances, it is often necessary to start over from the preindentation of a new gasket. If the loading of the gas medium is successful, there should be no noticeable pressure variation when the pressure is below 10 GPa.

2.2 Pressure measurement

In principle, pressure can be calculated by measuring the load. However, because of its variation across the sample area and friction between the mechanical parts, this method usually does not give very accurate measurements of the sample pressure, so a secondary pressure calibration is necessary. By far the most widely used technique to measure the pressure in an high pressure experiment is by using ruby fluorescence technique. This method, based on the shift of the R_1 (6942.4 Å) and R_2 (6928.0 Å) lines in the fluorescence spectrum as a function of pressure. Early development of this method is described by several authors [11, 12]. In this case, the relation between the shift and pressure is determined by using the fixed point method, in which a pressure of phase transition is measured by utilizing other methods. More recently, Mao *et al.*[12, 13, 15] have determined the relation between the pressure and R_1 shift over a large pressure range by using the shock wave determined equation of state for metals which do not have phase transitions in the covered high pressure region (Cu, Ag, Pd, Mo). In this case, the pressure under each specific loading is calculated by using the measured volume data by *in situ* x-ray diffraction under

both non-hydrostatic (no pressure medium) and quasi-hydrostatic (rare gas solid pressure medium) loading conditions. The relation thus obtained can be described by the following two empirical formulas:

$$P = 3.808\left\{1 + \left(\frac{\Delta\lambda}{\lambda_0}\right)^5 - 1\right\} \quad (2.1)$$

and

$$P = 2.484\left\{1 + \left(\frac{\Delta\lambda}{\lambda_0}\right)^{7.665} - 1\right\} \quad (2.2)$$

for non-hydro static [15] and quasi-hydrostatic [13] compression respectively, where λ_0 is the R_1 line wavelength at ambient pressure and $\Delta\lambda$ is the wavelength shift under a given pressure.

For non-hydrostatic compression, ruby powder is scattered on the sample surface. Each chip is small enough so they do not bridge the anvils. Finely ground ruby ($\text{Al}_2\text{O}_3:\text{Cr}$) can be suspended in a liquid and the evaporation of the liquid will leave the particles separate into different layers, and thereby different grain sizes can be selected. The quantity of the ruby powder should be sufficient so the pressure measurement can be made in a reasonable time interval. The fluorescence intensity decreases sharply as a function of pressure and this effects should be taken into account. But too much ruby will produce unwanted effect like the interference of the diffraction lines from the ruby powder in an x-ray experiment. It is also important that the ruby pieces are on the surface of the sample because optical access is necessary to record the fluorescence. For quasi-hydrostatic compression where the sample is loaded with a pressure medium, the ruby powder can be pressed into the sample disk while preparing the sample.

In the laboratory, pressures were measured using the system described by Mao *et al.*[16]. In this system, a He-Cd (Liconix, 4416Å, 40mW) laser is used to excite the fluorescence, the fluorescence from the ruby powder in the diamond cell is collected and sent through a dichroic mirror before it reaches the spectrometer (Jarrell-Ash 0.5 m Ebert scanning). While on a synchrotron, the fluorescence can be excited by the x-rays. In this case, one particular advantage is that one can measure the

pressure at the same point because no physical movement of the cell with respect to the beam is necessary. When the experiment is done in the laboratory, the pressure measurement can be done at many points, and a distribution can be obtained. A suitable average of the distribution is taken to be the average pressure. The pressure is measured before and after the x-ray exposure is taken that usually takes several days on a laboratory x-ray source, a small variation can be observed between the measurements. The spectrometer is calibrated every time a new pressure is measured by measuring the ruby R_1 line under ambient pressure. In the synchrotron experiments, the time elapse between runs is so short, a recalibration of the spectrometer is unnecessary. However, it is noted that one typically needs to wait for a few minutes before the pressure measurement is taken after an increment in pressure in order to have the pressure settled. After the intensity as a function of wavelength is obtained, the position of the highest intensity of the R_1 line is measured, and the pressure determined.

Since the ruby fluorescence is extremely weak at high pressures, it is sometimes more convenient to use the internal standard method in x-ray diffraction experiments. A well behaved material (chemically inert, high diffraction power, simple structure with no phase transitions) with a known equation of state is ground into powder and mixed with sample before loading. X-ray diffraction patterns of both the sample and the standard material are taken at the same time. The unit cell volume of the standard can be used to calculate the pressure. Platinum and gold have been used often in very high pressure experiments. Their equations of state are derived from shock wave experiments and theoretical calculations.

All x-ray experiments described in this thesis were performed on synchrotron radiation beamlines, so most of the pressure measurements were based on this internal standard method. Ruby fluorescence method is only used during the preparation of the experiments and occasionally during the experiments. The internal standard used here is platinum, its room temperature isotherm is taken from the recent com-

bined shock wave and theoretical study[17]. The relation between pressure and unit cell volume can be described by the following formula:

$$P = 798.31(\text{GPa}) \frac{(1 - X)}{X^2} e^{7.2119(1-X)}$$

where $X = (V/V_0)^{1/3}$ and V_0 is the zero pressure unit cell volume.

Chapter 3

X-ray Diffraction Methods in High Pressure Studies

Most of the results contained in this thesis were obtained using various x-ray diffraction techniques. Although x-ray diffraction processes are well understood, it is still useful to include a brief discussion here for the following reasons: 1) the energy dispersive method used here is seldom described in textbooks; 2) in experiments on materials under high pressure using diamond anvil cell techniques, one may have a very strong background due to inelastic scattering from diamond, which is absent under most other circumstances and therefore is not discussed in detail elsewhere; 3) we want to present a comparison between the various methods and sources.

3.1 Scattering by a single electron

From the classical electrodynamics point of view, when a plane wave of monochromatic electromagnetic radiation is incident on a particle with mass m and charge e , the particle is driven by the electromagnetic interaction and oscillates back and forth, emitting electromagnetic radiation just like an oscillating electric dipole. The radiation has the same frequency as the incident radiation but in a wide range of directions. The amount of radiation that it emits in unit solid angle in a particular direction can be calculated. It is proportional to the incident intensity. The ratio of

the two is termed differential scattering cross section. For an unpolarized incident radiation, this is given by J. J. Thomson as [Equation (14.103) of [18]]

$$\frac{d\sigma}{d\Omega} = \frac{1}{2} \left(\frac{e^2}{mc^2} \right)^2 (1 + \cos^2 \theta) = \frac{r_e^2}{2} (1 + \cos^2 \theta) \quad (3.1)$$

where, $r_e = e^2/mc^2$ is the classical radius of electron and θ is the angle between the incident and scattered radiation. The derivation of this formula does not require any specifics of electrons so it is also valid for scattering by protons. It is immediately evident that the cross section for protons is much smaller than that of electrons because of the mass difference between the two particles. This also illustrates that the interaction between x-rays and matter is mostly determined by the interaction between x-rays and electrons at x-ray energies for which the *Thomson formula* (3.1) is valid.

The classical treatment neglects the effects of recoil of the electron as a result of transfer of the photon momentum. For low energy photons, this is a rather good approximation. It is certainly not exactly the case for x-rays with energies greater than a few keV which most diffraction experiments use. In the case where the momentum transfer cannot be neglected, the incident photon also suffers an energy loss. By using both the momentum and energy conservation, it is straightforward to show that the scattered photon has a wave length λ' given by the *Compton formula* [Equation (1-25) of [19]],

$$\lambda' = \lambda + \frac{h}{mc} (1 - \cos \theta) \quad (3.2)$$

where θ is the angle between the incident and scattered radiation. The derivation of cross section for this process is much involved and the final result is given by *Klein-Nishina formula* as [Equation (5) of Hubbell *et al.*[20]]

$$\frac{d\sigma_{KN}}{d\Omega} = \frac{r_e^2}{2} [1 + k(1 - \cos \theta)]^{-2} \left[1 + \cos^2 \theta + \frac{k^2(1 - \cos \theta)^2}{1 + k(1 - \cos \theta)} \right] \quad (3.3)$$

where k is the photon energy in units of the electron rest mass energy (*i. e.*, $m_e c^2$).

From Equation (3.2), since the shift in wavelength is independent of the photon energy, the shift in energy is therefore proportional to the square of the photon

energy and is small for low energy photons thereby validates the classical elastic scattering argument. It is also important to note that for very low energies ($k \rightarrow 0$), we recover the *Thomson formula* from Equation (3.3). Therefore, strictly speaking, there is no purely elastic scattering when electromagnetic radiation is scattered by a free charged particle, it is only in the limiting sense that we speak of elastic scattering for a free electron.

3.2 Scattering by an atom: coherent and incoherent scattering

Conceptually, the scattering of x-rays by an atom is different from that by an electron in that we can have a well defined boundary between coherent and incoherent scattering. The process of coherent scattering can be defined as the process in which the incident photon leaves the atom in the atomic ground state. This is possible because an atom has a much larger mass and therefore the energy transfer associated with momentum transfer is negligibly small. Incoherent scattering, on the other hand, changes the atomic state. Compton scattering where part of the photon momentum is transferred to one electron similar to the free electron case turns out to be the most important of all incoherent scattering processes in the x-ray energy range that we are interested in.

A rigorous calculation for the coherent scattering cross section for an atom should therefore include all contributions from the process

$$\gamma + \Phi_0 \longrightarrow \gamma' + \Phi_0$$

where, γ and γ' denote the incident and scattered photons, and Φ_0 represents the atomic ground state. The first order contribution to this process involves an intermediate state where the incident photon is absorbed by the atom and then reemitted at the same frequency. In fact, calculation of this effect probably represents the best theoretical calculation for the coherent scattering cross section for an atom[21].

In almost all textbooks on x-ray diffraction, the treatment of scattering by an atom is based on a less rigorous approximation. With the understanding above, we take a look at the *form factor approximation* to the scattering of x-rays from an atom. This approximation stems from a combination of classical and quantum mechanical concepts. As we have discussed in last section, a free electron can scatter a relatively low energy photons elastically with its cross section given by Equation (3.1). From quantum mechanics, we know that the electrons in atoms can not be described as point charges but rather as continuous distributions around the nucleus. To correct for that, the form factor approximation assumes that an electron at position \vec{r} with density $\rho(\vec{r})$ has a scattering amplitude proportional to (3.1) and $\rho(\vec{r})$ with an appropriate phase factor. The total amplitude is obtained by summing the amplitudes due to charge distributions at all points.

$$\frac{d\sigma}{d\Omega} = \frac{r_e^2}{2}(1 + \cos^2 \theta)|f(\vec{q})|^2 \quad (3.4)$$

where

$$f(\vec{q}) = \sum_{n=1}^Z \langle \Phi_0 | \exp(i\vec{q} \cdot \vec{r}_n) | \Phi_0 \rangle$$

and Φ_0 is the ground state wave function of the atom, \vec{q} is the momentum transfer vector and \vec{r}_n is the position of the n th electron with respect to the position of the nucleus.

This atomic form factor also can be expressed as the integral,

$$f(\vec{q}) = \int \rho(\vec{r}) \exp(i\vec{q} \cdot \vec{r}) d^3\vec{r}.$$

For a spherically symmetric atom the angular integration can be performed, resulting in

$$f(q) = 4\pi \int_0^\infty \rho(r) \frac{\sin(qr)}{qr} r^2 dr.$$

The necessary condition for the above derivation to be valid is that the energy of the incident photon is high enough so the bound electrons scatter like free electrons and at the same time not so high that there is significant Compton scattering.

Despite these severe limitations, it is experimentally found that (3.4) gives a very good description in normal x-ray diffraction studies. From the above derivation it is also clear that in the form factor approximation the scattering cross section is independent of the energy of the incident photons, which intuitively is not true. In fact, when the energy of the incident x-rays is close to the binding energies of electrons, the deviation is rather large. Traditionally, “anomalous scattering factors” are introduced in such cases, so that the simple form of the coherent scattering cross sections in the form factor approximation, given by (3.4), can be retained by replacing factor $f(\vec{q})$ by a scattering factor given by

$$F(\vec{q}) = f(\vec{q}) + \Delta f' + i\Delta f''.$$

The above derivation for the coherent scattering cross section, can also be applied to individual electrons and the coherent scattering factor obtained for specific electrons,

$$f_n(\vec{q}) = \langle \Phi_0 | \exp(i\vec{q} \cdot \vec{r}_n) | \Phi_0 \rangle$$

clearly, $|f_n(\vec{q})| \leq 1$, *i. e.* there is a reduction in the cross section relative to a fixed point charge case. Historically, the difference has been attributed to the *incoherent scattering*. So the incoherent scattering cross section for a single moving electron is given by

$$s_n(\vec{q}) = 1 - |f_n(\vec{q})|^2$$

For atoms that contain more than one electron, the total incoherent scattering cross section is simply a summation of the cross sections (rather than amplitudes) for each individual electron:

$$s(\vec{q}) = \sum_{n=1}^Z s_n(\vec{q}).$$

Appropriately, the unit of this cross section should be that given by the *Klein-Nishina formula* (3.3), although for the energy range ($\hbar\omega < 50$ keV), where diffraction studies are normally performed, the difference between this and the *Thomson formula* is less than 10% in the angular range one normally uses to obtain diffraction data.

3.3 Scattering by crystals

X-ray scattering by crystals can be derived similarly as in the case for single atoms. Since the arrangement of atoms in a crystal is periodic with a basic unit described as the unit cell, the diffraction from these periodical structures is similar to the theory of optical diffraction. The detailed derivation can be found in many textbooks, and will not be repeated. A summary of the important results are presented here.

3.3.1 The Bragg law of diffraction

By requiring that diffracted x-rays from different atomic planes of a crystal have a phase difference suitable for constructive interference, we immediately obtain

$$2d \sin \theta = n\lambda \quad (3.5)$$

This equation enables us to calculate the angles where diffracted beams may be found when a monochromatic x-rays with wavelength λ is used for diffraction or alternatively the wavelengths (energies) when polychromatic radiation is used and the diffraction pattern is recorded at a fixed angle. Here d is the distance between the atomic planes. There are many sets of planes with various d spacings that are capable of diffraction in crystals. But for single crystals, each set of planes has a well defined orientation and diffraction only occurs when the normal to the set of planes is in the scattering plane and bisects the angle between the incident and diffracted beam. Therefore, one typically needs to search extensively in three dimensions for the diffracted beams. A more conventional method is used when one wants to investigate relatively simple crystal structures. One considers a collection of very small crystals with random orientations with respect to each other. In this case, the diffracted beams form cones and the diffraction peaks are reduced to have a one dimensional feature only. Since all the experimental data presented here is obtained this way, we will restrict our discussions to such methods.

By differentiating the Bragg law, we obtain

$$\frac{\Delta d}{d} = \frac{\Delta \lambda}{\lambda} + \frac{\cos \theta}{\sin \theta} \Delta \theta \quad (3.6)$$

it is clear that the resolution in the lattice spacing d 's measurement is determined by the energy resolution and the angular resolution. There are two modes of diffraction commonly used based on this formula. One is called the Angular Dispersive X-ray Diffraction (ADX) in which one employs x-rays with a single energy(wavelength), and record the diffraction pattern in the angular(reciprocal) space. This corresponds to the case that the first term is much less than the second term in Equation (3.6). The second method is called the Energy Dispersive X-ray Diffraction (EDXD) or Wavelength Dispersive X-ray Diffraction. In this case, the detector is set at a fixed angle, and the diffraction pattern is recorded using an energy dispersive detector. Normally, the resolution is mostly determined by the first term in equation (3.6).

3.3.2 Integrated intensities

In both cases, the diffracted intensity in a Debye ring (which is the intersection area between a diffraction cone and a cylindrical surface as a piece of film used in the experiment) for a given set of planes can be easily derived. It is the same as the total intensity in the diffraction cone. Following the approach of Warren[22], neglecting absorption and extinction, it can be written as

$$I = I_0(\lambda) \Delta \lambda \frac{1}{8} r_e^2 \frac{\lambda^3 V}{v^2} |F|^2 m \frac{1 + \cos^2 2\theta}{\sin \theta} e^{-2M} \quad (3.7)$$

here I is the integrated intensity over the entire Debye ring (photons/sec), $I_0(\lambda) \Delta \lambda$ is the x-ray flux per unit area of the incident beam (photons/sec/area), $|F|$ is the structural factor corresponding to a unit cell defined similarly to the case of a single atom, v is the volume of the unit cell of the crystal, m is the multiplicity factor which is defined to be the number of directions in which the lattice spacings are the same, e^{-2M} is the Debye-Waller factor which accounts for the loss of intensity due to vibrations of the atoms, and V is the volume of the crystal that is illuminated

by the x-ray beam. Note here the scattering angle is 2θ . This formula was derived for the case of monochromatic radiation, but as pointed out by Buras[23], by substituting $\Delta\lambda = \lambda \cot \theta_0 \Delta\theta_0$, one can obtain the integrated intensity in a complete Debye ring for the EDXD method. If the sample is uniform and has a large cross section perpendicular to the beam, the diffracted intensity is proportional to the total available flux and does not depend on the area of the sample that is illuminated. However, if the sample is small, the intensity is determined by the x-ray flux striking the sample.

To obtain the relevant formulas for samples under high pressure in a diamond anvil cell, one needs to take into account the absorption due to both the sample and the diamond anvils. The absorption due to the anvils can be written simply as $\exp(-\mu_d(d_p + d_c/\cos 2\theta))$, where d_p, d_c are the thickness of the diamond anvil on the piston and cylinder side respectively, and μ_d is the absorption coefficient for diamond, which is a function of x-ray energy. The absorption due to the sample itself can be found by a simple integration[26], it can be written as

$$\frac{e^{-\mu d_s/\cos 2\theta} - e^{-\mu d_s}}{\mu d_s(1 - 1/\cos 2\theta)}$$

where d_s is the sample thickness, μ is the absorption coefficient for the sample.

Another aspect that should be mentioned is that synchrotron radiation is close to 100% polarized with the electric field vector in the orbital plane. This affects the intensity formula by modifying the polarization factor. Instead of being the averaged value of $(1 + \cos^2 2\theta)/2$, it is either 1 or $\cos^2 2\theta$ depending on the direction of the scattered radiation collected. In the ADXD method, we have chosen to record the diffraction pattern in the vertical plane hence the factor should be 1. In the EDXD method, the diffraction is collected in the horizontal plane, so the polarization factor should be $\cos^2 2\theta$. It is a constant as well in a diffraction pattern, since the diffraction pattern is recorded at a fixed angle.

Just to give an idea of the strength of the inelastic scattering, we consider only the contribution from the non-point-distribution nature of the electron charge dis-

tribution (*i.e.* we ignore the contribution from the motion of the atoms or ions as a whole). Since the scattering is inelastic, the intensity due to both the sample and the diamond anvils are simply a summation over all the individual atoms. Hence, the intensity is a smooth function of the scattering angle 2θ and, in the absence of anomalous dispersion, a smooth function of energy. Assume the beam size is S , the scattering intensity with scattering angle between 2θ and $2(\theta + \delta\theta)$ can be written as

$$[S(d_c + d_p)N_d s_d + S d_s N_s s_s] \frac{r_e^2}{2} (1 + \cos^2 2\theta) 2\pi \sin 2\theta \delta(2\theta) \quad (3.8)$$

where N_d , s_d and N_s , s_s are the atomic density and inelastic scattering factor for the diamond and sample respectively.

Of course, the above formula should be corrected by absorption as well. The absorption factor for the part due to the sample is identical to the one pointed out above. For the anvil on the cylinder side, it is

$$\frac{\exp(-\mu_d d_p) \exp(-\mu_d d_s) e^{-\mu_d d_c / \cos 2\theta} - e^{-\mu_d d_c}}{\mu_d d_c (1 - 1/\cos 2\theta)}$$

where the symbols have the same meaning as before. An extra complication arises in the contribution from the anvil on the piston side caused by the existence of a gasket. We will not attempt to derive a formula for it here. In practice, the gasket is rather thick and a strong absorber of x-rays, only the sample itself and the gasket near the sample is very thin. Hence except for x-rays with a very small scattering angle or coming from the part of the diamond that is very close to the sample, the scattered radiation will be mostly absorbed by the gasket and make a negligible contribution to the total intensity of the inelastically scattered radiation.

3.4 A comparison of EDXD and ADXD methods

The two methods used to perform diffraction experiments are closely related in theory as described above. In reality, because quite different instrumentation is needed, they offer different merits depending on the actual requirements of the

experiment. A comparison of the two methods is presented below.

3.4.1 Resolution

In the EDXD method, solid state detectors are used to differentiate the energies of the x-ray photons. They are usually made of high quality semiconductor single crystals, typical Ge or Si. The incoming x-ray photons excite electrons from the valance band to the conduction band. These electrons and the holes they left behind are subsequently collected. Since the excitation energy of a single electron is quite low (on the order of the band gap), many electrons are excited by a single x-ray photon, therefore the current in the single pulse is proportional to the energy of the incoming photon. The resolution of these detectors can be represented by the formula[24],

$$\Delta_D E_{FWHM} = \{(\Delta E_{amp})^2 + [2.355(F\epsilon E)^{1/2}]^2\}^{1/2}$$

where ΔE_{amp} is due to the solid state detector leakage noise and to the preamplifier noise, F is the Fano factor with a typical value of 0.15, and ϵ is the energy required for creating an electron- hole pair. At low energy, the resolution is dominated by the first term. The resolution of a typical solid state detector is 0.15 to 0.2 keV for 6keV x-rays. Although the relative resolution increases as x-ray energy increases, the ratio is always on the order of 1% or higher.

For diffraction studies, the width in the observed diffraction peaks is also affected by the angular divergence, the pressure gradient, the sample quality (particle size). However, if we are mainly interested in the best resolution attainable, these effects need not concern us. It is clear that the resolution that can be achieved can be no better than the best resolution on the detector itself, *i.e.* about 1%. Indeed, Buras *et. al.*[25] present a study on the optimum resolution achievable using the EDXD method on samples under ambient conditions, in which, under no circumstances resolution better than 1% was found.

The resolution as a function of angular divergence collected at the detector is

studied in the above mentioned study. An angular divergence less than 1 mrad is allowed in order to maintain a similar resolution for diffraction angles larger than 20 degrees. A smaller angular divergence is needed in order to achieve similar resolution at smaller diffraction angles.

In the ADXD method, the situation is entirely different. Two different types of sources are commonly used. In the case of a laboratory source, one normally uses the characteristic x-rays from a given target. In this case, the energy width is determined in principle by the lifetime of the corresponding atomic state, which typically translates to a few electron volts for most commonly used targets. The relative resolution in this case is therefore on the order of 0.1% or less. This assumes that we can use a single x-ray emission line. In most high pressure experiments performed on laboratory sources, it is not the case, since normally the K_{α_1} and K_{α_2} lines are close to each other and can not be distinguished. Of course, it is possible to use a monochromator to eliminate one of the lines, but this results in a large decrease in intensity and hence is seldom practiced. In practice, the energy resolution is therefore determined by the separation of the K_{α_1} and K_{α_2} lines. For Molybdenum, by fitting a gaussian over the two peaks and taking into account the intensity ratio between the two, the separation means $\frac{\Delta\lambda}{\lambda} = 0.4\%$. On a synchrotron source, a double crystal monochromator is normally used to obtain monochromatic x-rays with a band width typically much less than 0.1%.

In either case, the contribution from the energy or wavelength spread can be set to be at least a few times smaller than 1%. As long as we make the second term in Eq. (3.6) less than or equal to this, the overall resolution will be well below 1% which is a few times better than the EDXD method.

In the case of a laboratory source, the control on the magnitude of the second term in (3.6) can be achieved using a capillary tube. In fact, the capillary tube is also needed for the purpose of limiting the beamsize. A typical capillary tube used in the experiment has a diameter of 50 μm or larger and is about 20 millimeters

long, which gives an angular divergence of about 5 mrad. Although in principle a capillary with a smaller diameter can be used, the resulting intensity loss is too large to be practical. Combining this and the wavelength resolution described above, we see that the ADXD method on a laboratory source is only marginally better than the EDXD method in terms of resolution.

For a synchrotron radiation source, the natural angular spread is much less than 1 mrad in the vertical direction for high energy x-rays so much higher resolution can be attained. In fact, the angular divergence is so small that we have room to increase the angular divergence by focusing in order to gain more intensity as we will discuss in the next chapter.

3.4.2 Intensity

Another important factor for the comparison of the two diffraction methods is the time it takes to collect a diffraction pattern since it often determines whether a particular experiment is possible or not. Since the actual time varies greatly from sample to sample, we base the comparison on some simple estimates as described below.

The spectral brightness (photons/s/mm²/mrad²/0.1% bandwidth) is a good starting point for this purpose. We further restrict ourself to x-rays with energy near 17 keV, *i. e.* the Mo K α line. For laboratory sources, the value of the spectral brightness lies in the range of 10⁸ to 10¹⁰ for regular x-ray tubes, microfocus tubes and rotating anode sources. The natural width for Mo K α lines is about 7 eV, which gives a bandwidth of $\sqrt{\pi} \times 7/17479 = 0.07\%$, so the number of photons per second that can be collected within an area of 50 μm in diameter, with angular divergence within 5 mrad is between $2.7 \times (10^5 \sim 10^7)$. The spectral brightness for synchrotron sources is significantly higher. For a bending magnet source at the National Synchrotron Light Source at Brookhaven, the corresponding value is close to 10¹³, however, since the experimental setup is a large distance away from the

source, the actual gain will not be as high as the ratio of the brightness. For a similar energy bandwidth and sample area, the angular divergence that can be accepted at longer source-sample distance is very much smaller. In fact, it is about 0.0025 mrad for a sample-source distance of 20 meters. Assume the source size is 1 mm in the horizontal direction and 0.5 mm in the vertical direction, the total flux on the sample is 2×10^6 photons per second. This is comparable to the case of using laboratory sources. So for ADXD studies, if similar techniques are used, using the two sources will require almost the same amount of time. But the synchrotron will provide much higher resolution as discussed in the last section. However, if a brighter synchrotron source or focusing optics are used, it is possible to have a x-ray flux that is much higher than what can be obtained by using a laboratory source.

In EDXD studies, we can use a much wider energy bandwidth because of the low resolution of the solid state detector. If the energy bandwidth is 300 eV instead of 7 eV, we have a gain of 43 times. These estimates are in rather good agreement with what has been observed during our experiments.

The actual time it takes to get one diffraction pattern also depends on the method used to record the diffraction patterns. Both the energy dispersive detector and x-ray film are integrating detectors and they also can record an entire diffraction pattern at the same time. The major difference is the percentage of x-rays that are recorded. For solid state detector, it is close to 100%; But for x-ray film, it is below 20%. Furthermore, x-ray film has a intrinsically high background fog, this will increase the collection time another several fold in order to achieve a similar signal to noise ratio in the diffraction patterns. The recent development of the so called imaging plate system offers a much improved alternative. With the absorption efficiency of nearly 100% for 17 keV x-rays, and extremely low background, it will reduce the collection time by up to two orders of magnitude compared to using film.

By comparing the two diffraction methods, the high pressure structural study

can be loosely classified into two categories: 1) the structure of the material under study is relatively simple and so are its diffraction patterns. The diffraction pattern consists of widely separated non-overlapping peaks. The EDXD method is well suited to this case. 2) The structure of the material under study has a relatively complicated crystal structure and the peaks in its diffraction pattern are not well separated, therefore a high resolution technique is needed in order to determine its crystal structure and determine the lattice parameters accurately. Most materials fall in the latter category. To study these materials, the ADXD method is necessary, but its use requires significantly longer collection time. The ADXD method using a laboratory x-ray source without separating the K_{α} doublet will offer only marginal improvements in resolution compared to the EDXD method. The intensity available from these source seems to limit their applicability even if a high resolution monochromator is used to eliminate one of the lines in the doublets. Only synchrotron radiation sources provide adequate intensity for these types of studies.

3.5 Experimental setup for studies of crystal structures under high pressure

Briefly, the x-ray diffraction studies presented in this thesis used both the EDXD and ADXD setup. Common to both studies, we used synchrotron radiation x-rays produced by electron beams in a storage ring. An introduction to the physics of synchrotron radiation can be found in reference [18]. In the EDXD studies, the white radiation from a bending magnet beamline is used directly. In the ADXD studies, Si(111) crystals are used to obtain monochromatic radiation.

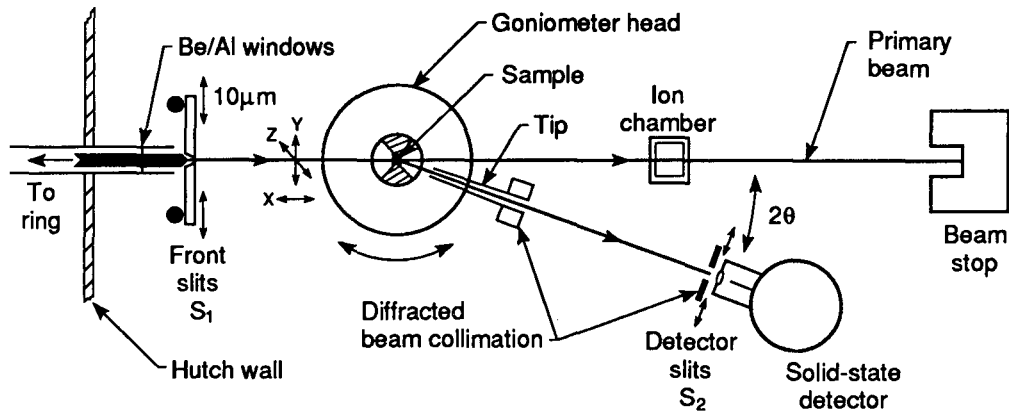
Normally, on a synchrotron radiation beamline, there are always some existing experimental setups designed for some general purpose studies. However, different requirements are necessary for our experiments. So the result experimental setup is often a hybrid involving both the existing instrumentation and additional or temporally modified instrumentation. Depending on the particular beamline that

one is working on, the instrumentation has to be specially fitted to a pre-existing arrangements. Hence, a modular experimental setup is useful under these conditions and this is what we have adopted in our experimental setup. Since most of the experimental setups need to be enclosed in a radiation hutch for safety reasons, it is also advantageous to be able to remote control the various experimental adjustments.

3.5.1 EDXD method

Figure 3.1 shows a plan view of the experimental setup in a EDXD study. The synchrotron x-ray beam enters from the right, is collimated by a set of mutually perpendicular slits to a size as small as $10\ \mu\text{m}$ in each direction. This slit is capable of moving in the two directions perpendicular to the beam so the center of the beam can be located. The second block consists of the mounting and positioning mechanism for the diamond anvil cells. The movements required in this case are translations in all three directions, and preferably a rotational movement around the vertical axis for alignment and occasional angular oscillation purposes. The intensity of the main beam that passes through the diamond anvil cell is measured in an ion chamber. The beam is then captured in a beamstop. The detection mechanism consists of a detector sitting at a fixed angle 2θ with respect to the main beam, although from time to time, it is desirable to change the angle to different values. So it is preferred that it sits on a rotational arm that rotates around the sample. The pair of detector slits S_2 are used to define the angular acceptance of the detector. The first slit collimates in the vertical direction and is a rather coarse adjustment. The second slit collimates in the horizontal direction and is related to the resolution of detection as reflected in Equation (3.6) thus requires fine adjustments. A tip with horizontal opening as small as $20\ \mu\text{m}$ is sometimes used to discriminate against the inelastic scattering from the diamond anvils to reduce the background.

Two pictures of one of our particular setups are shown in Fig. 3.2. The synchrotron beam coming from inside the pipe (A) is first collimated by a set of mo-



XBL 904-5832
lg/Mac

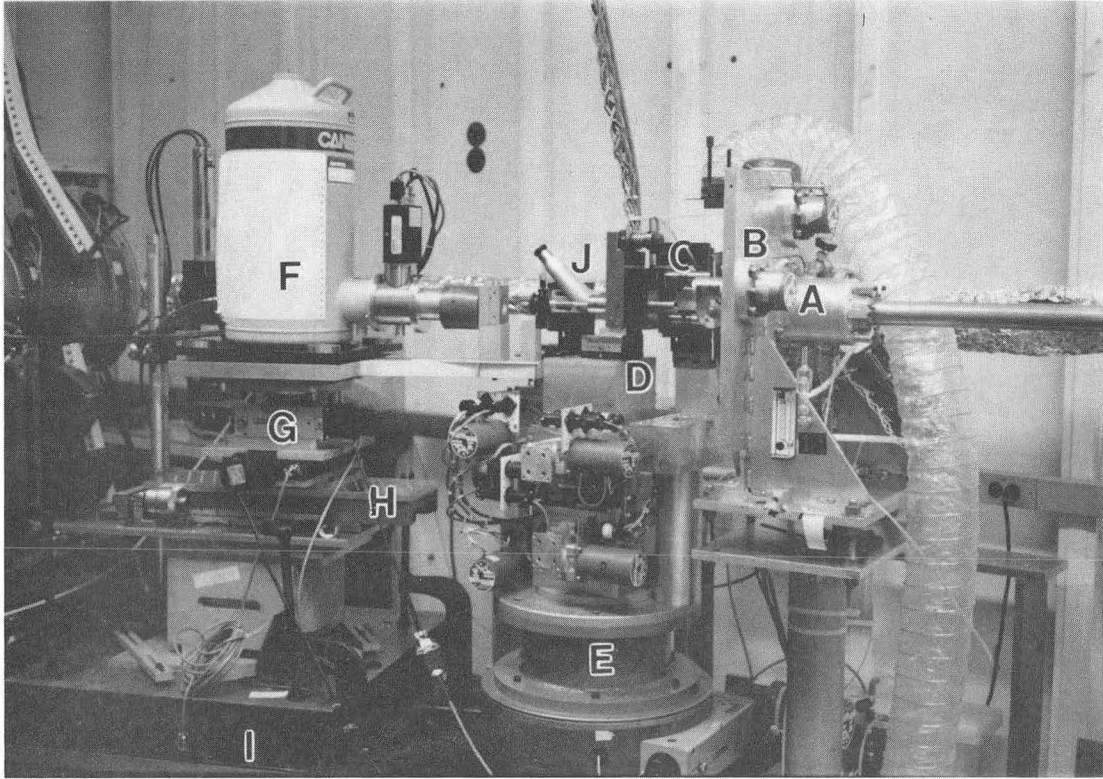
Figure 3.1: A schematic of a generic setup for Energy Dispersive X-ray Diffraction (EDXD) experiments. There are three essential parts: (1) the slit system, which consists of a pair of adjustable or fixed slits with the smallest possible size below $10\ \mu\text{m}$; (2) the diamond cell mounting block, also called the first axis, which consists of three motorized translational adjustments, two manual translational adjustments, and two rotational adjustments; (3) the detector system, which consists of a solid state detector, a set of slits to control the acceptance of the detector, and an optional tip to provide some spatial discrimination against the scattering from the diamonds. An ion chamber is used to record the transmitted x-ray intensity to facilitate alignment process.

torized slits (B) to a size of few hundred microns. Then it is further collimated by a set of fixed slits (C) with 10 μm opening in each direction. This slit assembly is equipped with motorized translational as well as rotational adjustments in both the vertical and horizontal directions since the slit is made of thick tantalum pieces so rotation is necessary to allow proper alignment. The microbeam of x-ray is sent through the diamond anvil cell (D) which itself was mounted on a stage (E) capable of translation in all three directions and rotation around the vertical axis. This vertical axis is called the first axis. The solid state detector along with the accepting slits and the tip (F) is on a stage (G) with motorized translation adjustment in the horizontal and vertical direction. This stage is placed on a precision slide (H) so quick and reproducible movement of the detector can be achieved for viewing the sample through a microscope (J). The slide sits on a long rotation arm (I) that can rotate around the same axis as the first axis. A microscope (J) with micrometer adjustments in three directions also sits on two precision slides to facilitate quick and reproducible repositioning.

There are several independent procedures in an experiment. They are presented in separate paragraphs that follow.

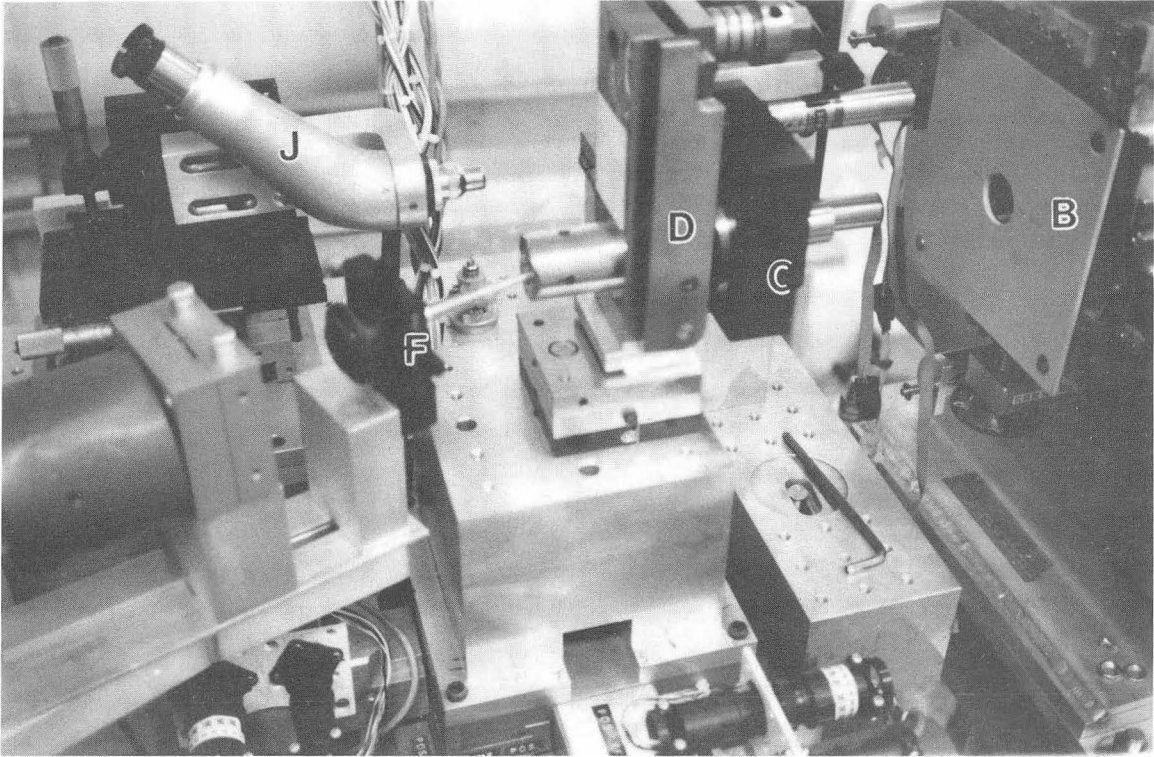
(1) The alignment of the entrance slits: Starting with a large beam, the proper angle of the fixed slit with respect to the beam can be easily found by measuring the transmitted intensity while rotating the slits in both the vertical and the horizontal directions. The center of the beam can be located by scanning the slits in the vertical and the horizontal directions. The motorized slits are rather coarse and are used to reduce the general scattering background.

(2) The alignment of the sample stage. There are two independent procedures to the alignment of the sample stage. The first one consists of positioning the sample on the axis of rotation. The second part is to bring the axis of rotation into the microbeam. The reason for aligning the sample on the axis of rotation is several fold. (a) In order to be able to change the angle of diffraction without having to



XBB 890-8939

Figure 3.2(a)



XBB 890-8938

Figure 3.2(b)

Figure 3.2: Photographs of one of the EDXD experimental setup used in our studies. The synchrotron beam coming from inside the pipe (A) is first collimated by a set of motorized slits (B) to a size of few hundred microns. Then it is further collimated by a set of fixed slits (C) with $10\ \mu\text{m}$ opening in each directions. This slit assembly is equipped with two motorized translational as well as rotational adjustments since the slit is made of thick tantalum pieces so rotation is necessary to allow proper alignment. The microbeam of x-ray is send through the diamond anvil cell (D) which itself was mounted on a stage (E) capable of translation in all three directions and rotation around the vertical axis. This vertical axis is called the first axis. The solid state detector along with the accepting slits and the tip (F) is on a stage (G) with motorized translation adjustment in the horizontal and vertical direction. This stage is placed on a precision slide (H) so quick and reproducible movements of the detector can be achieved for viewing the sample through a microscope(J). The slide sits on a long rotation arm (I) that can rotate around the same axis as the first axis. A microscope (J) with micrometer adjustments in three directions also sits on two precision slides to facilitate quick and reproducible repositioning.

recalibrate the angle of diffraction after each time the angle is changed, the sample should be made to coincide with the axis of rotation of the detector arm. But in most $\theta - 2\theta$ goniometer designs, the two axes of rotation are prealigned to a high degree of accuracy. (b) This axis of rotation also serves as an absolute reference point because its position is determined by the rotation alone and is independent of horizontal translational adjustments which are located on the rotating stage. (c) By putting the sample at the rotation axis, we can rock the sample without going out of alignment in cases where one needs to reduce the effect of preferred orientation in the sample.

In order to find the axis of rotation, we can mount a cross-hair horizontally at the sample position, by rotating the stage and observing the center of the cross hair through a fixed microscope, one can easily tell whether the center of the cross hair coincides with the axis of rotation. By noting the departure along each of the horizontal axis (X and Y), we can adjust the translation stage to make the center of the cross hair appears stationary in the microscope. This process can also be carried out using a vertical pin and adjust the two directions independently. Once the axis of rotation is found, a vertical pin is aligned to it. This position is then transferred to a reference microscope in the horizontal direction. This microscope is used in putting the sample in position. The microscope is equipped with a cross hair to define the position in the horizontal (Y) and the vertical (Z) directions. By correcting for the difference in the focusing distance due to the existence of diamond anvil, one can use the criterion that the sample is in proper focusing condition to make sure the sample is in the correct position along the X direction as well. The formula to be used is simply

$$\Delta x = \left(1 - \frac{1}{n}\right)d_c$$

where n is the reflective index of diamond and d_c is the thickness of the diamond anvil on the cylinder side. The actual distance between the sample and the focusing plane is shortened by the above amount due to the existence of the diamond. This

way, the sample can be positioned within a few microns of the desired point in the Y and Z direction. The accuracy in the X direction is somewhat less due to deformations of the diamond anvil at high pressures.

In order to align the axis of rotation into the beam, an auxiliary adjustment in the Y direction is necessary. By using a sharp pin and scanning it across the beam, one can determine the distance between the axis of rotation and the x-ray beam, the whole stage is moved subsequently. For experiments using a bending magnet or wiggler beamline where the x-ray beam is wide in the horizontal direction, sometimes one can move the slits instead of the entire first axis stage.

(3) The energy calibration of the solid state detector. The signal from the preamplifier of the solid state detector is fed into a spectroscopic amplifier to convert the current pulses into gaussian shaped voltage pulses, then it is send to a Multi-Channel Analyzer (MCA) where the peak height of each pulse is digitized and histogrammed as a function of the peak height. This system requires frequent energy calibrations. The calibration is done by using a radioactive source to excite a set of secondary targets, the characteristic fluorescences with known energies are recorded in the MCA. A linear regression can be used to relate the channel numbers to the x-ray energies.

(4) The alignment of the solid state detector. In order to perform diffraction experiments, the slits in front of the detector and the tip need to be precisely aligned. The opening in the slits is determined by a combination of resolution desired and counting rate available for a given sample. Normally, an angular opening of 1 mrad or less with respect to the sample is used so there is no significant degradation in resolution due to the angular divergence. The opening of the tip is determined by the nature of the sample. For samples with low scattering power, the discrimination against the diamond background is more critical. For samples with high scattering power, tips with large openings or no tip at all may be used. The exact desired size can be estimated by forming the pinhole image of the detector slit on the sample area. Of course, the finer the tip opening, the harder it is to align the tip into

position. Once the detector slit is set, one needs to move the tip so it will allow the diffracted beam into the detector.

(5) The calibration of diffraction angle. In order to use the Bragg law to calculate the lattice spacings, one needs to know precisely the angle at which the detector is sitting. This is accomplished by using a standard material with well characterized structure parameters, usually a metal like Au, or Pt, under the ambient condition. The standard is aligned in the same way as the sample and the diffraction patterns obtained. From the known lattice parameters and measured energies, the detector angle can be easily calculated. Alternatively, one can use the method proposed by Brister *et al.*[27] in the event no standards are available.

3.5.2 ADXD method

Compared to the setup used in the EDXD method, the ADXD setup is much simpler. The incident beam slit system is essentially identical to that used in the EDXD method. The diffracted intensity from samples under high pressure is very low from even the most intense synchrotron radiation sources, thus one can only be content with relatively large beam sizes ($\geq 100\mu\text{m}$) in order to be able to record a diffraction pattern in a practical time period(a few hours). It is much simpler to collimate x ray beams to these sizes.

The alignment of diamond anvil cell is much simpler too. The rotational adjustment is less critical because the detectors used can cover a larger solid angle than the solid state detector used in the EDXD studies so an average over the orientation is possible. Similar to the procedure described in the last section, the alignment is also achieved through a reference microscope.

The only part that is different and requires some discussion is the detecting mechanism. In most of the experiments described here, Kodak direct exposure x-ray film was used to record the diffraction patterns. The film is mounted either on a cassette attached to the diamond anvil cell as described in [43] or more recently on

a specially made cassette that has mounting structures in several different radii. A picture of this cassette can be found in Figure 4.7 in the next chapter. The curved structures on the cassette were made to a high precision and the film is spring loaded to ensure close fitting. The origin of the cylindrical mounting structure on the camera were aligned to the sample position by the aid of a removable alignment tool on which the origin is marked. It is designed that this tool can be attached to the cassette with high reproducibility. The reference microscope can again be used to facilitate this alignment. If proper alignment is achieved this way, since the radius of curvature of the film is given by the mechanical specification of the cassette, it is straightforward to calculate the lattice spacings of the sample under study. Only occasionally does the alignment scheme need to be checked by performing diffraction experiment on a standard.

In some part of the study, we have also exploited the use of a new detector system, the phosphors imaging plate system. A more detail description is presented in the next chapter.

The limited intensity in a micro beam achieved by using pinhole or slits is addressed extensively in next chapter, where we describe a rather large effort to make use of a focussing system to obtain higher intensities. Since the effort is relatively independent, we will deal with it in a separate chapter.

3.6 Data reduction

In the EDXD study, the diffraction data are in the form of intensity as a function of energy. We use a peak fitting routine to locate precisely the centroid of each diffraction peak and the integrated area under the peak along with their standard deviations. Through the use of the Bragg law, we convert the energies to lattice spacings. After obtaining the lattice spacings, we use a least square method to refine the lattice parameters and calculate the unit cell volumes. Along with the pressure measurement, the basic pressure volume relation is obtained. This relation is often

fitted to a empirical equation of state formulation. A new fitting algorithm taking into account the appropriate statistical weights is presented in Appendix A.

In the ADXD studies, the diffraction pattern recorded on film is usually read on a film reader, the centroids of diffraction peaks are directly read by eye. In the case where intensity data or more precise position data are desired, the film is also scanned on a microdensitometer to obtain the optical density as a function of position. Then this information is processed the same way as a EDXD diffraction pattern as described above. In general, the ADXD method is capable of achieving higher resolution compared to the EDXD method.

Chapter 4

The Development of a Focusing System for X-rays

In the last chapter, we have described the x-ray diffraction techniques used in the high pressure structural study experiment. Common to these techniques is the requirement for a small intense x-ray beam. In this chapter, we describe the development of a focusing system that is particularly suited to these experiments. We start with some simple calculations illustrating the necessity of a small size beam. Then we proceed to discuss the possible gain in intensity with a focusing system based on purely physical grounds. A discussion of the reason for choosing the particular focusing geometry that we used is then presented. After a brief discussion of the multilayer coating for the x-ray range, the design considerations, operation, and characterization of the Kirkpatrick-Baez focusing system is described. We look at the result of an initial application of this system to the x-ray diffraction studies under high pressure and conclude with some remarks about the future developments of such a focusing system.

4.1 The requirement for a small beam size in high pressure studies

The requirement for a small beam size in high pressure research can be seen from the following simple consideration. Since the pressure is equal to the applied force divided by the area, great amplifications can be achieved by suitably designing the pressure generating apparatus. For a nominal force of 1 Newton on a surface area of $1 \mu\text{m}^2$, the pressure is 10^{12} Pascal = 1,000 GPa. To generate the same pressure on a 1 cm^2 surface, it would require a force of 10^{12} Newtons which is clearly prohibitive. For comparison, the pressure at the center of the Earth is about 340 GPa, so it is evident that pressures above 100 GPa can be very useful in geophysical research. But the application is not limited to geophysical research because under these pressures there are fundamental changes in the properties of most materials. As an example, a large class of solids which are insulators under ambient conditions exhibit metallic behavior (for example, there are some recent reports on metallic hydrogen[28]). The nature of these transformations and structural properties in general are of great interest to condensed matter physics.

Experimentally, the above considerations are exploited in the attempts of generating ultra high pressures. With the development of diamond anvil cell techniques, static pressures in excess of 500 GPa[29] have been generated in the laboratory. As expected, the area over which such high pressure exists is indeed very small. In this particular experiment, the area over which the highest pressure existed was estimated to have a diameter of $2 \mu\text{m}$. Figure 4.1 shows a typical pressure profile in high pressure studies. It can be seen that the pressure gradient is rather large, and the region with the highest pressure is only about $10 \mu\text{m}$ in diameter. In order to minimize the effects of pressure gradients on one's measurements, a beam size equal to or smaller than this is desired.

The above experiment was performed using the energy dispersive x-ray diffraction (EDXD) method described in the last chapter, with the incident x-ray radiation

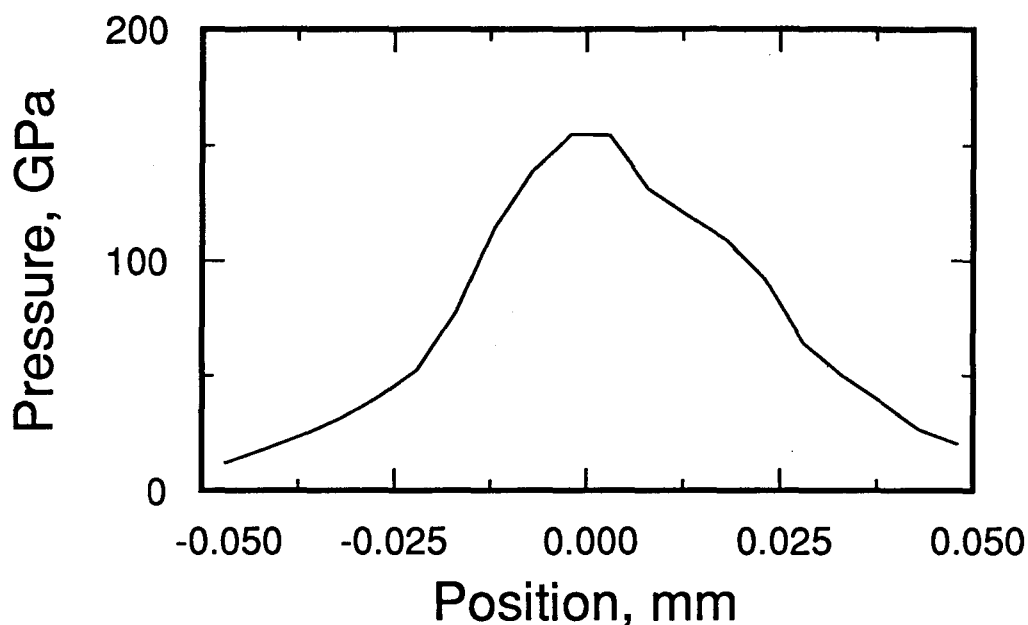


Figure 4.1: A typical pressure distribution at high peak pressure in a diamond anvil cell apparatus for ultra high pressure studies. The sample in this case was rhenium.

being collimated by a set of slits with $10\ \mu\text{m}$ openings. Such an approach has been rather successful to date. In fact, most diffraction data above the pressure of 100 GPa are obtained this way. There are two drawbacks to this method, however. One is the difficulty of producing even smaller beam sizes. It is increasingly more difficult to produce slits or pinholes with sizes on the order of few microns or less with sufficient stopping power for high energy x-rays. The second drawback comes from the use of energy dispersive detectors which have intrinsically low energy resolution for diffraction studies. As discussed in the last chapter, for a large class of materials, the resolution provided by the EDXD method is inadequate. The angular dispersive x-ray diffraction (ADX) method is needed. However, as noted there, by using the ADXD method, one suffers a large loss of flux which makes the experiment impractical for samples of this size. A focusing system can increase the intensity in the beam and is a natural candidate for enabling such studies. A focusing system also provides the possibility of achieving much smaller beam sizes without much sacrifice of intensity. It may be the only practical way to obtain intense x-ray beams with a

size on the order of $1 \mu\text{m}$. In this regard, such a development is necessary and very timely.

4.2 Advantages of using a focusing system

The intensity available at the sample point is given by the product of irradiance, the beam size and the converging solid angle. No matter what one does to the x-ray beam, one cannot increase the value of irradiance over the value of the source brightness (for x-rays, the index of reflection for all materials is close to 1 and has little effect on the value of irradiance). Therefore for a source with large emitting area (real space) and emitting into all the solid angle (momentum space), there is no possible gain in intensity by focusing. For sources with finite size in the real space and/or momentum space, a gain is possible depending on the actual condition.

It is useful to use phase space terminology in discussing the focusing processes. In our case, the allowed acceptance in phase space can be characterized by a small size in both vertical and horizontal directions in real space and a limited angular divergence in the scattering plane and a large angular divergence in the plane perpendicular to it. For simplicity, we only consider the scattering plane here because the possible gain in the other plane is certainly greater. Since the x-rays originating from synchrotron radiation in a bending magnet or wiggler is nearly 100% polarized, it is advantageous to perform diffraction in the plane perpendicular to the plane of polarization. Therefore, we need to consider the vertical plane as the scattering plane. For an angular divergence of 1 mrad at a diffraction angle of 0.5 rad, we can achieve a relative peak width of 0.2% which is significantly better than what can be achieved in the EDXD studies. So we can set our allowable angular divergence of the beam at the sample to be 1 mrad. Figure 4.2 compares the allowed phase space region with the phase space parameters of the LBL-EXXON wiggler beamline VI-1 at Stanford Synchrotron Radiation Laboratory (SSRL). It is seen that the angular divergence provided by the source is several times smaller than the allowed diver-

gence while the source size in the real space is several orders of magnitude larger than the allowed size which we have arbitrarily set to $10 \mu\text{m}$. For a bending magnet and wiggler source, σ_s , the standard deviation in the angular distribution is usually determined by the energy of the electron beam and the ratio of the energy of the x-ray of interest to the critical energy. Using the parameters for SSRL's SPEAR ring and 16 keV x-ray photons, we have a value of about $60 \mu\text{rad}$ [30]. This is much smaller than our experimentally allowed angular divergence of 0.42 mrad (1σ) or 1 mrad (FWHM). The source size is much larger than our allowed beam size. It is thus clear that one can gain intensity by increasing the angular divergence at the sample using a suitable focusing device. The gain is probably close to 7 fold in this direction in this particular situation.

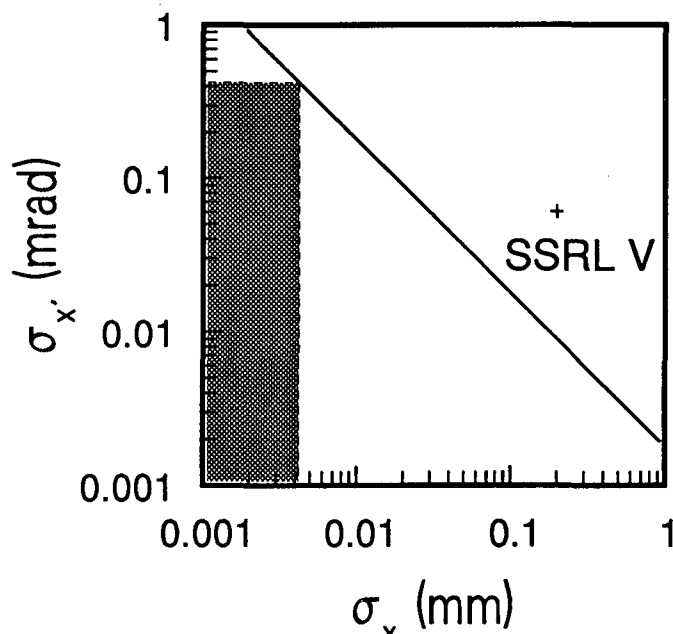


Figure 4.2: A comparison of the allowable region in the phase space for diffraction experiments and the location of a typical synchrotron source, here chosen to be the LBL- EXXON wiggler beamline at SSRL. Only the vertical direction is considered.

In reality, one always performs the experiment at a certain distance d away from the source. Depending on the source characteristics and the distance, there can be major modifications to the above discussion. Again, for simplicity, we consider

a one dimensional source, its size and angular divergence can be characterized by two gaussian distributions with standard deviation σ_s and $\sigma_{s'}$ respectively. At a distance d from the source, the distribution in the phase space can be represented approximately by two gaussian distributions with standard deviations $\sqrt{\sigma_s^2 + d^2\sigma_{s'}^2}$ and $\sigma_{s'}/\sqrt{1 + d^2\sigma_{s'}^2/\sigma_s^2}$. If we have an optical system with real space aperture σ_e and angular acceptance $\sigma_{e'}$ at this point, we can obtain the effective total phase space acceptance of the optical system as

$$\sigma = \frac{\text{total intensity}}{\text{peak brightness}} = \frac{\pi}{\sqrt{(1/\sigma_s^2 + 1/\sigma_e^2)(1/\sigma_{s'}^2 + 1/\sigma_{e'}^2)}} \frac{1}{\sqrt{1 + (d/d_c)^2}}$$

where $d_c = \sqrt{(\sigma_s^2 + \sigma_e^2)(1/\sigma_{s'}^2 + 1/\sigma_{e'}^2)}$. Thus, if $\sigma_e \ll \sigma_s$, it is rather inefficient to use a pinhole to obtain small size beams. Figure 4.3 gives a comparison between a 10 μm pinhole optics and a hypothetical focusing optics with 100 μm aperture and $\sigma_{e'} \gg \sigma_{s'}$. In principle, one can increase the aperture of the focusing system until one reaches the limiting acceptance, therefore the gain can be very high indeed. This gain increases as the distance is increases, when $d \gg d_c$, the gain is proportional to the distance. In this case, the source behaves much like a point source. For the indicated parameters, the gain is more than one order of magnitude at a distance of 20 meters away from the source with the indicated focusing system. If one takes into account that the actual sources are always two dimensional, so if one focuses in both directions, one should be able to gain more than two orders of magnitude in intensity.

4.3 Focusing optics in the x-ray region

Since the index of refraction for all materials has a value very close to 1 in the x-ray region, it is unrealistic to construct refractive optics similar to the ones used in visible optics to manipulate x-rays. In order to focus x-rays, different approaches are necessary. Various methods have been proposed and some of them have been tried. We shall not try to be complete in numerating all the different approaches

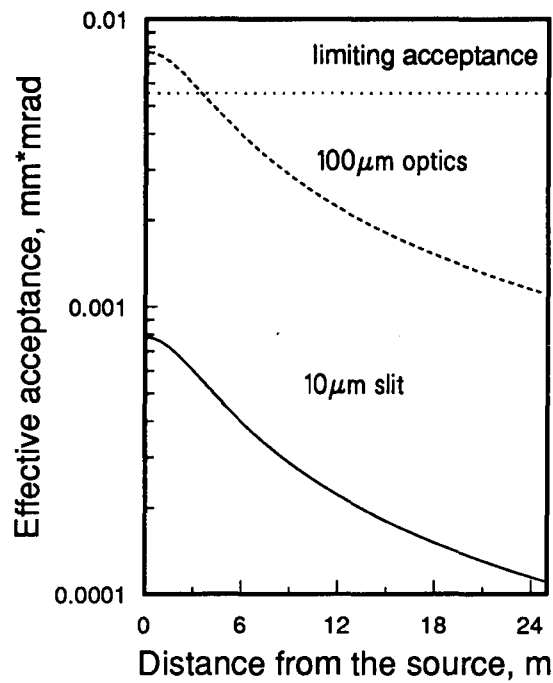


Figure 4.3: The effective acceptance for a 10 μm slit and a hypothetical optical system with 100 μm acceptance at a distance d away from the source. The allowable maximum acceptance is also plotted for comparison. In this calculation, we have assumed $\sigma_s = 0.21$ mm, $\sigma_{s'} = 0.06$ mrad, and $\sigma_{e'} = 0.42$ mrad and only one dimension is considered. The gain in intensity can be more than 10 fold in each direction at distances greater than 20 meters in this case.

here but rather concentrate on a collection of those closely related to what we would like to achieve, *i.e.* a small beam size.

4.3.1 Fresnel zone plate focusing system

Focusing using Fresnel zone plates has no special advantage in the visible region of the spectrum, but it has found some important applications in the x-ray region. Because it is extremely difficult to make thick zone plates of absorbing material, its use has been mainly limited to relatively low energy x-rays ($E < 1$ keV). A focused beam size as small as 300 Å has been achieved at an x-ray wavelength about 40 Å. Recently a multilayer zone plate fabricated using sputtering and slicing techniques has been used to focus x-rays of significantly higher energy ($E = 8$ keV)[31]. Using a 10 μm pinhole as the entrance slit, a focused beam size of 1 μm in diameter was claimed in the experiment.

Despite this, it remains to be seen whether such a zone plate focusing system will be useful in the hard x-ray ($E > 10$ keV) range. There is also the problem of intensity. Since only small zone plates of sufficient quality can be made at this time, the intensity in the focused beam is very low. In an earlier report[32] by the same group, the intensity they achieved at the focused spot with 8 keV monochromatic radiation was only 3×10^4 photons/s. This is three to four orders of magnitude lower than what is needed for diffraction studies. Much development is needed in order to see whether it is feasible to achieve much higher intensities.

4.3.2 Focusing using crystals

Focusing using single crystals is probably the most widely used method in the hard x-ray region. Most work in the early days was concerned with unit magnification where the applications have mainly been high flux monochromators and spectrometers. Two well known geometries are the Johann[33] and Johansson[34] geometry. In the Johann geometry, the crystal is bent to a radius of curvature R , while in the

Johansson geometry, the crystal is first ground to a radius of curvature R and then bent so that the Bragg plane forms a circular cylinder of radius R . In both cases, the source and image sit on a Rowland circle whose diameter equals the radius of curvature of the Bragg plane in the crystal to ensure the Bragg condition for diffraction is obeyed. In the Johann geometry, in order to maintain the same Bragg angle across the crystal surface, the crystal surface actually departs from the proper shape for point to point focusing, so there are significant geometric aberrations. The Johansson geometry eliminated those but it is much more difficult to fabricate.

The two geometries are used for unit magnification focusing only. In order to form images of non unit magnifications, one needs to use either asymmetrically cut crystals (the reflecting Bragg plane is not parallel to the surface of the crystal) or place the source outside the Rowland circle. In either case, one has some major difficulties to overcome, as we shall see.

In an asymmetrically cut crystal, the Bragg plane of interest is not parallel to the surface, so the angle of reflection with respect to the surface normal is different from the angle of incidence. This is necessary for focusing at a non-unit magnification while maintaining the source and the focused image on the Rowland circle. This direction of development is largely unexplored. Successful focusing systems may be possible to develop along this line, although the combination of high quality surface finish both in terms of surface smoothness and shape still represents major challenges. The need to use good quality single crystals and bending them adds to the degree of difficulty as well.

If one follows the unmodified Johann or Johansson geometry and tries to achieve non-unit magnification by placing the source and image out of the Rowland circle, one is required to bend the single crystal with a very small radius of curvature (on the order of 10 centimeters). This will be explained in the next section. It is exceedingly difficult to bend a single crystal into such a small radius of curvature and still maintain the quality of the single crystal.

Crystals can also be used in transmission geometry. The Guinier-Tennevin method[35, 36] represents an interesting example. A thin flat single crystal plate is used in transmission geometry and Bragg planes close to being perpendicular to the crystal surface are used to reflect x-rays. This is similar to the transmission grating in the visible light wavelength region. Such a geometry can achieve a point-to-line focussing. By using two thin plates in a mutually perpendicular geometry, it should be possible to design a system to achieve point-to-point focusing. Such a system is not directly applicable to the present situation in two regards. (1) In such a system, different parts of the crystal reflect x-rays of different energy while in our case we would like all parts of the crystal to reflect x-rays of the same energy; (2) The original method uses a flat plate and the system has unit magnification in the focusing direction while we would like a large demagnification. Although bending of a suitable single crystal also offers some interesting possibilities, they are largely unexplored as well because these possibilities are rather unique and only become available on synchrotron radiation sources.

4.3.3 Focusing using total reflection mirrors

Since the refractive index for most materials at x-ray wavelengths is slightly less than unity, x-rays incident on the material are totally reflected when the glancing angle is smaller than the critical angle given below. The complex index of refraction is described by

$$n = 1 - \delta - i\beta, \quad (4.1)$$

where δ and β for elemental materials at a given x-ray wavelength λ can be expressed as

$$\delta = \frac{N_0 r_e \lambda^2}{2\pi} (f + \Delta f'),$$

$$\beta = \frac{N_0 r_e \lambda^2}{2\pi} \Delta f''.$$

Here r_e is the classical radius of the electron, N_0 is the number density of atoms and $f, \Delta f', \Delta f''$ are the scattering factor and the anomalous scattering factors as

discussed in the last chapter. As an approximation, let $f = Z, \Delta f' = 0, \Delta f'' = 0$, the critical angle is

$$\theta_c = \sqrt{2\delta} = 2.99 \times 10^{-23} \sqrt{n_e \lambda},$$

where θ_c is given in radians, $n_e = N_0 Z$ is the electron density in electrons/cm³, and the wavelength λ is in Å. The critical angle is very small for relatively high energies. For example, $\theta_c = 0.3$ deg for Pt at 16 keV ($\lambda = 0.775$ Å).

The small critical angle has made total reflection mirrors necessarily big for a useful collecting solid angle. Of course, since the wavelength of x-rays are much shorter than the visible light, the requirement on the surface quality are also more stringent.

Despite these difficulties, focusing systems with a demagnification up to about 10 have been successfully made. A larger demagnification mirror which focuses in both directions is extremely difficult to fabricate and very costly. No attempts have been made in this regard.

4.3.4 A new possibility: focusing using multilayer coated mirrors

As described above, existing geometries for focusing systems in the x-ray region suffer from several drawbacks when a very small beam size is desired. Simple extensions of these techniques are not able to reach this goal. Innovative ideas and new techniques are very much in need.

Recent advancements in the fabrication of multilayer coatings for x-ray wavelengths provide a golden opportunity in developing new focusing systems for x-rays. In the following sections, we describe the concept, the physics, and the fabrication of multilayer coatings and a focusing system using these multilayer coatings.

4.4 An introduction to reflective optics

To understand the difficulty mentioned in the last section for making a large demagnification focusing system using both bent crystals and total reflection mirrors, and to understand the unique properties of multilayer coatings, it is necessary to describe some of the basic properties of reflective optics. Probably the simplest focusing system, a concave spherical mirror, when used near normal incidence, forms good real images of points near the optical axis. The images of off-axis points become progressively degraded. In fact, the image of a point source by no means resembles the source as glancing incidence is approached. At two different distances from the mirror, two mutually perpendicular lines are observed and they represent the best focusing conditions. Within the paraxial approximation, the focusing properties of such a mirror can be described by the Coddington equations:

for tangential rays

$$\frac{1}{u} + \frac{1}{v_t} = \frac{1}{f_t} \quad (4.2)$$

and for sagittal rays

$$\frac{1}{u} + \frac{1}{v_s} = \frac{1}{f_s} \quad (4.3)$$

where u, v and f are the object, image distances to the mirror vertex and the focal lengths, respectively. The subscript t and s refer to the tangential and sagittal rays which are in, and perpendicular to, the plane of incidence. $f_t = (R/2) \sin \theta$, $f_s = R/(2 \sin \theta)$ with θ the angle of glancing incidence, and R the radius of curvature of the mirror. For nonspherical mirrors, R should be replaced with the radius of curvature in the appropriate planes. For small θ , the two focal distances differ by a great amount. This particular aberration in the image formation process is termed astigmatism.

To correct for the severe astigmatism, Kirkpatrick and Baez[37] use two spherical mirrors that are perpendicular with respect to each other so that the sagittal rays with respect to the first mirror that are weakly focused, become the tangential

rays of the second mirror, and are strongly focused. The curvature of the second mirror and glancing incidence angle are designed so that this focus overlaps with the tangential focal plane of the first mirror. Since sagittal focusing is so weak for small incidence angles, only the tangential focusing needs to be considered.

Although this simple system eliminates most of the astigmatism, it still suffers from other optical aberrations. For our application, since we need not be concerned with a large field of view, we can restrict ourselves to the image formation of an on-axis point source. As shown in Fig. 4.4, rays originating from the point source but striking different parts of the mirror will not cross at the supposed focal point exactly. The minimum waist size of these rays is the aberration we are concerned with. For simplicity, instead of finding the minimum waist along the beam, we approximate it by the spreading in the gaussian plane (its position is calculated from the Coddington equation). An analytical formula can be found. However, for small incidence angle, Kirkpatrick and Baez[37] derived an expression, which can be written as

$$\delta = \frac{3 w^2}{2 R}, \quad (4.4)$$

where w is the half width of the illuminated part of the mirror and R is the radius of curvature in the tangential plane of the mirror. For the mirror used in our experiment, the maximum mirror half width is 1.25 cm, and $R = 15$ m, which gives a maximum deviation of $10 \mu\text{m}$. This is within 10% of the value of an exact calculation. This value is the full extent of the beam if the whole mirror is illuminated. If one takes into account the intensity distribution and considers the full width at half maximum and the actual reduced illumination area due to aperture and finite band pass of the multilayer coating, this value is much smaller than $10 \mu\text{m}$.

While the deviation does not depend on the incidence angle, the angle that the mirror subtends to the source is linearly proportional to the glancing incidence angle, so for the same size mirror, a larger glancing incidence angle is desired.

Now we can look at the reason why the total external reflection mirror and bent

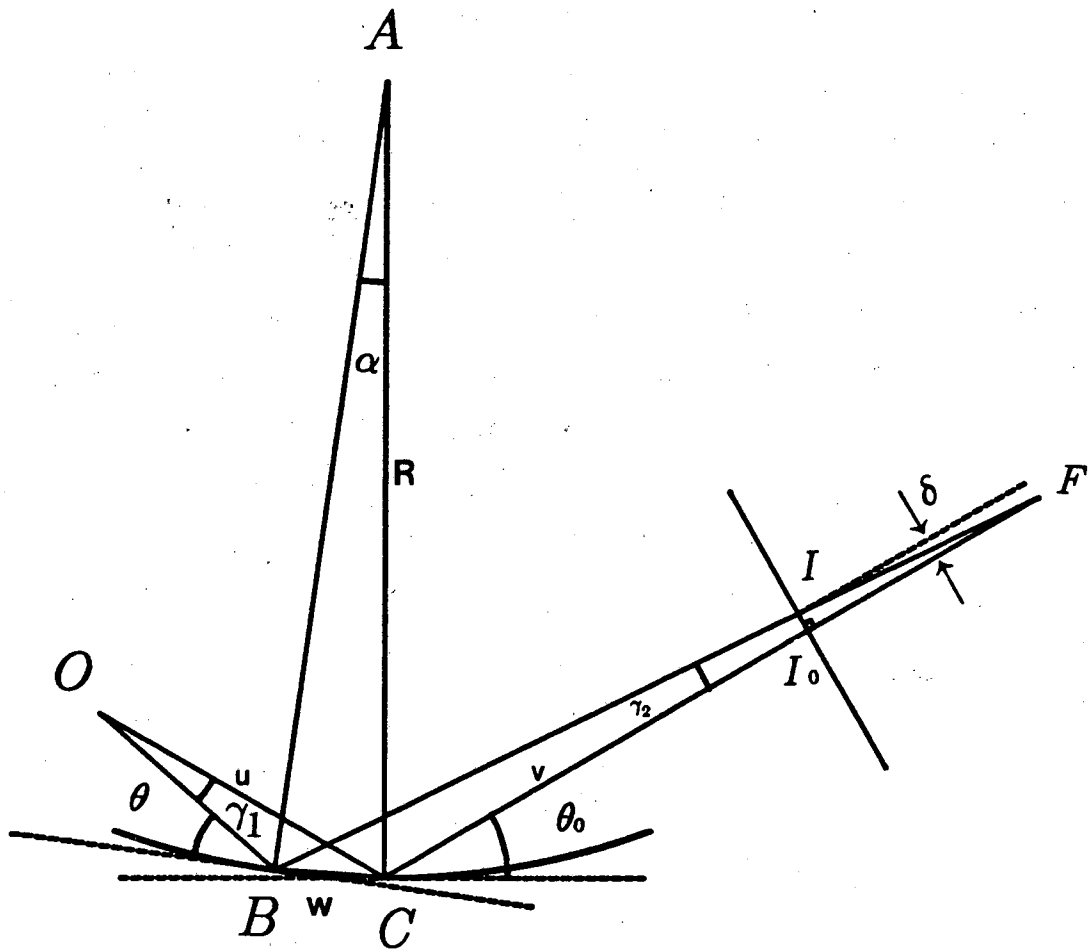


Figure 4.4: Image formation of a reflective concave spherical surface. Only the tangential direction is considered. The sagittal focusing is very weak for a small glancing incidence angle θ_0 and is neglected here. If the rays pass through the center C of the mirror, an image is formed at I_0 according to the Coddington equation (4.2 and 4.3). The rays striking at point B will not cross at I_0 at the focal plane, the deviation δ is the total aberration. The first order term in its expansion in terms of w contributes most for the parameters that concern us and is named spherical aberration.

crystal do not fit our requirements very well. Since the source size on a typical synchrotron radiation source is on the order of one millimeter, a large demagnification is necessary in order to achieve a focused beam spot on the order of $10\ \mu\text{m}$. Normally, an experimental station is on the order of 20 m away from the source, this means the corresponding focal length of the system must be on the order of 10 cm. Now recall that the focal length is given by $f = (R/2) \sin \theta$, so if θ is large, then R is on the order of 10 cm to 1 m. This small radius of curvature is difficult to achieve by bending a single crystal and at the same time maintaining its good crystalline quality. On the other hand, if θ is very small, one is restricted by space requirements as well besides the high cost of making a relatively large mirror because a longer mirror takes up more space between the center of the mirror to the focal point.

There is a further restriction on the use of crystals because all single crystals have a very narrow band pass (on the order of 0.003 degree). But as can be seen from Fig. 4.4, the rays striking at points different from the mirror vertex have different angles of incidence from those striking at the mirror vertex. The differences are rather large comparing to the angular band pass, and this is the reason why in the Johann geometry, one bends the crystal to a different radius of curvature than what is required by the focusing geometry, or in the Johansson geometry, the crystal has to be ground into a particular shape. As we shall see, multilayer coating on the other hand has a much wider band pass, so a similar limitation is not so severe and a spherical substrate correct for focusing purpose can be used.

4.5 Multilayer reflective coatings for x-rays

Multilayer reflective and antireflective coatings are standard items in optical technology for the visible and nearby UV and IR spectral regions. Similar developments for x-rays actually preceded these applications by about 10 years. However, because of the much greater difficulty of the problem, not much progress has been made in making useful multilayer coatings for x-rays for a long period of time. About a

decade ago, developments in the sputtering [38] and electron beam evaporation[39] techniques made possible stable, good quality multilayers. We would like to briefly describe the principles of the multilayer reflective coatings and the design and fabrication process of the multilayer coatings used in the current experiment.

4.5.1 Principles

Briefly, a multilayer reflective coating is a structure in which the index of refraction varies as a function of depth into the structure. In the x-ray wavelength region, the indices of refraction for all materials are close to 1 with the difference from 1 being proportional to the total electron densities in a given material, as was discussed earlier in section 4.3.3. Therefore, a multilayer coating in the x-ray region is obtained by depositing different materials as a function of depth. In the current experiments, we have used only periodic multilayers. They are made by depositing alternating layers of two materials with very different atomic numbers and/or densities. Fig. 4.5 shows a schematic drawing of the cross section of the multilayer structure. The material A consists mostly of elements with low atomic numbers and each individual layer has a thickness of d_A ; the material B consists mostly of elements with high atomic numbers, each layer has a thickness of d_B . In our study, we have used elemental carbon and tungsten for A and B respectively. When the multilayer structure is illuminated by a parallel, monochromatic light of wavelength λ , the reflectivity of the multilayer with period $d = d_A + d_B$ as a function of glancing incidence angle θ , reaches a maximum when the the reflected rays from individual interfaces are in phase. The angles correspond to the maxima are given by the same Bragg condition as in a crystal:

$$2d \sin \theta = n\lambda, \quad (4.5)$$

where n is the order of the reflection.

For hard x-rays with a wavelength about 1 Å, when the glancing angle of incidence is a few degrees, the period d should be in the range of 10's of Å. This fact

is partially responsible for the difficulty of making high quality multilayers that are suitable for x-ray applications.

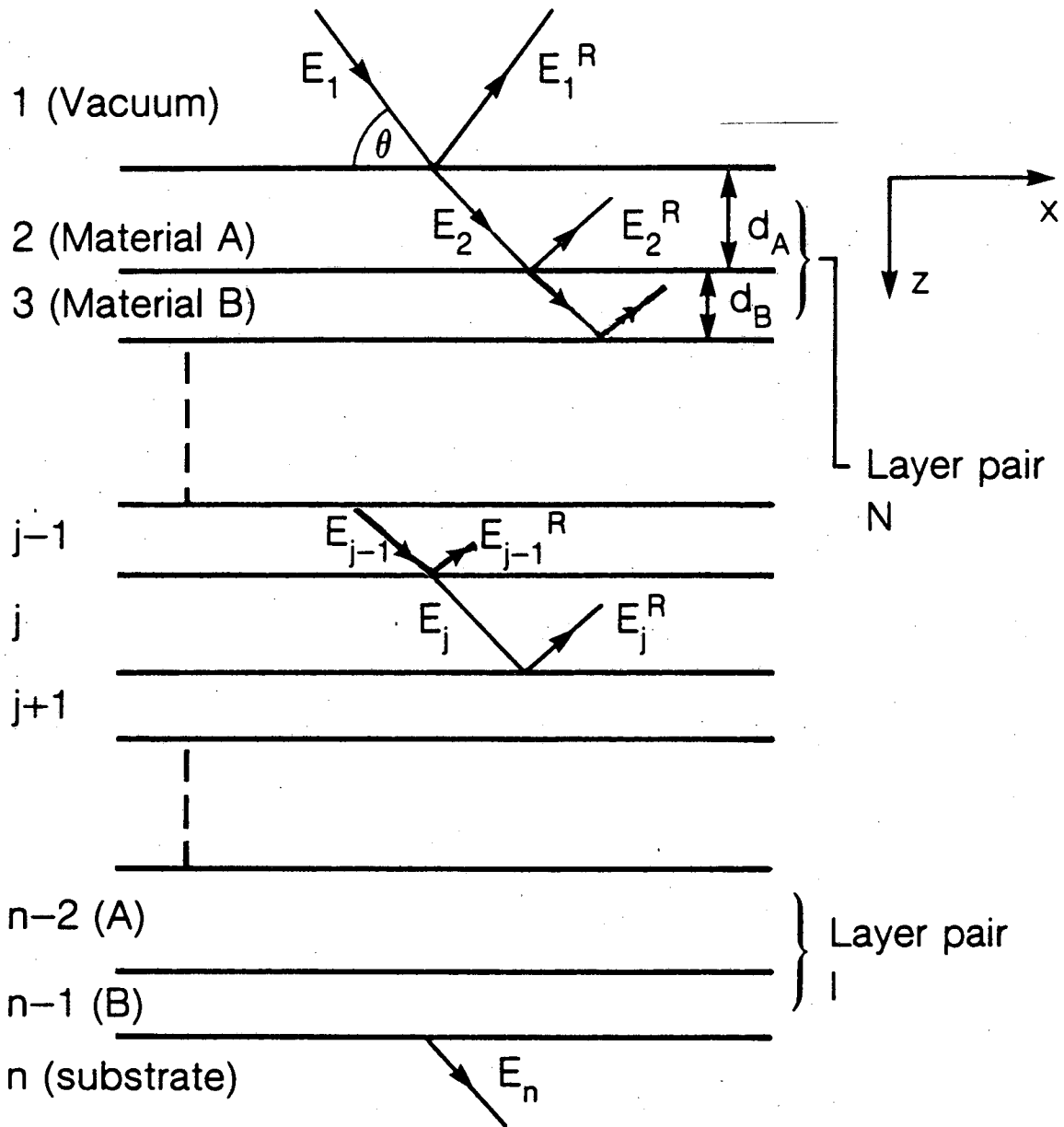
Application of these multilayer coatings requires a good understanding of their reflecting properties. Various methods have been developed to calculate the reflectivity as a function of angle of incidence. Since the multilayer structure can be regarded as either a synthetic crystal with large lattice spacings or an optical interference filter with a very small period, these methods can be divided into two categories accordingly: one uses atomic scattering factors and crystal diffraction theory, the other uses the standard optical multilayer methods. We have developed an efficient method based on the second approach which enabled us to obtain excellent agreement between the calculated and measured reflectivities. Fig. 4.6 shows one such comparison. With this multilayer model, we can design the multilayer so optimum performance can be expected for a particular application.

As can be seen from Fig. 4.6, the Bragg reflection angle (at ~ 2.2 degrees) is several times the value of the total external reflection angle (~ 0.7 degrees). The peak reflectivity is close to 70% with a relatively wide bandpass of 10% (FWHM). These are the unique properties of multilayer coatings that are exploited in the focusing system.

4.5.2 Design and fabrication

For the current application, we usually require the multilayer to have a certain Bragg angle in a given focusing geometry at a given x-ray energy. We also would like to maximize the integrated reflectivity. Using the theoretical model mentioned in the last section, the parameters of the multilayer (d_A , d_B and the total number of periods) which give the optimal performance can be found.

The physics and design of a multilayer coating for x-ray wavelength region is rather straight forward, but it is probably worth mentioning the difficulty of making a good quality multilayer for x-ray applications. As mentioned in the last section,



XBL 8510-11727

Figure 4.5: Schematic drawing of the cross section of an ideal multilayer reflector for x-rays. The abrupt interface in the sketch is an idealization. In reality, the interdiffusion at the interface often can not be neglected in calculating the multilayer reflectivities.

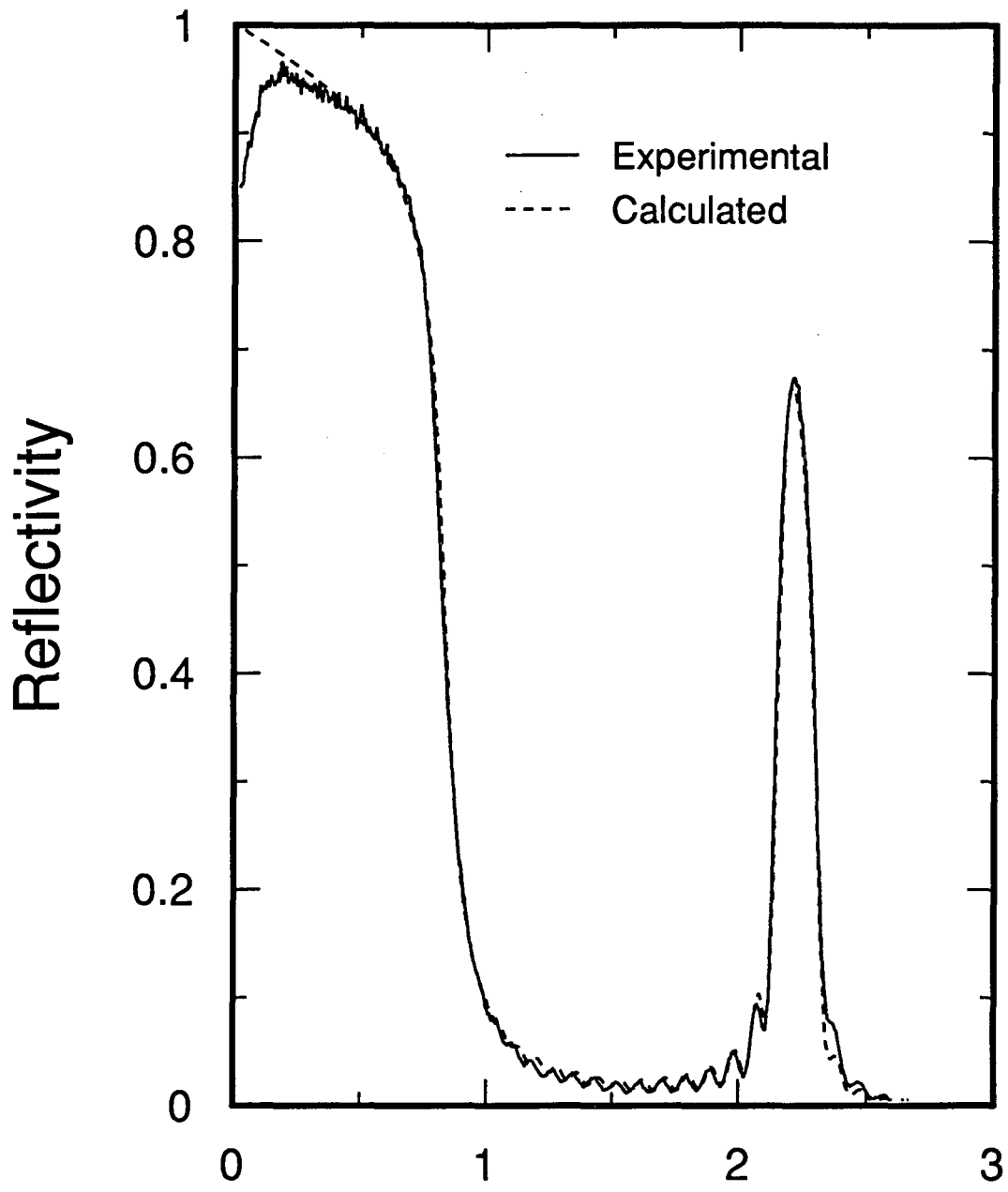


Figure 4.6: Reflectivity versus glancing angle (2θ) for a tungsten-carbon multilayer mirror for Cu $K\alpha$ x-rays. Notice the excellent agreement between the experimentally measured values and the calculated ones. A graded interface is necessary to get such good agreement. Similar multilayers were used in the focusing system described in this chapter.

the period of multilayer coatings for x-ray applications must be very small, so are the thicknesses of individual layers. In a lot of cases, the individual layer contains only a few atomic layers. This made its fabrication difficult in at least two aspects. One is how to control the thickness, the other is how to ensure that the structure is stable over a long period of time. Furthermore, since the reflectivity at each individual interface is low because the difference between the indices of refraction in different materials is small, a large number of periods is necessary to have a sizable reflectivity. In addition, there is also the problem of surface quality of the substrate. In order to make the multilayer structures useful or even meaningful, the surface smoothness must be substantially better than the individual layer thicknesses. All of these factors contributed to the early failures in making useful multilayers for x-rays.

The more recent success in the making of the multilayers came about as a result of significant advances in the electronic industry. Highly stable power supplies, more accurate thickness measurement techniques and availability of large quantities of good optical surfaces (*i.e.* Si wafers) all contributed.

The multilayer coatings used in the experiment described here were made using a sputtering technique similar to that described in [38]. The substrate rotates on a table above two magnetron sputtering sources each containing one of the material being deposited. The power source to the sputtering gun is regulated so a constant sputtering rate is assured. The combination of power settings and the speed of rotation determine the individual layer thicknesses and the number of rotation give the number of period of the multilayer.

In a typical run, the sputtering rates for both materials are calibrated as a function of power setting and speed of rotation. The result of calibration is used to determine the settings necessary to produce an optimal multilayer from the parameters derived from theoretical calculations. In the actual fabrication process, extra steps are taken to ensure both a correct Bragg angle and optimum reflectivity.

We make several multilayers on different substrates (Si wafers) with slightly different combinations of power settings and speed of rotation, then choose the one that shows the best agreement with the desired Bragg angle and with the highest integral reflectivity. The actual mirror is subsequently coated under identical conditions.

4.6 The design and operation of the K-B focusing system

The optical design of a Kirkpatrick-Baez system using multilayer coated mirrors is similar to a corresponding design using total external reflection mirrors. To achieve a focused image, the Coddington equation (4.2) for the tangential rays has to be satisfied by both mirrors. If we label the mirrors as 1 and 2 in the order of beam direction, we have

$$\frac{1}{u_1} + \frac{1}{v_1} = \frac{1}{f_1}; \quad \frac{1}{u_2} + \frac{1}{v_2} = \frac{1}{f_2}. \quad (4.6)$$

If the separation between the two mirrors is s , then $u_2 = u_1 + s$ and $v_2 = v_1 - s$.

In the actual design, we fix the total distance between the source and image $D = u_1 + v_1$, assume a suitable separation s , and specify the demagnification desired for the first mirror to be M_1 , then the rest of the parameters can be calculated from the above equations. Some of them are:

$$v_1 = \frac{D}{M_1 + 1}, \quad (4.7)$$

$$f_1 = \frac{M_1}{(M_1 + 1)^2} D, \quad (4.8)$$

$$f_2 = \frac{(M_1 v_1 + s)(v_1 - s)}{M_1 v_1^2}. \quad (4.9)$$

From these, the glancing incidence angles, θ_1 and θ_2 , and the radii of curvature, R_1 and R_2 , can be decided. The Bragg equation (4.5) can be used to calculate the approximate multilayer periodicity d . It should be remembered that only multilayer coatings with periodicity greater than a certain value can be made reliably and with good reflectivity; unrealistic parameters should be avoided. The space requirements

Table 4.1: Optical parameters for the focusing system

	11.5 keV		16 keV	
	M1	M2	M1	M2
Radius of curvature (m)	15	15	15	15
Diameter of mirror (cm)	2.0	2.0	2.0	2.0
Source to mirror distance (m)	17.14	17.15	21.88	21.89
Image to mirror distance (cm)	16.09	13.8	11.54	9.86
Demagnification, M_1	106.5	124.3	189.6	222.0
Focal length (cm)	15.95	13.69	11.48	9.82
Angle of incidence (deg)	1.22	1.05	0.88	0.75
Multilayer d-spacing (Å)	25.3	29.5	25.3	29.5
Mirror separation (cm)	2.29		1.68	

should also be kept in mind which may limit the range of the demagnification that can be used. The parameters of the focusing system used in the high pressure experiments described in a later section are given in Table 4.1.

The above design procedure is for a fixed x-ray energy. If s is a variable, the designed system can also be made to work at a different energy with a slightly different magnification. This is demonstrated in Table 4.1 as well. The original system was designed to work at 11.5 keV, but it also can work at 16 keV. The only difficulty in this case has been the requirement of a too close separation, which is not strictly met.

In the experiment, the incidence angles of the two mirrors and the positions of the two mirrors along the beam direction can be tuned by either remote control or by a computer controlled stepping motor device. The entire system can also be moved in the two directions perpendicular to the x-ray beam so it can be easily positioned at the central part of the beam.

The alignment of the focusing system is accomplished in the following manner. Firstly, the system is aligned parallel to the x-ray beam. With both mirrors in position and lying flat, the entire system is moved across the x-ray beam when the beam is on, until the hottest part of the beam is located. With a tightly collimated

beam ($100\ \mu\text{m}$ or less on a side) shining into the focusing system, using a detector with a wide open active area and blocking the straight through beam, the correct incidence angle of each mirror is found by continuously rotating the mirror. As the correct angle is approached, the reflection signal can be observed. This procedure is carried out for both of the mirrors. Once the correct incidence angle is found, the actual focusing is achieved by measuring the beam size as each of the mirrors is moved along the beam direction.

4.7 The performance of the x-ray focusing system

The focused beam is characterized in terms of its size, angular divergence, and intensity. We measured the size of the focused beam by scanning a knife edge across the beam. The derivative of the transmitted intensity with respect to the position gives an upper limit to the actual beam size. The best focus is found by the method described earlier. In the high pressure experiment described in the next section, no attempt has been made in finding the best focus along the beam since our objective there was not to achieve the smallest beam size because the synchrotron source size at SSRL beamline VI is relatively large. A beam size of 20 by $10\ \mu\text{m}$ was obtained when focusing mirrors in both directions are used. During other testing experiments performed at the National Synchrotron Light Source (NSLS) at Brookhaven National Laboratory, where the source size is smaller, we have obtained much smaller beam sizes which were limited by the spherical aberrations. In a feasibility experiment where each mirror was only coated in a narrow striped area to reduce the spherical aberration, a beam size of $2 \times 1.8\ \mu\text{m}$ has been obtained. It is clear, beam sizes much smaller than $10\ \mu\text{m}$ in diameter can be obtained with little modification to the current system, provided a suitable synchrotron source is available.

The angular divergence of the focused beam can be easily controlled by using

the aperture up-stream of the mirror. In the present experiment, the multilayer coatings have a constant lattice spacing across the mirror surface. Because of this, at the edges of the mirror, the reflectivity is greatly reduced due to the change in the incidence angle. The maximum acceptance of the mirror system is not determined by the size of the mirror but rather by the areas that are actually reflecting. We have estimated that this results in a maximum effective acceptance(FWHM) of 100 microns. Since the sample is located 10 centimeters away, the angular divergence should be less than 1 mrad. This is verified by the fact that in some cases, very narrow diffraction lines are observed.

The intensity of the focused beam is of primary importance for small samples because the diffracted intensity is proportional to the sample volume. In this regard, we have compared the intensity of the focused beam with the intensity that can be obtained by using slits. We have measured a gain between 4 to 5 in each direction. This agrees well with our discussion in the early sections taking into account that the multilayer coating has probably an average reflectivity around 40%. The gain in the horizontal direction can be increased further by employing multilayer coatings with graded d spacings to increase the effective acceptance since we have no requirements on the angular divergence. We estimate an additional factor of three should be possible with the present mirrors.

4.8 Applications to diffraction studies under high pressure

Despite the gain offered by the focusing device, the intensity in the beam is still not sufficient if only synchrotron radiation from a existing bending magnet beamline is used. To carry out the ADXD studies under very high pressure, one requires the most bright synchrotron sources available and beyond. The wiggler beamline VI at SSRL is one of such sources available at present. We had only a single opportunity to carry out the following experiment.

Fig. 4.7 is a schematic diagram of the experimental setup employed in the present study. The monochromatic radiation from a Si(111) double crystal monochromator is focused and sent into a diamond anvil cell where the sample is located. The diffraction patterns are recorded on a camera using film or on an imaging plate.

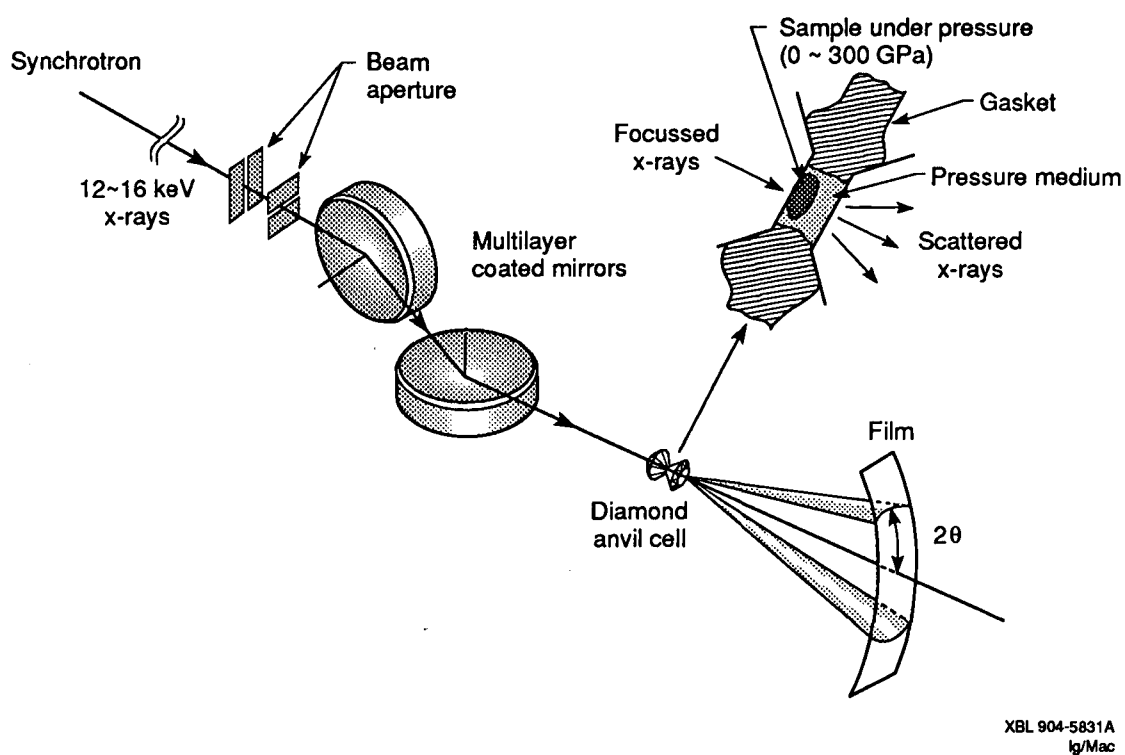


Figure 4.7: A schematic drawing of the setup for the ADXD experiment using the K-B focusing system. The monochromatic radiation produced by a wiggler through the use of a Si(111) double crystal monochromator is collimated by a pair of coarse slits and focused by the multilayer coated mirrors to a small size on the order of $10 \mu\text{m}$ on a side. The diamond anvil cell containing samples subject to high pressure is placed at the focal spot. The diffraction patterns are recorded on either a film fitted to a cylindrical camera or on a flat imaging plate.

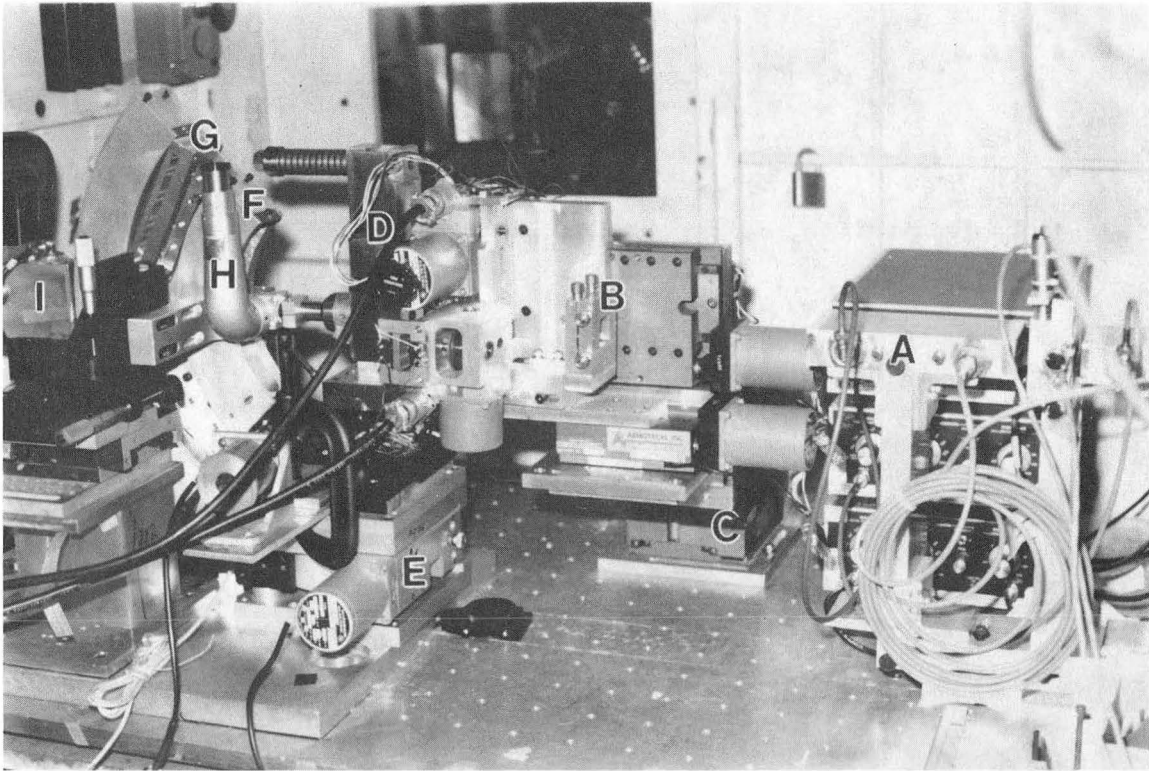
Figure 4.8 shows two pictures of the actual experimental setup. A and I are two ion chambers that are used in the alignment procedures. B is a pair of slits in

both the horizontal and vertical directions. C is the focusing system. Four stepping motors can be seen, the incidence angles and the position along the beam can be adjusted with them. D is the diamond anvil cell. E is a pair of translation stages for the sample alignment. F is the homemade cassette for x-ray films and G is the holder for imaging plates. The microscope H is an alignment aid and a fixed reference point just as described in the EDXD setup in the last chapter.

4.8.1 Ultra high pressure studies

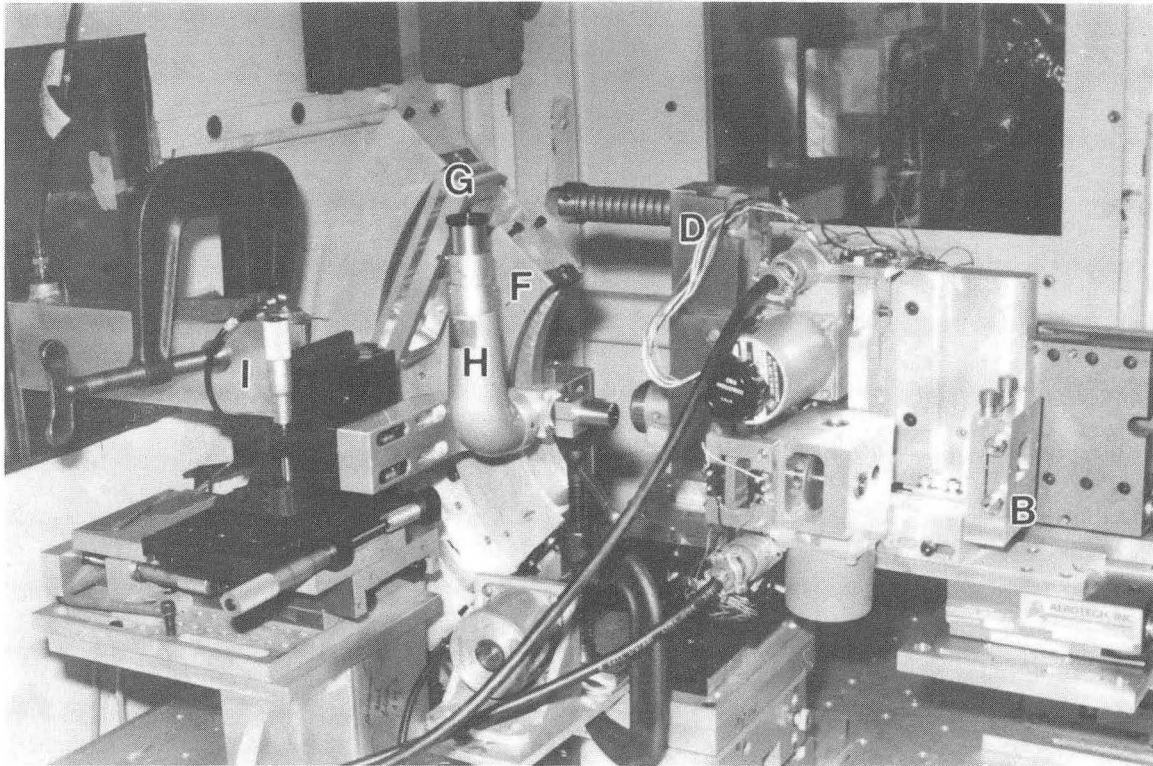
The main objective of the present experiment is to verify whether it is possible to perform angular dispersive diffraction experiments on materials under ultra high pressures with existing synchrotron sources. Fig. 4.9 shows a diffraction pattern of iron in its hcp phase at a pressure close to 300 GPa and at room temperature. The study of iron is particularly important to geophysics because it is believed that iron constitutes the main element in the Earth's core. At these ultra high pressures, the thickness of the samples is probably only 1 μm or less, therefore the diffracted intensity is extremely low. In fact, as one can see from the figure, the inelastically scattered radiation from the diamond anvils has higher intensity than the diffracted intensities. Because of this, a detector with high sensitivity and large dynamic range is necessary in order to be able to observe the diffraction lines. The figure shown is produced by exposing an imaging plate for one hour in the beam. From the digital image, the (100) and (101) peaks can be identified. Figure 4.9(b) also shows a diffraction profile obtained by summing along the diffraction ring which shows the signal to background intensity ratio more clearly.

At the time when the experiment was performed, the magnetic field of the wiggler was much lower than the nominal operating field and the electron beam current was half of its normal value which resulted in a 90% reduction in intensity. If the brightness of the source is increased 10 times by going to higher field and full current, the exposure time would be reduced to 6 minutes which is rather reasonable for this



XBB 906-4571

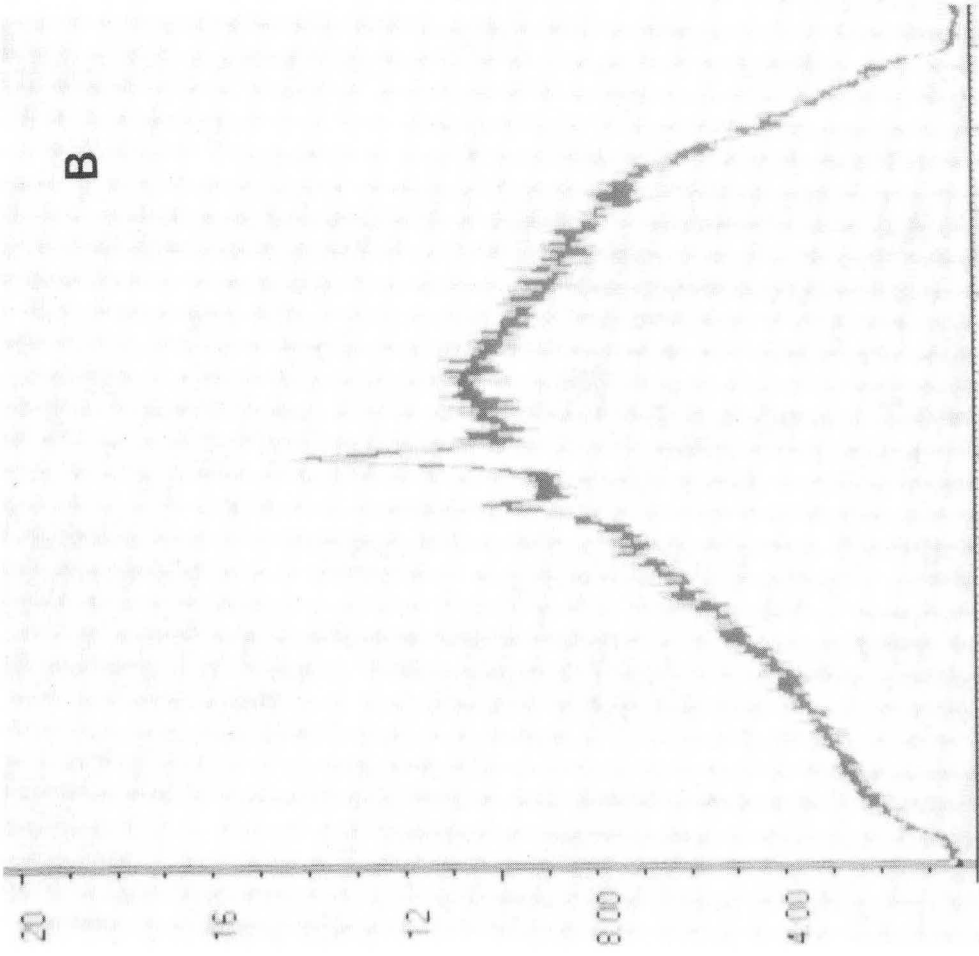
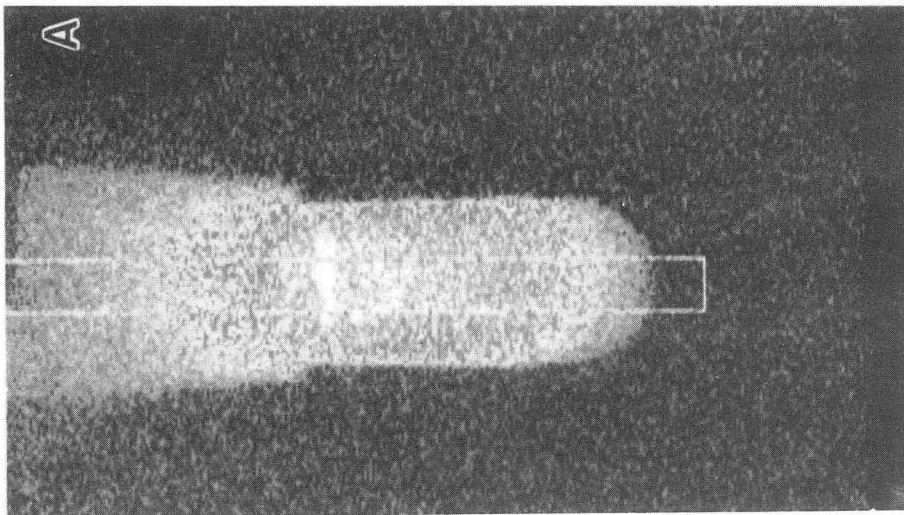
Figure 4.8(a)



XBB 906-4569

Figure 4.8(b)

Figure 4.8: Two pictures of the experimental setup in the ADXD experiments. (b) is a close up. A and I are two ion chambers that are used in the alignment procedures. B is a pair of slits in both the horizontal and vertical directions. C is the focusing system. Four stepping motors can be seen, the incidence angles and the position along the beam can be adjusted with them. D is the diamond anvil cell. E is a pair of translation stages for the sample alignment. F is the homemade cassette for x-ray films and G is the holder for imaging plates. The microscope H is an alignment aid and a fixed reference point just as described in the EDXD setup in the last chapter.



CBB 909-7125

Figure 4.9

Figure 4.9: A diffraction pattern of Fe under ultra high pressure recorded on an imaging plate. (a) The two dimensional pattern shows the sample diffraction rings and the high background that arises from inelastic scattering from the diamond. The shape of the scattering is a result of a slot that was cut on the cylinder in which one of the diamond anvils is supported. The two visible diffraction rings correspond to the (100) and (101) lines of hcp Fe. (b) A summation of line traces of the diffraction pattern shows clearly the peak-to-background ratio in these types of experiments. A detector with large dynamic range is necessary.

type of experiment.

The combination of a state of the art synchrotron radiation, the focusing device, and a high sensitivity detector system like the imaging plate system makes it possible to carry out ADXD studies on samples containing relatively heavy elements to ultra high pressures. If the resolution of the focusing device is improved without the loss of intensity in the future, it might be possible to perform experiments to even higher pressures if it can be generated. The higher resolution will also help to reduce the pressure gradient effects in high pressure structural studies in general.

Challenges still lie ahead for performing ultra high pressure experiments on very light elements like hydrogen. The intensity in the powder diffraction pattern of hydrogen is expected to be 26^2 times smaller than that of Fe. The third generation synchrotron radiation Advanced Photon Source (APS) now under construction at Argonne National Laboratory will certainly provide such an increase in brightness, therefore exciting opportunities for ultra high pressure crystal structural studies are not too far away.

4.8.2 High resolution studies

A separate type of experiment involves the use of higher resolution offered by the angular dispersive geometry. We have studied the onset of a phase transition in CsI to illustrate this aspect. The details of the study are presented in the next chapter. For the sake of being self contained, we mention the essence of the results.

CsI is a typical ionic solid. Under high pressure, it transforms continuously through an orthorhombic structure to an hcp like structure at ultra high pressures. The actual onset of the transition has been difficult to ascertain because of the relatively low resolution of other methods. Our current setup offers a unique opportunity in this regard. The onset of the phase transformation has been based on the broadening of the diffraction peaks. However, a pressure gradient in the sample can also introduce the observed broadening. In order to exclude this possibility, we

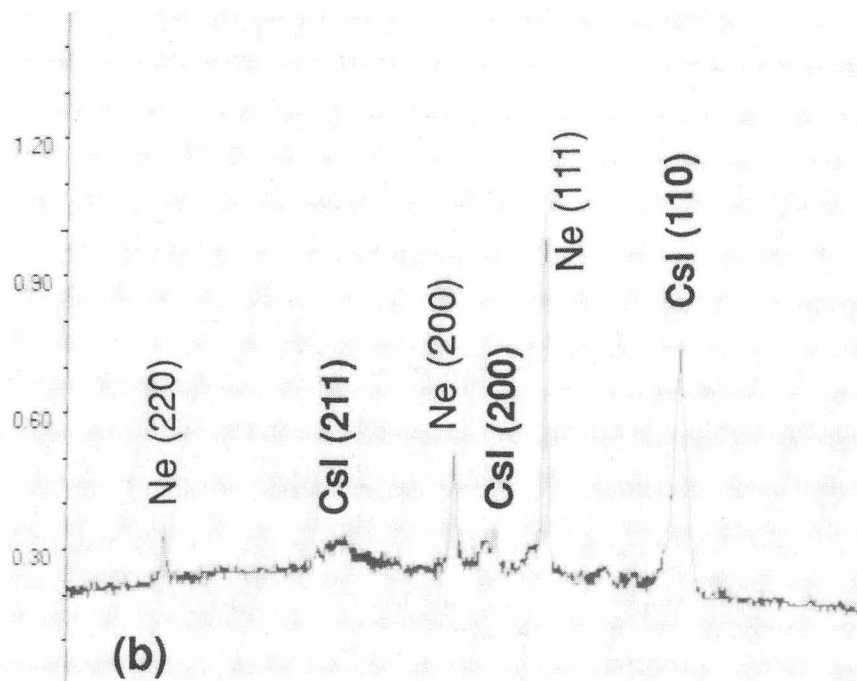
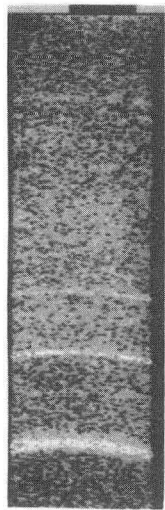
have used neon as a pressure medium in our experiment. Since Ne is softer than CsI, the line broadening will be more severe for Ne than for CsI if the broadening is caused by the pressure medium. At the same time, we should observe the line broadening in CsI at a much earlier stage compared to using the EDXD method if the broadening is due to an actual phase transition rather than non-hydrostatic stress.

Figure 4.10 shows a diffraction pattern of CsI and Ne under a pressure of about 26 GPa recorded on an imaging plate. Two conclusions can be drawn from this pattern. The diffraction lines from Ne are significantly sharper than that from CsI, which clearly indicates that the broadening seen in CsI is not due to the pressure gradient. A careful study of the diffraction patterns of CsI as a function of pressure indicates the line broadening is much less than has been observed in previous experiments that employed other methods. This observation, along with the single crystal experiment data using He as pressure medium by other people has led us to conclude that the onset of the phase transition is closely related to the non-hydrostatic stress in the pressure environment. This observation can explain the apparent discrepancies among the various data sets from pervious studies.

The higher resolution of the ADXD method will be very useful in the studies of materials that have complex crystal structures. The use of the ADXD method also offers the possibility of doing anomalous scattering experiments. This technique is very useful in the identification of structures of crystals that contain atoms with similar scattering factors. For example, it would be possible to study the ordering of Cs and I ions in CsI.

4.8.3 Effect of beam size on the quality of diffraction patterns

The size of the beam clearly affects the quality of the diffraction pattern. The current setup also provides unique opportunities in studying these effects. With the



CBB 909-8047

Figure 4.10

Figure 4.10: A high resolution diffraction pattern of CsI under a quasi-hydrostatic pressure of approximately of 26 GPa. It is clear that the width of the diffraction peaks from CsI is much wider than that from Ne, so this widening is not due to the pressure gradient that existed. The higher resolution afforded by the current system is very useful in these circumstances.

current setup, the beam size can be changed by using two dimensional focusing, one dimensional focusing, or no focusing at all. The two dimensional nature of the detector system also aided greatly in seeing the changes in the diffraction patterns.

Figure 4.11 shows two diffraction patterns of CsI under very similar pressures except the beam size used in (A) is $20 \times 10 \mu\text{m}$ (the focused beam) and (B) $80 \times 60 \mu\text{m}$ (unfocused). A normal sample preparation procedure was carried out on CsI before the sample was loaded. It is obvious that the grain size does not affect the quality of the diffraction pattern much if the incident beam is large. For a small incident beam size, the pattern becomes very spotty. This has important implications for the EDXD studies. Since in most cases a very small beam size is used, the intensity data from an EDXD experiment may not be very reliable.

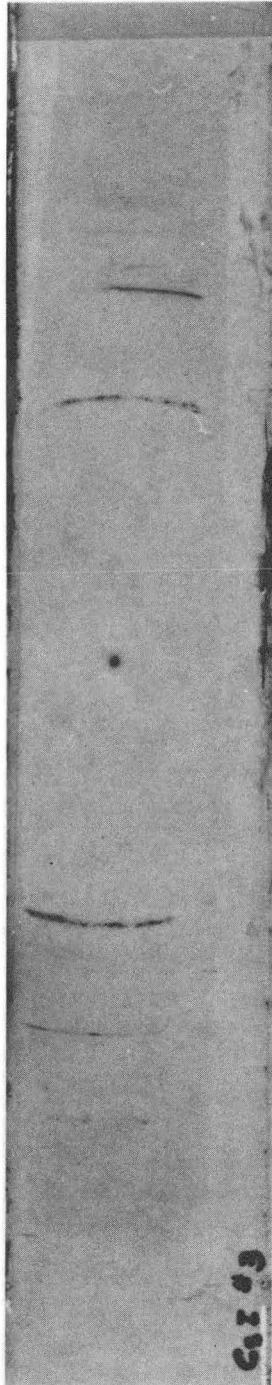
4.9 Conclusions and suggestions for further studies

In order to make an x-ray focusing system useful in studies of structure of materials under high pressure, both the beam size and photon flux are of primary importance. The current experiment demonstrated that by using the Kirkpatrick-Baez system with multilayer coated spherical mirrors, there is sufficient photon flux in the focused beam for performing experiments on a wiggler beamline like SSRL's beamline VI.

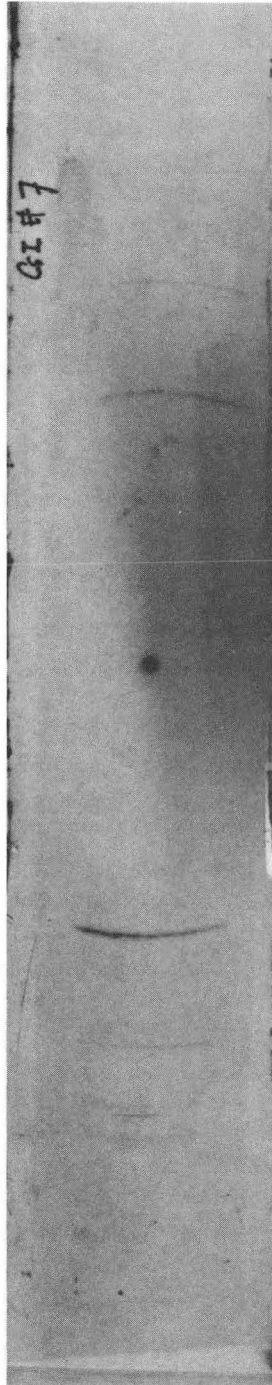
Further improvements on the beam size must maintain the same level of total photon flux. Therefore, aspherical mirrors are necessary. On the other hand, with the development of the newer, brighter synchrotron radiation sources, the relatively economical spherical mirror focusing system may be used with a reduced aperture to get a source size limited focal spot with sufficient intensity for diffraction experiments at ultra high pressures.

The gain in photon flux can be improved by increasing the acceptance in the horizontal direction by the use of a large aspherical mirror coated with a graded multilayer. In the vertical direction, a similar increase does not seem to be appro-

(a)



(b)



XBB 906-4574

Figure 4.11

Figure 4.11: The effect of beam size on the quality of diffraction patterns. (a) A diffraction pattern taken with a micro beam with dimensions $20 \times 10 \mu\text{m}$; (b) A diffraction pattern taken with a beam with a relatively larger size: $80 \times 80 \mu\text{m}$. Comparison of the two shows the quality of the diffraction pattern is affected very much by the beam size change of this order of magnitude.

priate for high resolution experiments, but is also possible when the resolution can be traded for higher photon flux.

Chapter 5

O. the Structure and Equation of State of CsI under High Pressure

This chapter describes a series of experiments on the structure of CsI under high pressure. The presentation is organized as follows. After a brief introduction of the motivation for this study, a review of previous studies is presented. The experimental procedures that are pertinent to the present studies are then described, followed by a detailed presentation of our results from various runs. The results are then used to reconcile some discrepancies among the previous static compression studies and to compare the quality of some existing analytical equations of state formulations. The new equation of state derived from the present studies is then used to derive a metalization pressure for CsI using the simple Herzfeld model. The equation of state data are then compared with previous theoretical and dynamic compression studies. Finally, we present a simple ionic model which has enabled us to explain successfully the experimental results.

5.1 Introduction

Ionic solids are one of the most important classes of simple solids. Their various properties under ambient conditions can often be described by very simple physical models. This simplicity arises from the fact that the electronic configurations of all

ions in the crystal correspond to closed electronic shells, as in the inert gas atoms. The charge distribution on all ions is largely spherical symmetric and the overlap of charges between adjacent ions is very small. So at ambient conditions, all of them are electronic insulators. The application of pressure changes the situation rather dramatically. As the pressure is increased, the overlap of charges also increases. One of the most striking phenomena is that upon sufficient compression, all of them exhibit metallic behavior. The entire sequence of structural and electronic properties therefore serves as an excellent testbed for various theoretical models.

The simplest of all ionic solids are the alkali halides. Of the twenty commonly seen ones (combinations of Li, Na, K, Rb, Cs and F, Cl, Br, I) and under ambient conditions, all except three crystalize in the B1 (NaCl) structure, in which the cations and anions sit on two interpenetrating fcc lattices. Each ion has six nearest neighbors of the unlike ions. Three Cs compounds (CsCl, CsBr, CsI), however, crystalize in the B2 (CsCl) structure where each ion is surrounded by eight unlike ions. The difference here arises probably because of the change in the extent of charge transfer, although it has been proposed that non-classical origin might be important in determining the relative stability between the two phases[40]. In any case, most of the compounds that crystalize in the B1 phase will transform into the B2 structure under pressure. For those involving heavier ions, the transformation occurs at rather low pressures. Therefore, it is probably justifiable to consider the B2 structure as a common rather than exceptional structure of alkali halides under pressure. Therefore the possible further transformation of the B2 structure may reflect a general trend in the phase transition sequence.

For a given pressure, the compression achieved depends on the compressibility of the material. Table 5.1 lists the bulk moduli of the alkali halides. It can be seen that the bulk modulus is a monotonic function of both the anion and cation atomic numbers. The three cesium compounds do not obey this trend because they have different crystal structures than the rest as discussed above. If same structure can

Table 5.1: Bulk Moduli (in GPa) for Alkali Halides*

	Li	Na	K	Rb	Cs
F	67.1	46.5	30.5	26.2	
Cl	29.8	24.0	17.4	15.6	18.2
Br	23.8	19.9	14.8	13.0	15.8
I	17.1	15.1	11.7	10.6	11.5

* from [41] and [42].

be maintained, it is likely that such trend will be strictly obeyed. It is seen that CsI is the most compressible among them and for a given pressure, greatest compression can be achieved. For this reason, CsI has been the subject of rather extensive study in the last few years. A summary of previous studies will be presented in the next section.

The study of CsI is interesting in a different context as well. With the recent progress in generating ultra-high pressures, one can study materials under such a compression that the most important contribution to the total crystal energy is from the repulsive interaction due to charge overlapping. This implies that isoelectronic compounds should exhibit similar structures and equations of state in this pressure range. CsI, together with Xe and BaTe offers an interesting sequence for this comparison. The rare gas solid Xe has recently been shown[43] to go through two phase transitions under very high pressure. For pressures greater than 75 GPa, it has the hcp structure and no further phase transition was observed to the highest pressure of 170 GPa, which exceeds the metallization pressure of 150[44] (130[45]) GPa. BaTe, on the other hand, has been shown to transform from the room pressure B1 structure to the B2 structure at a pressure of 4.8 GPa and to remain in the B2 structure until at least 40 GPa, the highest pressure studied, with metallization[46] occurring at a pressure of 25 GPa. It seems that the structural phase transition is not directly linked with the metallization transition in these two compounds and no volume discontinuity has been detected at the insulator-metal transition. CsI can

serve as a further test on this observation.

5.2 Previous studies on properties of CsI under high pressure

Previous studies on the properties of CsI under high pressure can be divided into four categories: structural and equation of state studies under static compressions, equation of state studies by shock wave methods, spectroscopic studies on the optical properties, and theoretical calculations on both the electronic and structural properties. We would like to briefly review the results obtained from these studies in this section.

Static equation of state studies under relatively low pressures were carried out as early as in the 1940's by P. W. Bridgman[47, 48] using a piston-cylinder assembly as the means of obtaining high pressures. A similar study was carried out by Vaidya *et al.*[49] in 1971. Because of the limited maximum pressure that could be reached, it was not possible to observe any change in either the structural or other properties. Hammond *et al.*[50, 51] was probably the first one who used the diamond anvil cell technique to study the equation of state of CsI. In that study, they observed no phase transition upto the maximum pressure of 23 GPa. The major advancement of diamond anvil cell technique in the 70's has changed the situation dramatically. Because of the high pressure that is achievable by such an apparatus, the insulator to metal phase transition seems to be in the range of experimentation. A large effort has been devoted to study the various properties of CsI under relatively high pressures.

Static studies on the structure of CsI under moderately high pressures have been reported by Asaumi[52], Knittle and Jeanloz[53, 54], Huang and Ruoff[55, 56, 57], and Zisman *et al.*[58, 59] to about 60 GPa. Results from the first three groups all indicated that the B2(CsCl) structure of CsI under ambient conditions underwent a tetragonal distortion between 35 ~ 40 GPa based on the broadening and then

splitting of one or more diffraction lines. Asaumi also reported a further distortion at 56 ± 1 GPa where the tetragonal cell transformed into an orthorhombic cell. Later studies by Vohra *et al.*[60, 61] to much higher pressure (95 GPa) identified the same transition sequence. The equation of state derived from all these studies are in rather good mutual agreement except for certain pressure ranges in the study by Zisman *et al.* Since the structure at the highest pressure is orthorhombic, it is unclear whether CsI will transform into a close packed, more symmetric structure at even higher pressures.

Zisman *et al.* used Xe as the pressure medium in their study and assumed the structure of Xe remained in the fcc structure throughout the pressure range. They concluded that the equation of state of Xe and CsI overlap each other exactly for pressures above 15 GPa. Since then, new data on Xenon have become available[43], solid Xe in fact goes into an unidentified phase for pressures above 14 GPa. So it is possible that the equation of state of Xe derived from their study is in error for high pressures. The conclusion that the equations of state of Xe and CsI overlap each other exactly above 15 GPa may therefore be untrue. Because of the experimental limitations, only one of the diffraction peaks of CsI in the cubic phase can be observed at high pressures and accordingly, only the first two diffraction peaks can be observed after the phase transition. This led them to adopt the same structure for the high pressure phase of CsI as in other studies. The pressure volume data between 5 and 40 GPa are in agreement with other static compression studies. Below 5 GPa, CsI seems to be more compressible than in other diamond anvil cell studies. And above 40 GPa, their data appear to be significantly more compressible as well. Some deviations from the previous lower pressure studies can be observed, but they were not substantiated in those studies.

CsI has also been studied extensively using the dynamic compression method. In this case, the material is subject to a shock loading, in which the density, pressure, and temperature all increase. A relation among them can then be obtained by

varying the strength of the shock loading. These relations are normally referred as the Hugoniot equation of state. To a good approximation, it can be separated into two parts,

$$P = P(\rho, T) = P_0(\rho, T_0) + P_T(\rho, T)$$

where P_0 refers to the static equation of state at a reference temperature T_0 and P_T is the thermal contribution due to the high temperature T .

By separating P into two parts, one is able to compare the experimentally obtained Hugoniot equation of state data with an isotherm by using various techniques to estimate the thermal pressure $P_T(\rho, T)$.

Early shock wave studies have been reported by Christian[62] in the low pressure range of up to 25 GPa. These data were compared with the static data of Hammond[50] by Bassett and Takahashi[51] and good agreement was found. Al'tshuler *et al.*[63] and Pavlovskii *et al.*[64] shocked CsI to a pressure of 110 GPa and 550 GPa respectively. More recently, Radousky *et al.*[65] measured the temperature of CsI under shock loading. The temperature ranged from 3400 to 10800 K for pressures range from 24 GPa to 92 GPa. They also observed melting of CsI along the shock wave adiabat at a pressure of 25 GPa and a temperature of 3500 K. Subsequent shock wave experiments by Swenson *et al.*[66] confirmed this melting behavior. These measurements also constitutes a mutually consistent data set.

Several theoretical studies on the high pressure properties of CsI have been performed [67, 68, 69, 70]. These studies gave directly the static equation of state and also the electronic properties of the crystal under pressure. From these, the thermal contribution to the equation of state from both the vibrational contribution and electronic contribution can be estimated. One major drawback of these studies is that they rely on the knowledge of the actual crystal structure under the given pressure. So these studies assumed either the zero pressure structure of CsI or the proposed tetragonal distortion. In fact, both a first principle study[69] and a model calculation[60] have confirmed the instability of the B2 structure below

certain compressions.

Spectroscopic observations on CsI has also been performed on CsI under high pressure by many authors. Optical absorption measurements have been reported by Asaumi[71] to 45 GPa, Itieet *al.*[72] and by Makarenko *et al.*[73], and Knittle and Jeanloz[53, 54] to 60, 58, and 65 GPa respectively. From these studies, the extrapolated metallization pressure varied from 65 GPa to 110 GPa. Vohra *et al.*[74] claimed that CsI metalized at a pressure of 65 ± 5 GPa based on absorption and reflectivity data. This claim was quickly rejected by the experiments of Williams and Jeanloz[75], in which they extended the absorption measurements to much lower photon energies and the closure of the gap was not observed to a pressure of 93 GPa. Reichlin *et al.*[76] carried out similar experiments to much higher pressures and concluded the metallization pressure lies in the range of 110 ± 10 GPa. In these measurements, the pressure was determined from the ruby fluorescence technique and therefore is not expected to be affected by the equation of state of CsI itself. Hence, it serves as an additional check on the equation of state if a physical model is used to relate the metallization transition to the volume compression.

There are major inconsistencies among the previous studies concerning the compressional properties of CsI. In fact, The equation of state derived from the static studies overlaps with the Hugoniot equation of state derived from the dynamic compression studies. This requires the thermal contribution to the pressure from both the electronic and vibrational contribution to vanish or cancel out. It is very unlikely because of the extremely high temperature that exists in the dynamic compression studies. On the other hand, the shock wave compression equation of state, after correcting for the thermal contribution to the pressure, is in good agreement with the results of theoretical calculations[68]. In order to explain the discrepancy between the dynamic compression and static compression data, it was proposed that CsI disproportionate into elements Cs and I [77] at the high temperatures of shock wave experiment. This explanation has not been fully accepted by the shock wave com-

munity. Furthermore it has not explained the discrepancy between the static results and theoretical calculations for single phase CsI. An attempt has been made[66] to attribute the discrepancy to errors in static pressure due to stress inhomogeneity, because the apparently higher compressibility reported for static experiments was performed with a rare gas Xe medium[58]. The required differential stress, however, appears to be greater than those permitted by the strength of CsI at high pressure.

5.3 Experimental

The study on the structure of CsI under pressure presented in this thesis included several experimental runs with each one designed for specific purposes.

The first run (PTCSI series) was aimed at obtaining the structural and compressional properties of CsI under ultra high pressures (> 100 GPa). In this case, a powdered mixture of CsI (99.999% purity) and Pt (99.999%) was confined in a $40\ \mu\text{m}$ hole of a T-301 stainless steel gasket that was indented to a pressure of $40\sim 50$ GPa and was loaded into a diamond anvil cell with beveled diamonds. The central flats for the two diamonds were $20\ \mu\text{m}$ and $50\ \mu\text{m}$ in diameter with bevel angles of 5 and 7 degrees respectively. This way, the two diamonds with unequal central flats served the purpose of a double beveled anvil to allow a reduction in stress concentration near the edge of the flat so higher central pressures can be achieved before the anvils fail.

The second run (CI and CSI series) consisted of loading 4 different sample assemblies into two diamond anvil cells. Holes with $75\ \mu\text{m}$ diameter were drilled into the stainless steel gasket. The gaskets were preindented to a pressure of about 30 GPa. The anvils used have $100\ \mu\text{m}$ central flats and are not beveled. The runs were targeted at somewhat lower pressure range but with a larger sample volume. Two of the assemblies consisted of mixture of Pt and CsI powders as in the first run. The third assembly consisted of only CsI powder which is used to obtain diffraction patterns free from diffraction peaks from the Pt pressure standard to

facilitate interpretation of the diffraction patterns. The pressure on this assembly was obtained from the CsI diffraction lines which was in turn calibrated by the data obtained from the previous two assemblies. The fourth assembly was essentially a small single crystal CsI. This is used to study the effect of preferred orientation.

The above two runs were carried out on the National Synchrotron Light Source (NSLS) X7A beamline using the Energy Dispersive X-ray Diffraction (EDXD) method. Because the inherent low resolution of the detector, no effort has been made to minimize the line broadening due to pressure variations. In order to examine the effect of non hydrostatic compression, three more runs were carried out using Angular Dispersive X-ray Diffraction (ADXD) methods. Two of them were performed on the NSLS beamline X3A and the other one at Stanford Synchrotron Radiation Laboratory (SSRL)'s LBL-EXXON wiggler beamline IV-1.

In these three runs, CsI powder was loaded without a pressure medium (ACSI series), with ethanol-methanol(1:4) mixture (ACSIM series), and with Ne gas (ACSINE series) to achieve different levels of hydrostaticity. In all three runs, significantly larger samples ($\sim 300\mu\text{m}$ diameter) and anvils with large flats ($300\mu\text{m} \sim 400\mu\text{m}$) were used. The pressure range was rather limited. In fact, the runs were terminated when large broadening was observed during the loading process. In the first two runs ruby fluorescence was used to calibrate the pressure as described in Chapter 2. During the last run, Ne diffraction served as the primary pressure scale. Occasionally ruby fluorescence was also measured to confirm the Ne pressure scale.

The two EDXD runs were carried out using a $10\mu\text{m} \times 10\mu\text{m}$ x-ray beam, while the two ADXD runs at X3 were carried out using a $140\mu\text{m} \times 140\mu\text{m}$ beam due to insufficient intensity with smaller beams. The runs at SSRL were carried out using several different beamsizes, correspond to focusing in both horizontal and vertical directions; focusing only in the horizontal direction with slit in the vertical direction; and no focusing in either direction. The beamsizes were approximately $20\mu\text{m} \times 10\mu\text{m}$, $20\mu\text{m} \times 60\mu\text{m}$, and $80\mu\text{m} \times 60\mu\text{m}$. These have enabled us to learn the

effect of beamsize on the quality of the diffraction patterns which were discussed in Chapter 3.

5.4 Results

We will present the results in the chronological order: ultra high pressure region first, then the results in the lower pressure region, finally the results from the ADXD studies.

5.4.1 Crystal structure of CsI under ultra high pressures

Due to the small size of the central flat of the diamond anvils, the pressure rises very quickly initially. Therefore, the ultra high pressure run was not aimed at obtaining data points in the lower pressure region. At pressures above 200 GPa, the diffraction patterns of CsI display a triplet of peaks that is similar to the (100), (002), and (101) triplet [43] of hcp Xe above 100 GPa, and is typical of an ideal hcp metal (e.g. high pressure phase of Fe, Re, *etc.*). Figure 5.1 shows a representative diffraction pattern obtained. The two lines correspond to (100) and (101) are easily identified, while (002) usually only shows up through a least square fitting procedure.

The position of the three lines also falls on the extrapolation of the (011), (101), and (110) triplet of the CsI phase above 60 GPa according to the previously assigned orthorhombic structure [52]. However, two other evidences led us to conclude that the hcp¹ structure is the preferred assignment. One of them is the intensity data. Although as pointed out in chapter 3 that the intensity data may not be very reliable if a very small beamsize is used, however, in this run it is expected that crystals are crushed into much smaller sizes, so the intensity data are not going to be distorted much. Table 5.2 shows the measured intensities of the peaks compared with both

¹With two different ions, different orderings results different structures, the true hcp structure only exists if the locations of the ions are disordered on the hcp lattice. However, the current x-ray data is not able to distinguish among this, in fact, all these structures have similar diffraction patterns. We therefore use the phrase hcp and hcp like to refer to all these possible structures.

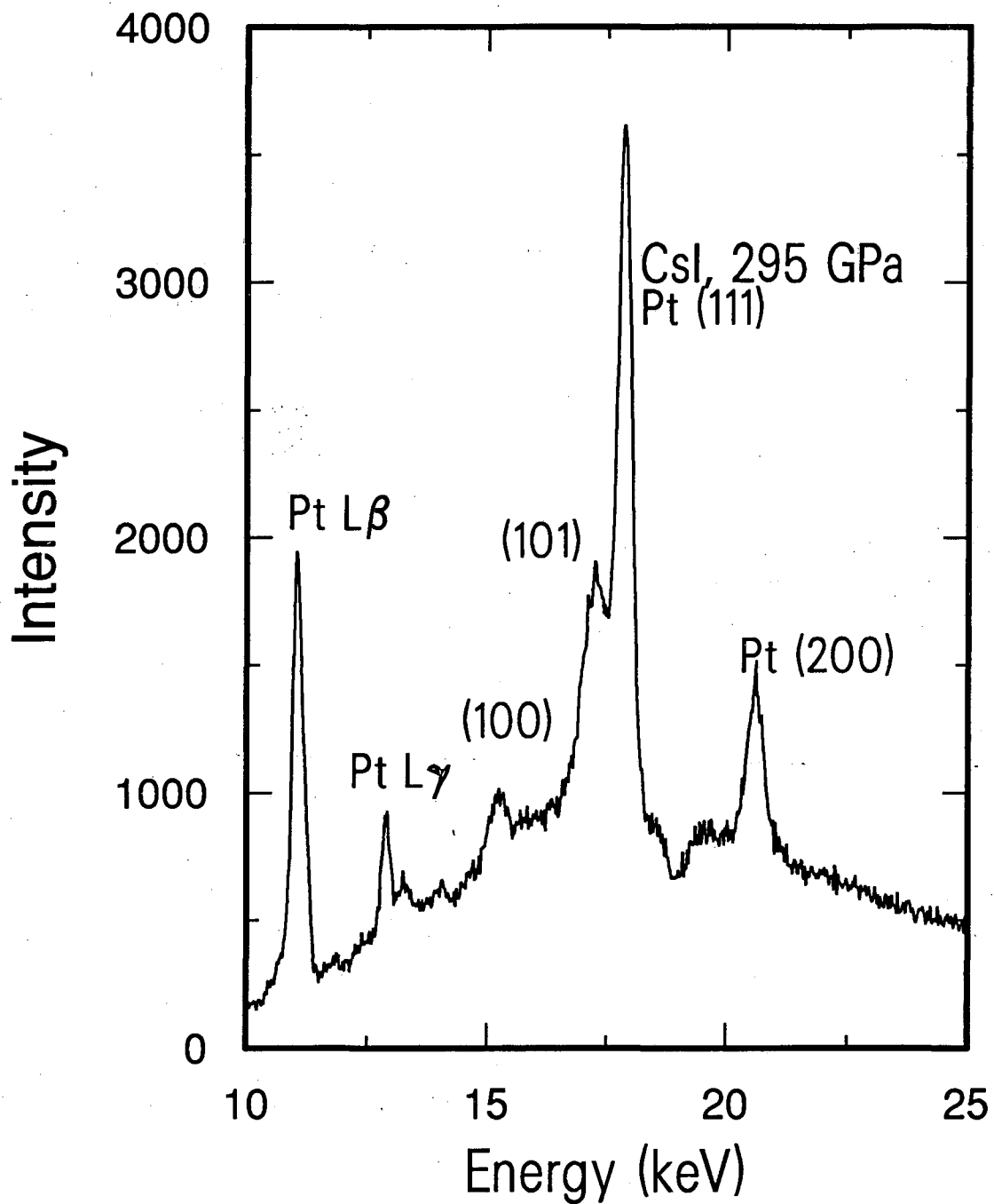


Figure 5.1: An energy dispersive diffraction pattern of CsI under a pressure of 295 GPa. The (100) and (101) lines corresponding to a hcp-like structure are easily identified, the (002) line is excessively broadened and shows up only via a peak fitting procedure. This feature is common in most hcp metals under non-hydrostatic compressions.

Table 5.2: A comparison of the observed diffraction peak intensities with calculated ones based on the ideal hcp structure and orthorhombic structure proposed in previous studies. The strongest diffraction line in each set is assumed to have a relative intensity of 100.

CsI		Ideal hcp		Orthorhombic	
$d_{obs}(\text{\AA})$	I_{obs}	hkl	I	hkl	I
2.375	18	(100)	22	(011)	100
2.239	22	(002)	26	(101)	100
2.094	100	(101)	100	(110)	100

the hcp and orthorhombic assignment. The observed and calculated intensities for the hcp assignment are in agreement while not for the orthorhombic assignment. Second evidence came from the relations of the ratios of the interplanar spacings as a function of pressure. Figure 5.2 shows the pressure dependence of the position of diffraction peaks in the high pressure region. The interplanar spacings of each diffraction peak changed continuously over the pressure range but the ratios of the interplanar spacings remained remarkably constant as evidenced by the lines shown along with the experimental data points. These lines were calculated based on an ideal hcp structure, therefore the ratios between the lines are constant. Such constancy strongly suggests the interplanar spacings are constrained by structural symmetry. The previously assigned orthorhombically distorted structure does not possess these intrinsic constraints.

Table 5.3 present the pressure volume data calculated based on the hcp structure assignment for pressures above 150 GPa and on the cubic structure for low pressures. Due to the rapid rise in pressure, no data are available in the intermediate pressure range.

One might argue that because CsI is an ionic solid, so the charged ions will not form an ideal hcp lattice. This can be explained by the following two arguments. (1) The bare Coulomb interaction is only a small fraction of the repulsive interaction at high pressures, even assuming fully charged ions, so its role is minor. (2) At the

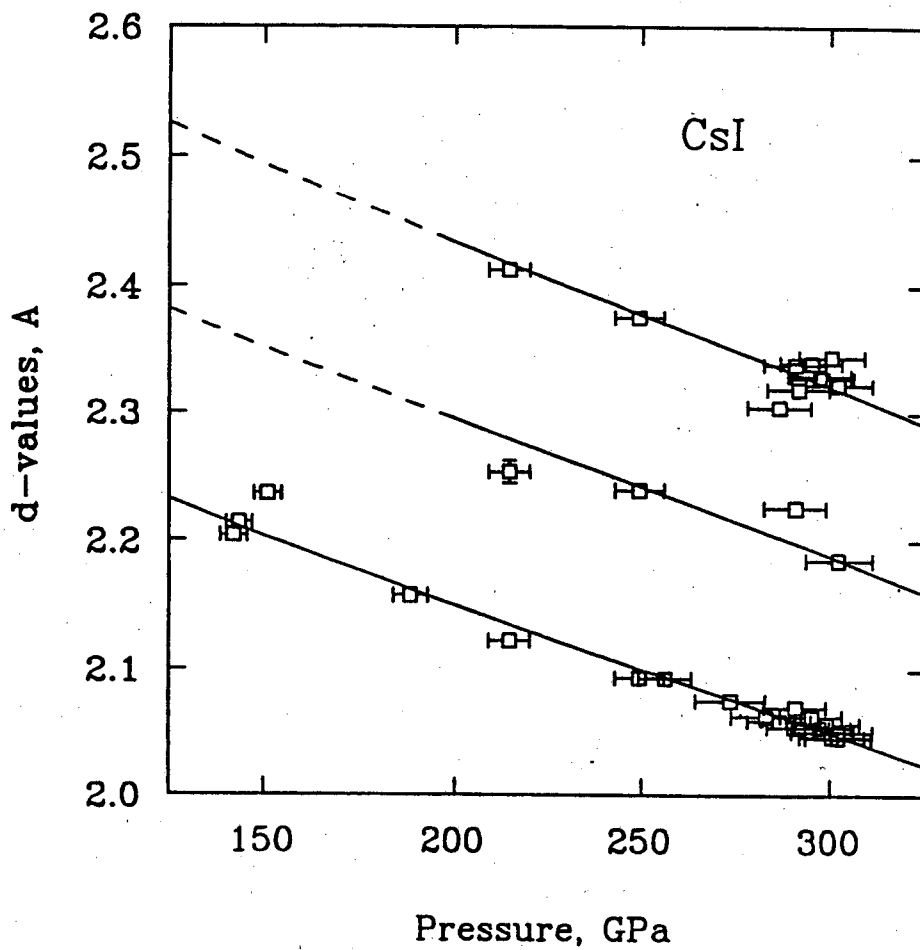


Figure 5.2: The variation of lattice spacings as a function of pressure for CsI in the ultra high pressure range. The straight lines were calculated based on a hcp lattice. The good agreement between the experimental points and the calculated lines supports our structural assignment.

Table 5.3: Volume per atom as a function of pressure of CsI in the PTCSI run. We assumed a B2 structure for pressures below 25 GPa and a hcp structure for pressures above 140 GPa.

Pressure(GPa)	σP	Volume($\text{\AA}^3/\text{atom}$)	σV
7.61	0.32	37.19	0.01
7.62	0.35	37.08	0.03
11.16	0.37	33.94	0.02
12.38	0.37	33.05	0.04
13.56	0.46	32.98	0.03
13.75	0.40	32.61	0.03
14.01	0.41	32.67	0.03
20.26	0.51	30.09	0.11
21.90	0.50	29.68	0.06
24.65	0.54	29.12	0.17
142.15	3.50	16.90	0.09
143.58	3.46	17.13	0.02
151.01	3.48	17.13	0.02
188.16	4.59	15.86	0.01
214.73	5.48	15.12	0.02
249.49	6.56	14.52	0.01
256.31	7.04	14.48	0.04
273.61	9.23	14.11	0.10
282.97	9.12	13.86	0.08
286.48	8.23	13.78	0.02
290.63	8.22	14.08	0.02
291.53	8.19	13.67	0.02
294.93	8.18	13.89	0.01
297.08	8.37	13.73	0.03
297.94	8.33	13.68	0.01
299.14	8.56	13.75	0.04
300.34	8.78	13.81	0.03
302.02	8.89	13.27	0.05
302.17	8.89	13.62	0.02

pressure range of interest, CsI is metallic, so the Coulomb interaction between the ions are greatly reduced by charge transfer and by the screening due to electrons in the conduction band. The resulted distortion is therefore very small. It can not be resolved in the current experiment.

Of course, one would expect that at lower pressures, the effect of the long range Coulomb interaction should manifest itself. This has been the major motivation for carrying out the follow up study in the lower pressure region.

5.4.2 Crystal structures of CsI in the intermediate pressure range

Since the structure of CsI under ultra high pressure (> 200 GPa) is found to be hcp like, it is natural to ask how the phase transition occurs. To this end, we have undertaken two EDXD runs on CsI focused on the lower pressure range. Figure 5.3 shows a selected series of diffraction patterns obtained in this study. At low pressure, the diffraction pattern clearly is consistent with a B2 structure. Due to the similar charge distribution of the Cs^+ and I^- ions, the B2 structure has the same diffraction pattern as a bcc lattice. Two peaks correspond to the (110) and (200) lines within the energy range illustrated can be seen in the diffraction pattern at 12.9 GPa. As the pressure increases, significant broadening can be seen. Above 40 GPa, the peak corresponding to the (110) peak has split into five peaks. The splitting becomes more evident as the pressure is further increased. Figure 5.4 shows the result of a deconvolution on one of these patterns. Five peaks can be clearly identified.

This observation is in direct contrast with previous studies. Clearly, the previously assigned orthorhombic distortion can not explain these observed patterns. This has led us to reexamine the structure identification in this pressure range. Since the structure of CsI under ultra high pressure is hcp as explained in the last section, it is natural to consider structures that is intermediate between B2 and hcp. Indeed, one such structure can successfully explain the diffraction pat-

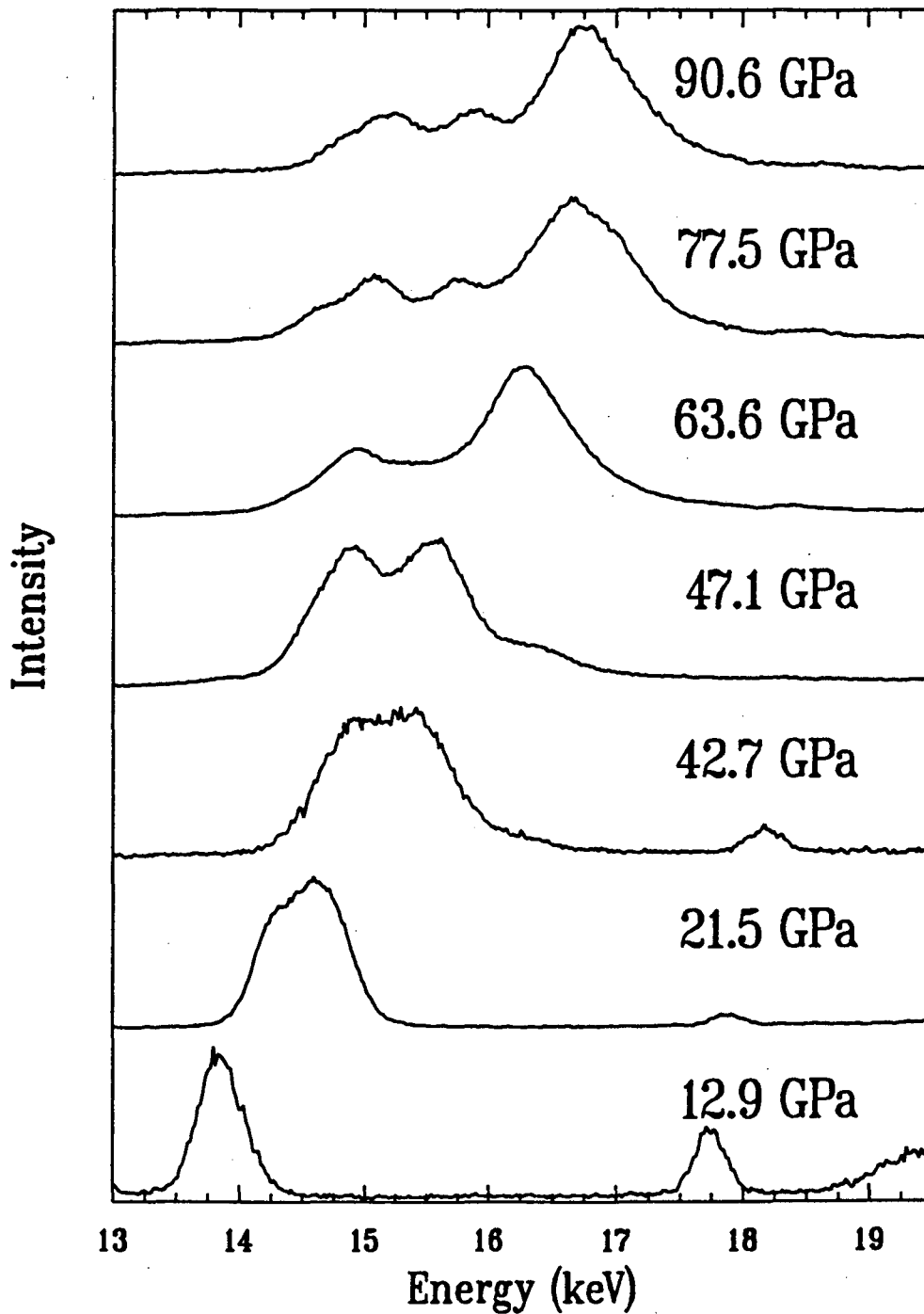


Figure 5.3: A series of diffraction patterns of CsI under increasing pressures. At the start, the (110) and (200) peaks of the B2 phase can be easily identified, as the pressure is increased, the peaks get broader, probably as a precursor of a phase transition. Above 45 GPa, five peaks appear in the region where the original (110) peak was found.

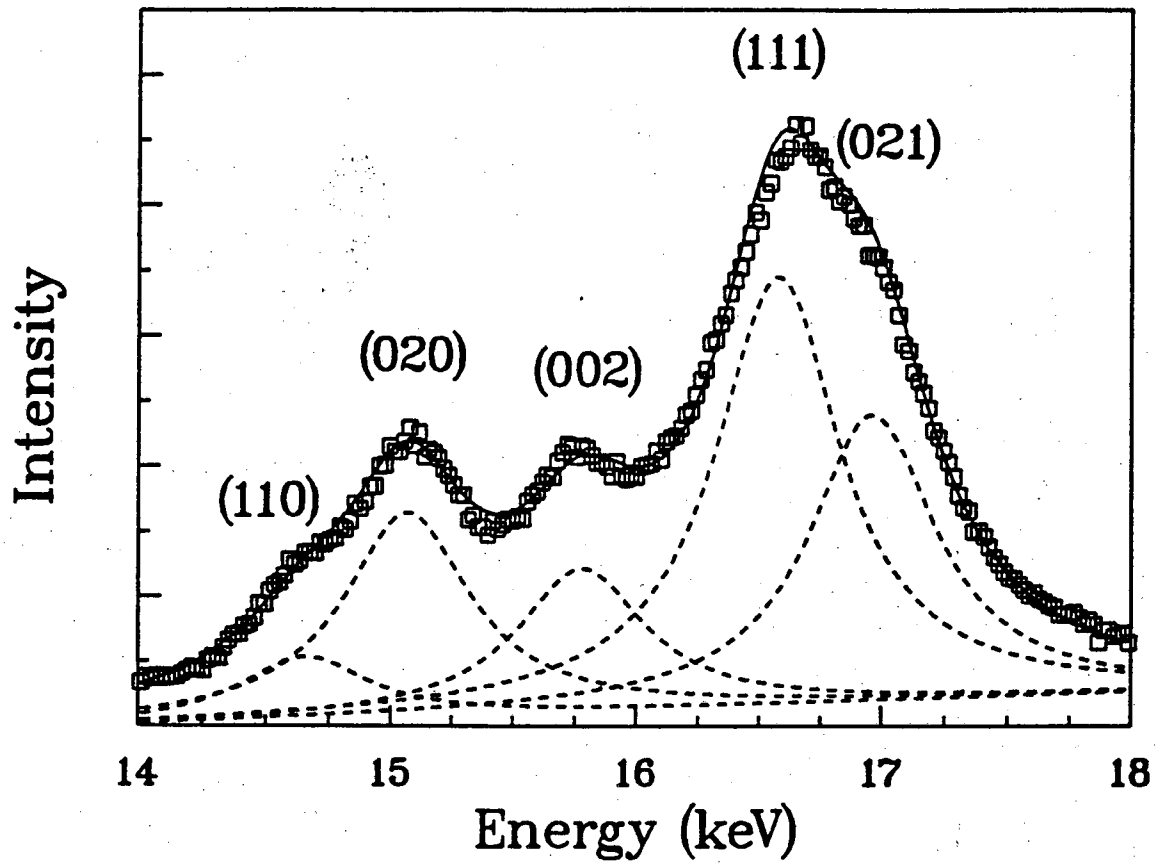
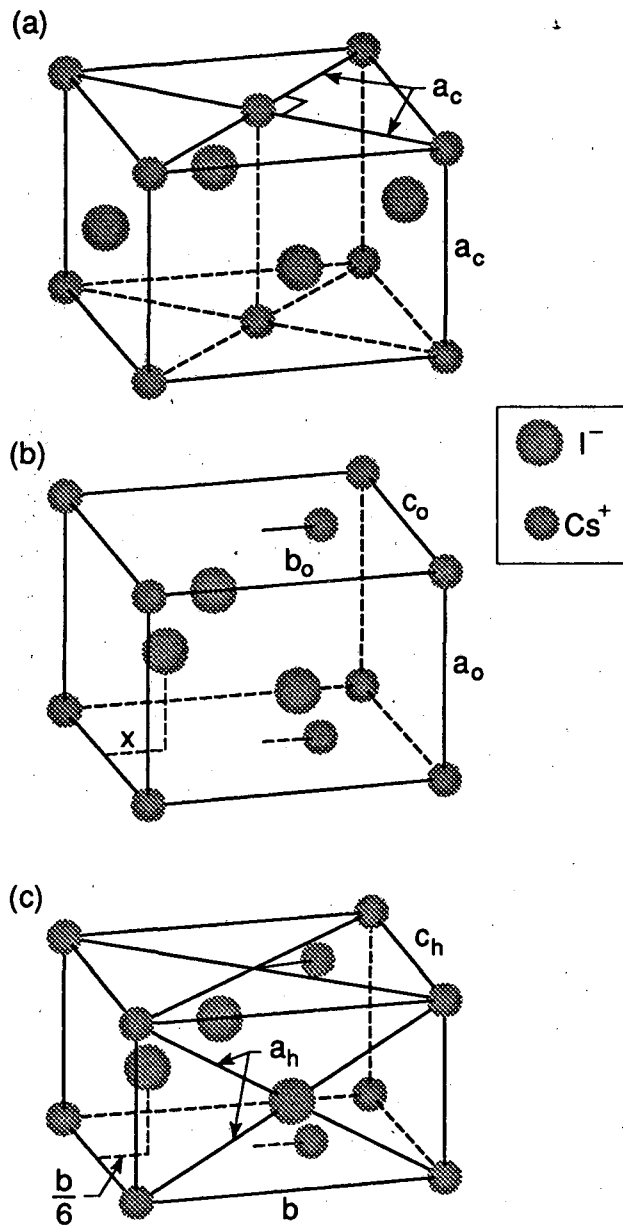


Figure 5.4: The result of a deconvolution shows five peaks in the region where the (110) of the B2 structure should occur. An orthorhombic unit cell can successfully explain this pattern. The pressure at which the pattern was taken is 77.5 GPa.

terns. Figure 5.5 shows the unit cell of this structure and its relationship to B2 and hcp. This new unit cell doubles the size of the original B2 unit cell. If $a_o = a_c, b_o = c_o = \sqrt{2}a_c$, and $x = 0$, then it is identical to the B2 structure. While for $a_o = a_h, b_o = \sqrt{3}a_h, c_o = c_h (c_h/a_h = \sqrt{8/3})$ for ideal hcp close packing), and $x = b_o/6$, it is identical to an hcp lattice. The subscripts above refer to the appropriate unit cells(c for the cubic, o for the general orthorhombic, and h for the hcp cell). The space group for the general orthorhombic cell is D_{2h}^5 , but because the difference in scattering power of Cs^+ and I^- for the energy range(no anomalous scattering) used in the current experiments is small, there are additional extinction rules. Furthermore, the value of x affects the extinction rules and relative intensities of the diffraction patterns. Table 5.4 shows the relationship between the diffraction peaks from the B2, orthorhombic and hcp structures. It is seen that the (110) peak of B2 splits into 3 peaks in the orthorhombic structure. Two additional peaks that are forbidden in the original cell also appeared. Together with the previous three peaks, they constitute the five peaks that we observed experimentally. As the ratios between the axes are further changed, the five peaks converge into three peaks that exist in the hcp structure.

All thirteen diffraction lines predicted for this orthorhombic structure with spacings larger than and including that of (202) can be identified. Table 5.5 gives a comparison of some calculated d-spacings with observed ones for two different pressures. Most of the difference between the observed and calculated values can be accounted for by either the intensity of the given peak is too weak or there are severe overlapping between neighboring peaks so an accurate determination of the line position is impossible. Despite this, the overall agreement is quite good. There are no lines left unidentified in all diffraction patterns.

Depend on the starting condition, the intensities of individual diffraction peaks showed quite large variations. In the CI series, we started with fine powder so there is no strong preferred orientation to start with. In the CSI series, we started with



XBL 907-5904
lg/M

Figure 5.5: The orthorhombic unit cell of CsI under high pressure and its relation to the low pressure B2 and ultra high pressure hcp structure. (a) The B2 unit cell is obtained when $b_o = \sqrt{2}a_o$, $c_o = \sqrt{2}a_o$ and $x = 0$ with the cubic unit cell parameter $a_c = a_o$; (b) The general orthorhombic cell; (c) The ideal hcp lattice is obtained when $b_o = \sqrt{3}a_o$, $c_o = \sqrt{8/3}a_o$ and $x = b_o/6$ with the hcp unit cell parameters $a_h = a_o$, $c_h = c_o$.

Table 5.4: The relationship between the diffraction peaks from the B2, the orthorhombic, and the hcp structures. We have only listed the lines that have non-zero intensity in the general orthorhombic cell. The two ions are assumed to have the same diffraction power.

B2	Orthorhombic	hcp
$(\frac{1}{2}\frac{1}{2}1)$	(110)	} (100)
{ (110)	(020)	
	(002)	(002)
$(\frac{3}{2}\frac{1}{2}0)$	(111)	} (101)
{ $(\frac{3}{2}\frac{1}{2}1)$	(021)	
	(200)	(112)
{ (200)	(022)	
	$(\frac{3}{2}\frac{3}{2}1)$	(200)
{ (211)	(130)	
	{ (211)	(131)
$(\frac{5}{2}\frac{1}{2}0)$		(113)
{ (211)	(023)	
	{ (211)	(220)
		(202)

* This line is extinct in the hcp structure.

Table 5.5: A comparison of calculated interplanar spacings with observed values.

Index	$P = 47 \text{ GPa}^a$		$P = 78 \text{ GPa}^b$	
	$d_{obs}(\text{\AA})$	d_{calc}	$d_{obs}(\text{\AA})$	d_{calc}
(110)	2.863(2)	2.898	2.686(2)	2.682
(020)	2.717(6)	2.699	2.651(2)	2.651
(002)	2.663(1)	2.683	2.527(1)	2.514
(111)	2.544(1)	2.550	2.387(1)	2.367
(021)	2.440(1)	2.411	2.332(1)	2.339
(112)	1.979(1)	1.969	1.871 ^c	1.834
(022)	1.897(1)	1.903	1.820(1)	1.821
(200)	1.715 ^c	1.718		
(130)	1.588(1)	1.588	1.530(1)	1.533
(131)	1.523(3) ^c	1.528		1.467
(113)		1.522	1.436 ^c	1.421
(023)	1.493(3) ^c	1.491		1.415
(220)	1.454(3) ^c	1.449	1.345(1)	1.341
(202)	1.434 ^c	1.446	1.318(2)	1.323

a. $a = 3.435(18)\text{\AA}$, $b = 5.398(21)\text{\AA}$, $c = 5.366(24)\text{\AA}$, $b/a = 1.571$, $c/a = 1.562$.

b. $a = 3.113(9)\text{\AA}$, $b = 5.285(18)\text{\AA}$, $c = 5.049(25)\text{\AA}$, $b/a = 1.697$, $c/a = 1.615$.

c. These lines were not used in the least-square fits for obtaining lattice parameters due to insufficient statistics in multiplet deconvolution.

a single grain and observed a strong preferred orientation effect. In fact, in the B2 phase, the pattern was dominated by the B2 (211) peak. After the transition, although other diffraction lines can be observed, it was still dominated by the (130) peak in the orthorhombic phase. It can be easily verified that the angle between the normal of the {130} planes in the orthorhombic structure and the {211} planes in the B2 structure is rather small. This correlation indicates a large grain was maintained even after the phase transition. This further suggest that the phase transition should be displasive and does not involve movement of atoms beyond a unit cell dimension, in accord with our proposed structure and transformation mechanism.

While above 45 GPa, it is certain that there are five peaks near the original (110) line of B2. It is less certain about the situation below 40 GPa. The current study shows significant broadening of the peak is observable at pressure as low as 15 GPa. More than one line is already present in a diffraction pattern taken at a pressure of 21.5 GPa(Fig. 5.3). The broadening is also reported in at least one previous study[56]. In order to gain a better understanding in the nature of the phase transition in this pressure range, we turn to the three high resolution ADXD studies.

The pressure volume data for CI run are presented in Table 5.6. The volume was calculated based on the orthorhombic cell for pressures above 40 GPa as explained above. For pressures between 15 to 40 GPa, a tetragonal unit cell is used(See discussion in next section). For pressures less than 15 GPa, the B2 unit cell is assumed.

5.4.3 Nature of the phase transition in the low pressure range

Three high resolution Angular Dispersive X-ray Diffraction (ADXD) runs were carried out to examine the origin of the peak broadening below 40 GPa observed in

Table 5.6: Volume per atom of CsI as a function of pressure under high pressure in the CI run.

Pressure(GPa)	σP	Volume($\text{\AA}^3/\text{atom}$)	σV
8.21	0.29	35.85	0.01
9.72	0.32	34.55	0.01
12.92	0.37	33.07	0.01
14.33	0.40	32.55	0.01
14.81	0.38	32.07	0.01
16.12	0.40	31.58	0.01
19.52	0.44	30.35	0.01
23.69	0.48	28.85	0.19
21.53	0.51	28.80	0.02
21.06	0.65	28.66	0.04
25.52	0.58	27.52	0.03
31.06	0.58	27.55	0.12
31.77	0.78	26.49	0.03
34.95	0.74	26.12	0.06
38.55	0.72	26.13	0.09
42.67	0.87	25.23	0.06
46.49	0.86	24.78	0.06
47.07	0.84	24.83	0.15
55.56	0.90	23.96	0.04
57.23	1.13	23.44	0.10
63.76	1.25	22.97	0.03
71.02	1.77	22.10	0.03
70.06	1.29	22.00	0.05
77.46	1.45	21.29	0.03
83.60	2.56	20.95	0.06
83.79	2.39	20.74	0.02
91.17	1.54	20.28	0.02
86.91	1.68	20.80	0.07
90.56	1.76	20.58	0.05
94.14	1.60	20.47	0.04
98.22	2.05	20.04	0.03
97.31	1.91	20.06	0.04
100.88	2.00	19.93	0.13
101.43	2.49	19.91	0.04

the previous runs. The differences among these three runs were mainly the pressure medium used.

Figure 5.6 shows the observed peak width in the first two of the three runs. In the first run, where no pressure medium was used, the diffraction peaks quickly get wider as the pressure is increased. Significant broadening can be seen even at a pressure as low as 5 GPa. Since the pressure variation over the sample area within the x-ray beam can also induce a broadening in the diffraction peaks, the observed broadening can not be definitively attributed to a possible phase transition. In fact, in the second run with Ethanol:Methanol (ratio 1:4) as pressure medium, the peak broadening is significantly reduced. At a pressure of 8 GPa, which is just above the fluid-glass transition for the pressure medium, the peak width is almost the same as the zero pressure peak width. However, as pressure is increased beyond 10 GPa, the peaks again begin to broaden. Unfortunately, there again two possible reasons for the peak broadening: the pressure variation or the precursor of a structure distortion.

In order to get a definitive answer about whether there is broadening that is due not to the pressure variation, a pressure medium that is softer than CsI throughout the pressure range is desired. We have used Ne for this purpose. Although Ne is known to solidify at a pressure as low as 3 GPa, it is also known that even in the solid phase, it is a very soft material[78]. Fig. 5.7 compares the bulk modulus of Ne with that of CsI derived from the isotherm at room temperature, it is seen, indeed, solid Ne is much softer than CsI. Fig. 5.8 shows a series of diffraction patterns selected from this run. The identification of the lines are shown in Fig. 5.9. Two points are worth noting in these patterns. (1) The diffraction peaks from CsI are rather sharp and do not show significant broadening at the beginning of the run, despite the starting pressure of about 18 GPa. There is no possible phase transition to at least this pressure when CsI is in the Ne medium. (2) The broadening of CsI peaks as pressure is further increased is readily seen. In particular, the widths of

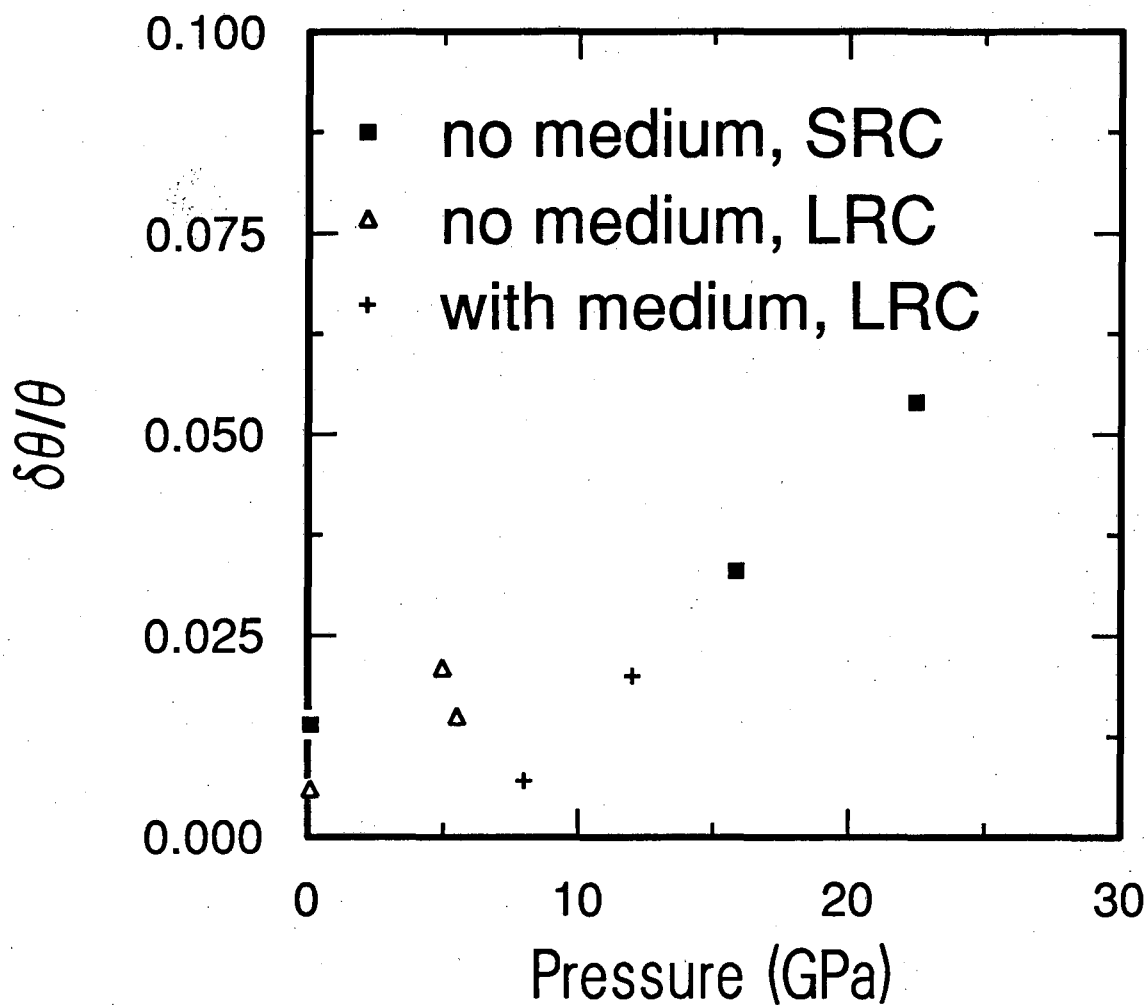


Figure 5.6: The peak width (FWHM) of diffraction peaks of CsI as a function of pressure for both no pressure medium and ethanol:methanol(1:4) pressure medium. Significant broadening is seen in the no medium run at a pressure as low as 5 GPa, however, with pressure medium, this broadening does not appear below 10 GPa. The label SRC refers to small radius camera, where the radius of the camera was 114.6 mm, and the label LRC refers to the large radius camera with radius of 286.5 mm. Different radius camera were used to exclude the possibility that the observed broadening is due to excessive angular divergence caused by grain size and other possible effects.

Table 5.7: Pressure-volume data for the ADXD run with Ne as the pressure medium

Run number	P(GPa)*	V (Å ³ /molecule)
csi1	18.05	60.20
csi2	18.62	59.11
csi3	22.61	57.66
csi6	26.11	54.75
csi7	30.51	52.39
csi8	31.22	52.08
csi9	33.88	53.22
csi14	25.62	56.10

* The pressures were calculated based on Solid Ne diffraction lines using the equation of state of Hemley *et al.*[78]

the CsI diffraction lines are becoming wider than the widths of the Ne lines. This is more clearly demonstrated in Fig. 5.10 where we have shown the intensity profile of a diffraction pattern recorded on an imaging plate. Since for a given pressure variation ΔP , the resulted variation in the unit cell volume is

$$\Delta V = \frac{V}{B} \Delta P,$$

where B is the bulk modulus at the mean pressure. The variation in lattice interplanar spacing is thus $\Delta d = \frac{1}{3} d \Delta V / V$. It is clear that the broadening of diffraction peak is therefore inversely proportional to the bulk modulus of the material. Since we have observed that the peakwidth of CsI is wider than that of Ne, pressure variation alone can not account for it. We will discuss a possible reason for the observed broadening in the next section.

The current data do not show clearly whether the peaks actually have split, so a new structure assignment is not possible. For the purpose of calculating the volume data, we have assumed the same B2 structure throughout this run. The pressure volume data thus obtained are listed in Table 5.7.

From these three runs, it can be concluded that the CsI diffraction peaks get broaden even in a pressure medium as soft as neon. The pressure at which that

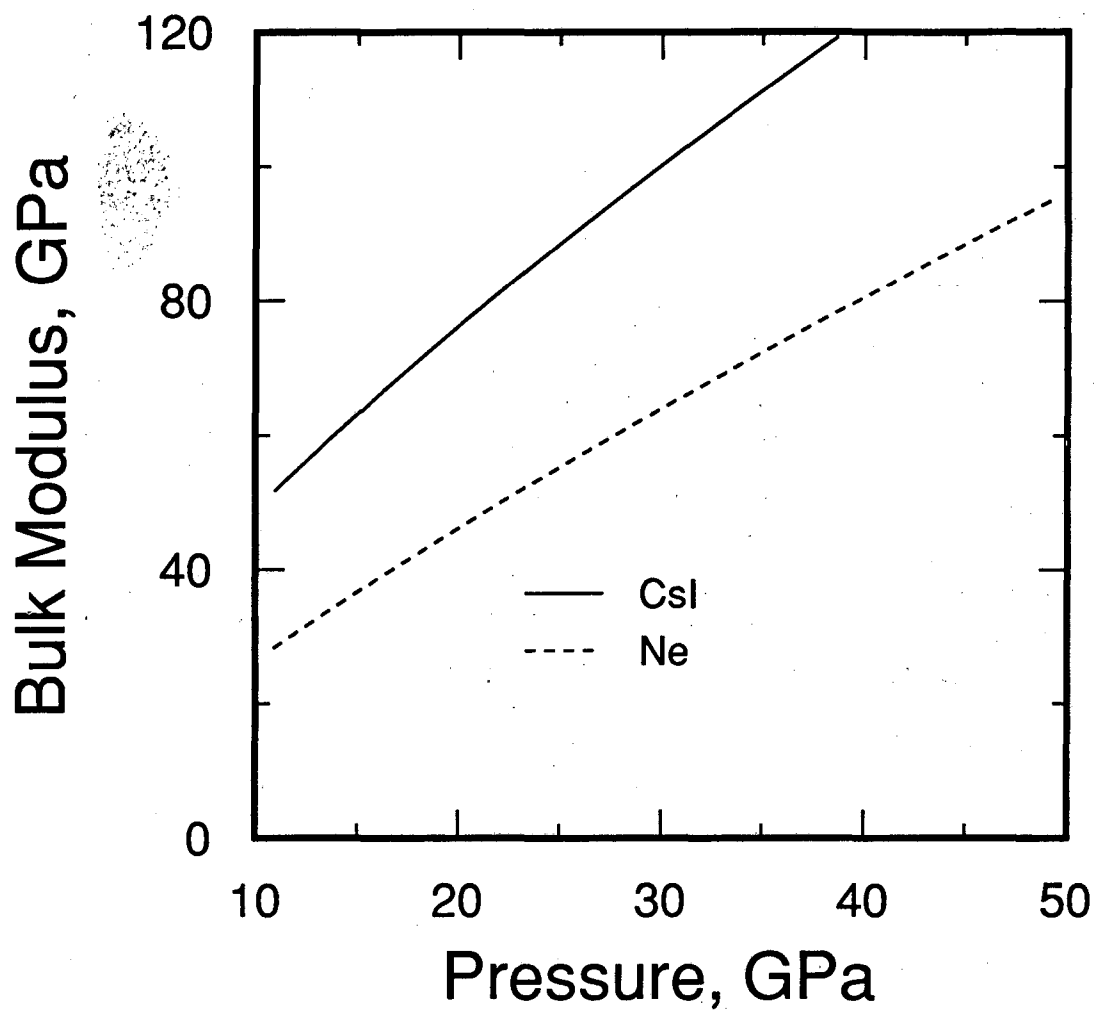
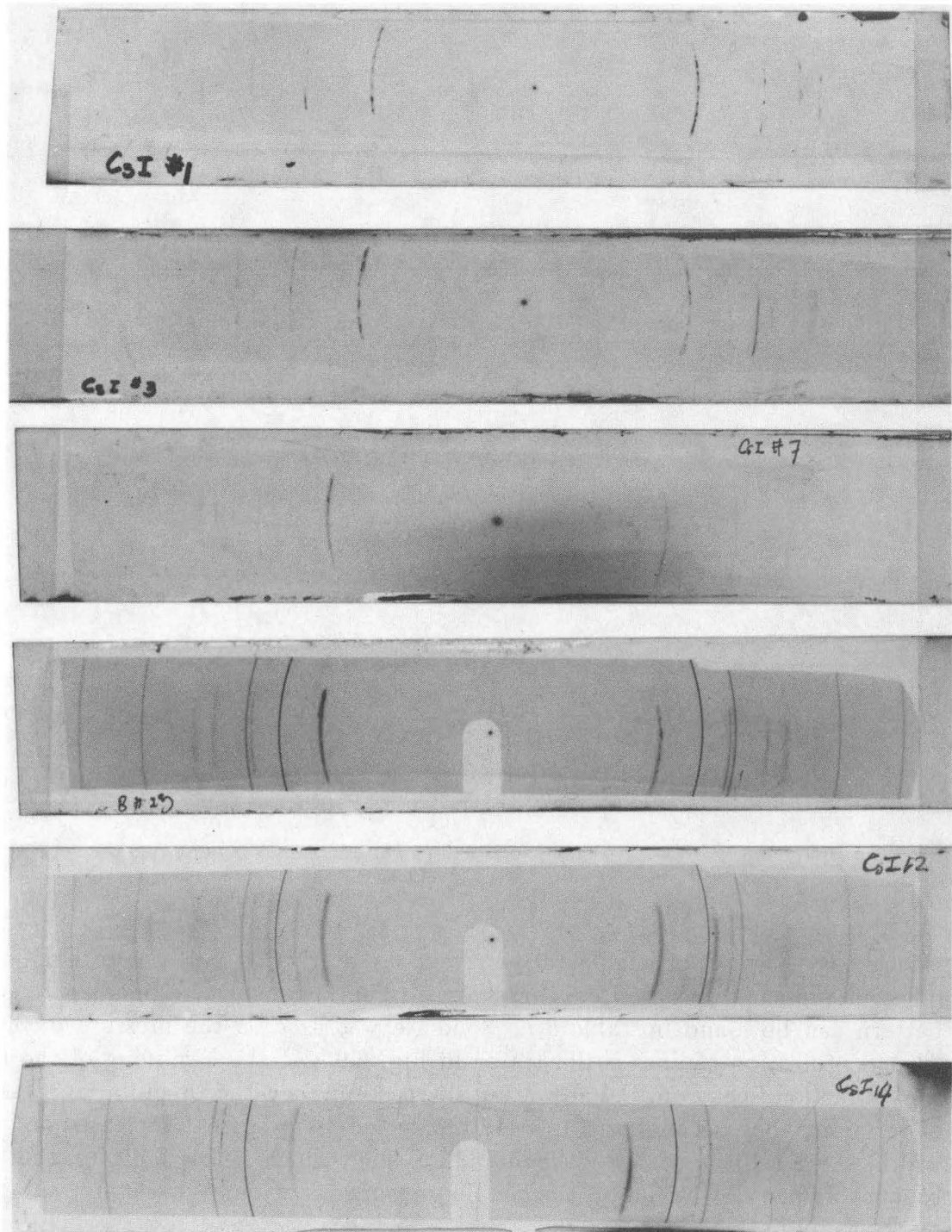


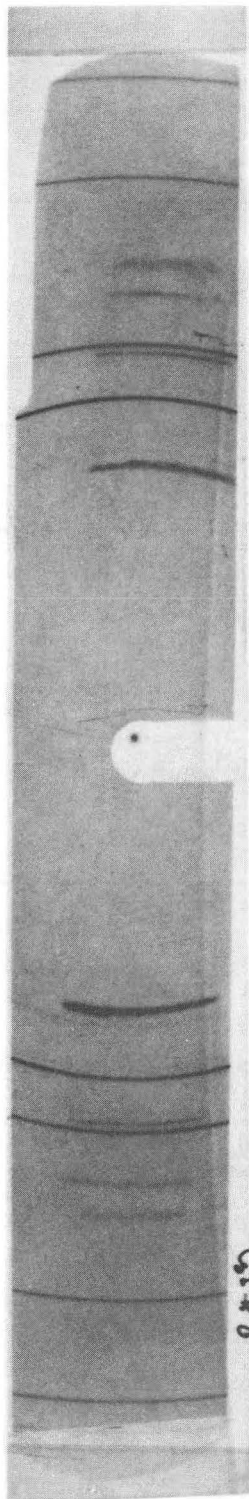
Figure 5.7: A comparison of isothermal bulk moduli of CsI and Ne at room temperature under high pressure. They were calculated based on the equation of state derived in the study for CsI and Hemley *et al.*[78] for Ne.



XBB 906-4572

Figure 5.8

Figure 5.8: A series of angular dispersive x-ray diffraction patterns of CsI under different pressures recorded on X-ray films. The pressure corresponding to each pattern can be found in Table 5.7. Solid Ne was used as the pressure medium. The identification of lines is illustrated in Fig. 5.9. At the beginning of the run, the diffraction lines from CsI are rather sharp despite a rather high initial pressure of 18 GPa. They become progressively broadened as pressure is increased and the widths surpassed the widths of Ne diffraction lines, which clearly indicates that the broadening can not be due to the simple pressure variation over the area sampled by the x-ray beam.



— Ne (200)
— Ne (111)

— CsI (110)

— Cu (111)
— Cu (200)

— CsI (211)
— Cu (220)
— Cu (311)

XBB 906-4573

Figure 5.9: The identification of diffraction lines.

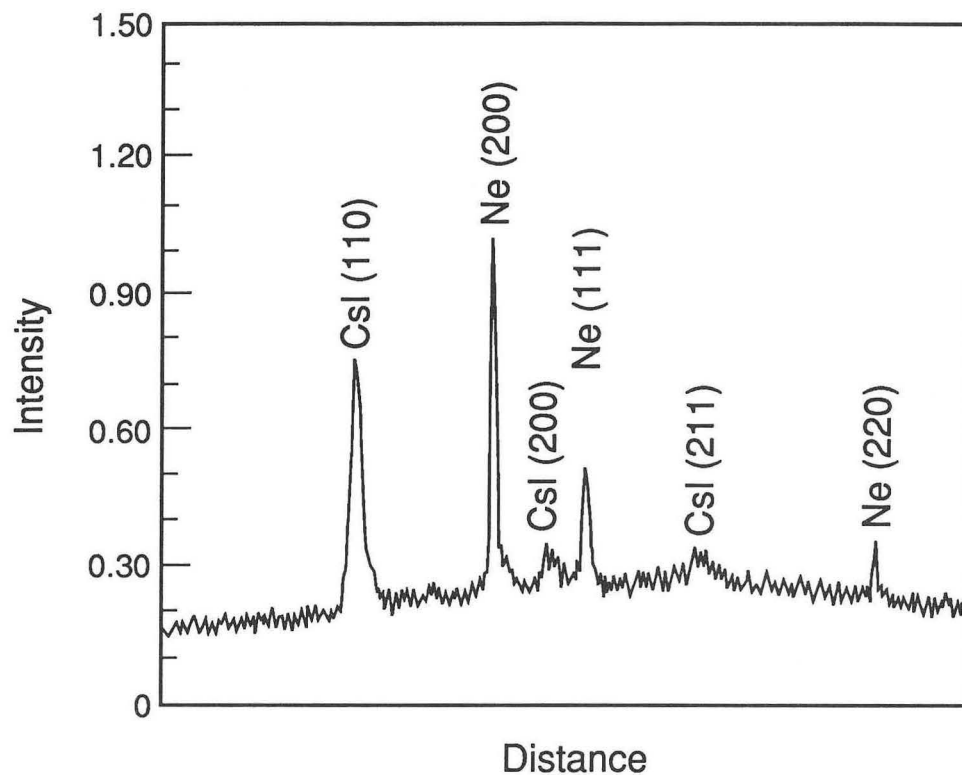


Figure 5.10: The intensity profile of the diffraction peaks of CsI and Ne under a pressure of 26 GPa and room temperature. This is obtained by summing over a small arc along the Debye-Scherrer ring of the two dimensional pattern as recorded on an imaging plate. The intensities are expected to reflect accurately the actual x-ray intensities because the imaging plate's response is linear for a large range of X-ray exposure. The (111), (200), (220) of fcc Ne peaks and the (110), (200), (211) of B2 CsI peaks can be easily identified. The latter is much broader than the Ne peaks which indicates the peak broadening is not due to simple pressure variation over the illuminated area.

the broadening starts to occur and the amount of broadening seem to depend on the pressure environment. This broadening can not be accounted for solely by the pressure variation across the sample area.

5.5 Equation of State (EOS) of CsI

5.5.1 Quasi-hydrostatic compression and non-hydrostatic compression: comparisons with previous static compression studies

We have seen that the B2 structure of CsI is not stable under high pressure, at pressures above about 40 GPa, the structure of CsI can be described in an orthorhombic unit cell which is intermediate between the B2 structure and the ideal hcp lattice. This orthorhombic cell changes continuously into the ultra high pressure phase of CsI, which has an hcp like structure.

For pressures below 40 GPa, our present systematic study indicates that there is significant broadening in the diffraction peaks that cannot be attributed to the pressure variation. The starting pressure of the broadening depends on to what extent the pressure was hydrostatic, which in turn is determined by what pressure medium is used. It is higher in a weaker pressure medium than in a stronger pressure medium. Along with the previous observation that this starting pressure also depends on the loading rate[79], we suggest CsI behaves differently under non-hydrostatic and hydrostatic compression. If the pressure environment is quasi-hydrostatic with non-hydrostatic stress below a critical value, the zero pressure B2 structure can be preserved to a pressure of nearly 40 GPa. If the non-hydrostatic stress exceeds the critical value before reaching this pressure, a distortion from the B2 structure results. This distortion is the result of the nonhydrostatic environment and is responsible for the observed peak broadening. A tetragonal distortion with ($a = b > c$) in terms of the B2 cubic unit cell seems to be a likely candidate because it lies intermediate between the two phases across the phase transition boundary.

This distortion is usually rather small and the resulting splitting of the diffraction peaks can not be readily resolved (because of low detector resolution and pressure gradient effects). If a single line is assumed in the calculations of interplanar spacings, it corresponds to taking an arithmetic average over the actual values. Since the volume is related to the geometric average of the lattice parameters, it is expected the volume calculated from the lattice parameters calculated assuming only a single line will give a volume larger than the true value. And as we shall see, this is indeed what has been observed in the experiments.

It should be pointed out that the non-hydrostatic stress is determined not only by the strength of the pressure medium used, but also by the dimensions of the pressure vessel. In the diamond anvil cell experiments where the thickness h of the sample chamber is usually much smaller than the lateral dimensions, the pressure gradient in the radial direction is given by

$$\frac{\partial P}{\partial r} = \frac{\sigma}{2h},$$

where σ is the shear stress which is limited by the strength of the sample or the pressure medium. For the same pressure medium and a given pressure gradient, if the sample is thicker, the shear stress is smaller and the environment is closer to being hydrostatic.

With these introductions, we are now in a position to examine all the data presented here as well as data from previous studies.

From the outset, we should expect the compression curve to start from a single line since at low pressures the environment is close to being hydrostatic. As the pressure increases, the volumes should lie between two extremes, corresponding to the hydrostatic limit and non-hydrostatic limit (which is dictated by the shear strength of CsI itself). At much higher pressures, they should merge into a single curve again because there is no truly hydrostatic environment.

We have summarized the quasi-hydrostatic compression studies in Fig. 5.11. The experimental data obtained by Bridgman[47, 48] should follow the hydrostatic limit

because the samples used in his piston cylinder experiments were quite large. Although Hammond's experiment[50] was performed in a diamond cell, a relatively thick sample could be used since the pressures were rather low. Our data from the run with Ne pressure medium should also follow the hydrostatic limit. Although we have seen some progressive broadening as the pressure is increased, the distortion due to the non-hydrostatic stress is apparently too small to produce an observable deviation in unit cell volume from the more hydrostatic data(*i.e.* He pressure medium). The more recent study of Aleksandrov *et al.*[80] where He was used as the pressure medium seems to best approximate a hydrostatic pressure environment under these pressures. No significant broadening is seen in the single crystal diffraction peaks up to the highest pressure studied (50 GPa). Below the pressure where a phase transition is observed (40 GPa), the volumes calculated based on the cubic B2 unit cell are in excellent agreement with studies described above. The most interesting case is the compression data [59] obtained using Xe as the pressure medium. At very low pressure, the data obviously agree well with other quasi-hydrostatic studies. But as pressure is increased above 6 GPa, a significant deviation starts to show up. We suggest this happens because the nonhydrostatic stress at this point becomes large enough to cause a significant distortion of the cubic structure. As explained earlier, if the splitting is not taken into account, the resultant unit cell volume will be larger. The deviation increases as the pressure is further raised, approaches and then crosses our non-hydrostatic compression data. This is in complete accord with our analysis earlier in this section.

The non-hydrostatic compression studies on CsI can be divided into two categories. The studies[52, 53] performed on laboratory x-ray machines normally used a large ($> 50\mu m$ in diameter) x-ray beam, therefore the pressure gradient that existed across the sample rendered an observation of the splitting of lines due to distortion prior to the phase transition at 40 GPa impossible. The apparent low resolution achieved in the previous synchrotron studies[55, 61] is probably due to the particular detector used or a large collection angle in front of the detector. The observation of

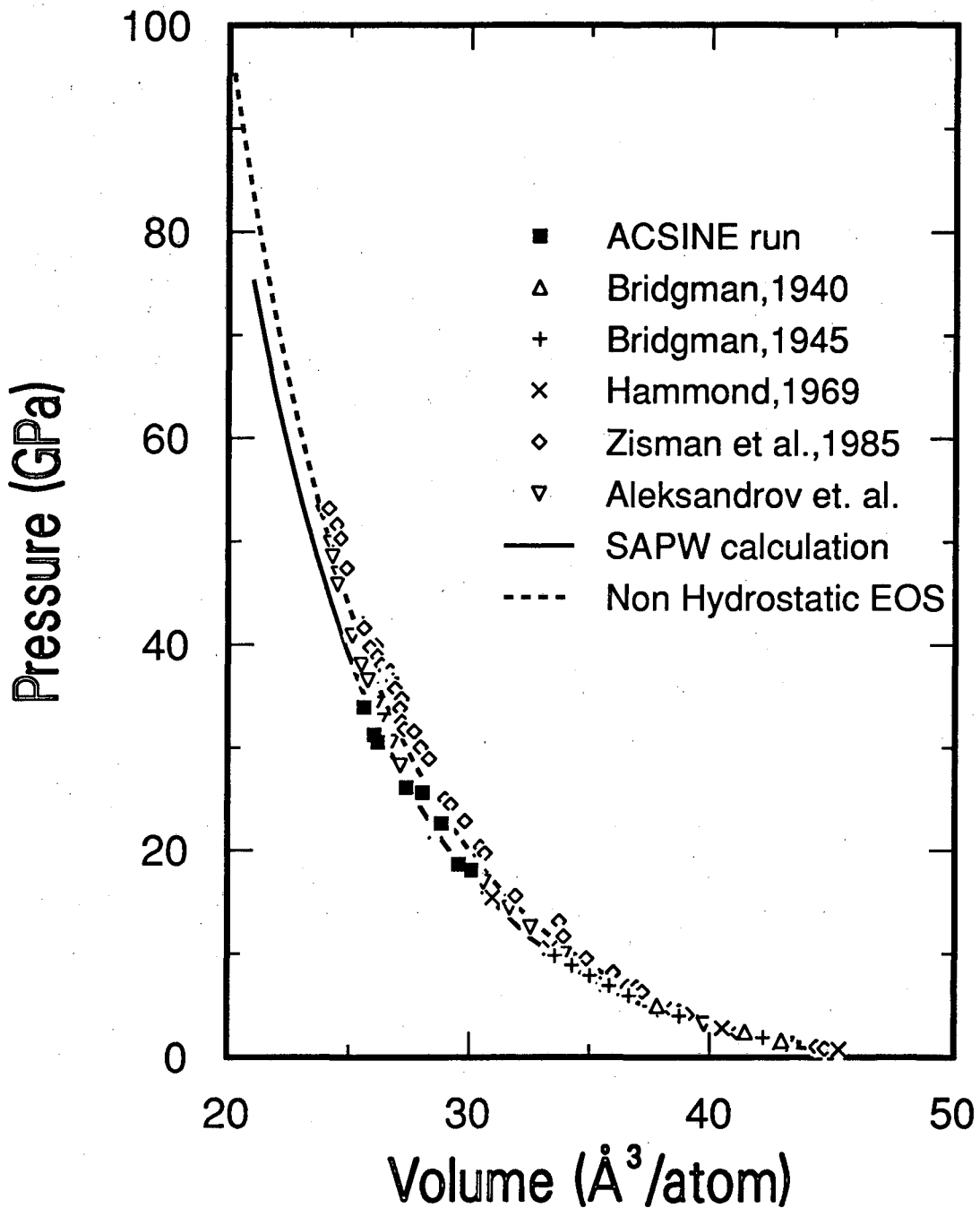


Figure 5.11: The compression data of CsI under quasi-hydrostatic compression. A quasi-hydro static environment in this case refers to where the non- hydrostatic stress is less than a certain critical value above which a significant distortion from CsI zero pressure's cubic structure exists. We have included data from large sample studies of Bridgman, Hammond and those studies using a soft material as pressure medium. The solid curve is the result of the APW calculation [68] and is used as a guide to the eyes. The dashed line is the result of our non-hydrostatic compression data shown for comparison.

Table 5.8: The zero pressure isothermal bulk moduli and its pressure derivatives of CsI derived from previous static studies and present results. We have also included the values obtained from ultrasonic studies of Barsch and Chang[87].

EOS	B(GPa)	B'	$B''(\text{GPa}^{-1})$	reference
Keane	11.89	5.93	-1.31	[55]
Birch	11.10	6.90		[52]
Birch	11.89	6.27		[61]
Vinet	12.45	5.71		Present Study
	11.89	5.93	-0.73	[87]

the distortion was not possible. In these studies, the cubic phase is assumed below the phase transition, which resulted an overestimation of the unit cell volumes. Our current study apparently achieved a higher resolution and enabled us to resolve the splitting of the lines well below the phase transition pressure. Calculation based on a tetragonally distorted unit cell reduces the unit cell volumes of previous studies.

The most important difference came from the phase identification above the phase transition pressure of 40 GPa. Our newly identified structure is rather different from the previous studies and this has reduced the unit cell volume significantly from the previous studies. Previous compression studies can also be analyzed in our new structure where data are available. We present in Fig. 5.12 a comparison of our results with some previous studies which we believe to be non-hydrostatic in nature. The data from previous studies are obtained either from literature[54, 59] or calculated from the values of the isothermal bulk modulus and its pressure derivatives [52, 55, 61] which are listed in table 5.8. Some of the data points of Knittle and Jeanloz above 40 GPa have been reanalyzed in terms of the new structure. As can be seen, the corrected data are in rather good agreement with our results. The only data set that can not be account for is the one by Huang and Ruoff[55]. Their fitted equation of state is very close to ours. If a similar amount of correction as to other studies is made, it will appear to be much more compressible.

It is now clear that despite the small yield strength of CsI, there is a de-

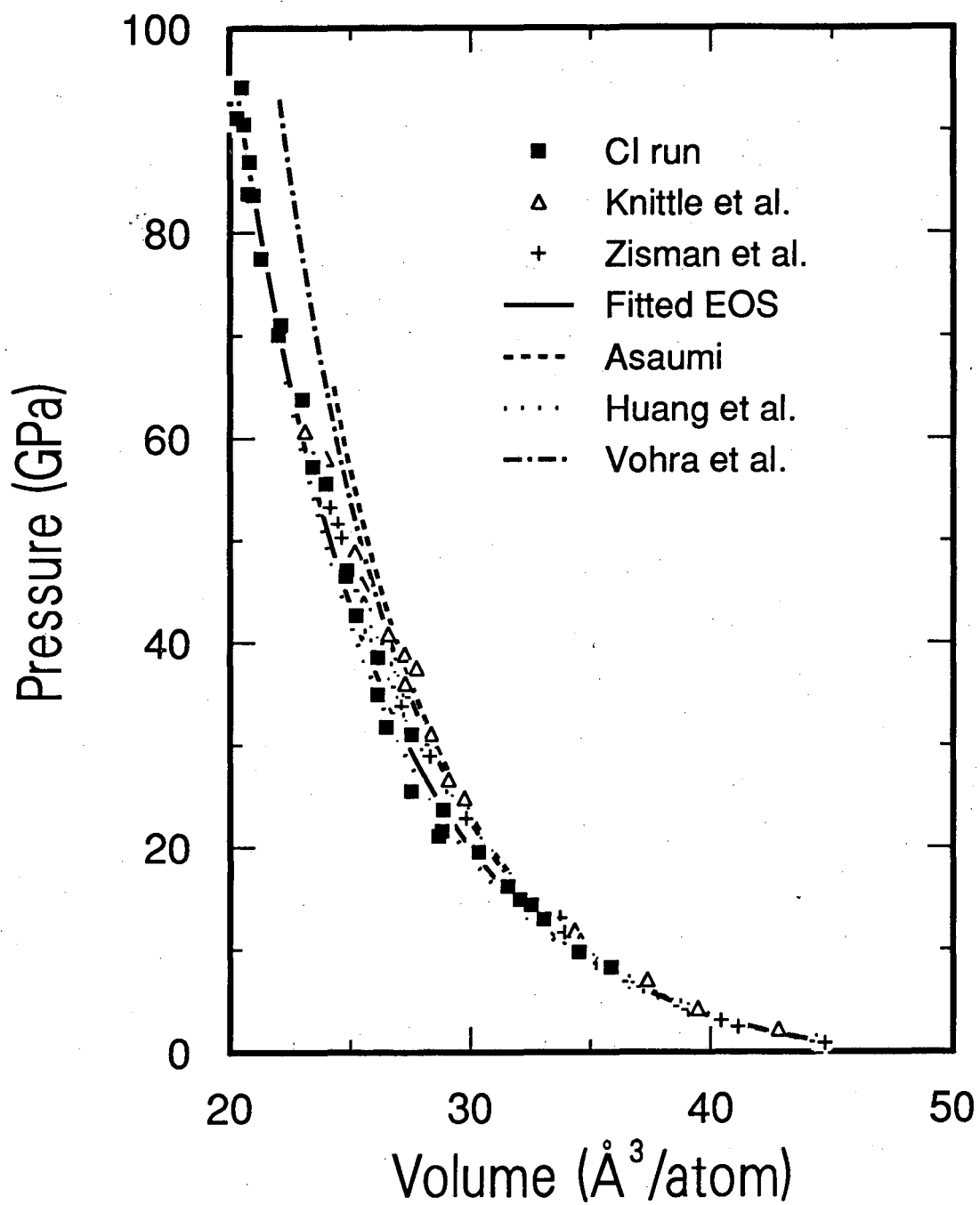


Figure 5.12: Comparison of current non-hydrostatic compression data with results from previous static compression studies.

tectable difference in the equation of state under hydrostatic compression and non-hydrostatic compression. This difference is responsible for the apparent small discrepancies among some earlier compression studies where larger samples were used, more recent studies to higher pressures with smaller samples, and studies with soft pressure media. By proper treatment of the data obtained in each of these studies, excellent agreement among these data can be found. Compared to other materials, the effect of distortion in the crystal structure in CsI is made more apparent because the large value of its compressibilities. Similar effects in other materials are expected to be much smaller.

The effect of this observation to the phase transition in the hydrostatic limit is worth commenting on. The only experiment that may be classified into this category is the one by Aleksandrov *et al.*[80]. If we assign the three observed peaks after the phase transition to be (020), (002), and (111) of the orthorhombic structure, the volume thus calculated shows no observable discontinuity from the lower pressure phase. Therefore, the phase transition from the B2 to the orthorhombic structure does not involve a noticeable volume discontinuity even in the quasi-hydrostatic limit.

5.5.2 Implication to the validity of various EOS formulations at ultra high pressures

There are two major consequences from our results on the structure of CsI under high pressure and ultra high pressure studies. The ultra high pressure study represents the first observation of ionic solids under such large compression. The newly identified structure may also exist in other ionic solids at high pressures. The structure in the intermediate pressure range give clues to the phase transition sequence and also helps to resolve a major controversy that exists between previous studies on CsI under high pressure. We will defer these discussions into a later section. Here we would like to concentrate on another separate issue: the implication of the current study on empirical equation of state formulations.

The relation between the pressure, volume and temperature are usually termed as the Equation of State (EOS) for a given material. More specifically, in static high pressure studies, we commonly deal with a constant temperature, so we mostly deal with isotherms. Unlike ideal gas systems, there is no simple theoretically derived exact form of equation of state for solids. Various empirical forms have been proposed in the past studies, each with different degree of success. Naively, one would think we can always expand the decrease of fractional volume ($1 - V/V_0$) as a power series in pressure P , *i. e.*

$$1 - V/V_0 = aP + bP^2 + \dots$$

where $a, b, \text{etc.}$ are parameters to be determined by fitting to experimental data. This is fine for low pressures. In fact, early high pressure studies used this to describe experimental data. One major drawback is that this series does not seem to converge, so the validity of this formulation is really very limited. Also, this form does not give meaningful results as P gets to be large. Clearly, a better formulation is necessary.

Murnaghan's EOS was first proposed in the 1930's[81]. The idea behind this EOS is that if we assume the bulk modulus B at pressure P is a linear function of P , $B(p) = B_0 + B'_0 p$, then by integrating this equation, we can obtain the Murnaghan EOS (we'll refer to it by M-EOS in subsequent discussions).

$$P = B_0 \left(\left(\frac{V_0}{V} \right)^{B'_0} - 1 \right) \quad (5.1)$$

This equation behaves much better than the polynomial EOS, and does show reasonable asymptotic behavior as P increases. This equation is widely used in the literature. One of the nice features of this EOS is that it is analytically invertible and can easily be integrated to yield the relation between the Gibbs free energy as a function of volume. However, the correctness of this EOS at large compression has not been verified.

Instead of expanding the various physical quantities in a simple power series of pressure as described earlier, one could seek to expand them in terms of certain

strain measure. The choice of the strain measure is rather arbitrary. The Eulerian formulation of this theory is now commonly used in Geophysics and in the presentation of static high pressure work.

For a quenchable phase or low pressure phase (where a volume can be measured at zero pressure), the strain measure used is the negative of the Eulerian(spatial) strain $f = -e$ where

$$f = 1/2[(V_0/V)^{2/3} - 1]$$

the total energy of the solid under strain is expanded in powers of f ,

$$E = E_0 + E_2 f^2 + E_3 f^3 + E_4 f^4 + \dots$$

The pressure can be derived from the relation $P = -\frac{\partial E}{\partial V} = -\frac{\partial E}{\partial f} \left(\frac{\partial f}{\partial V}\right)_T$, we obtain

$$F(f) = \frac{P}{3f(1+2f)^{5/2}} = B_0(1 + af + bf^2 + \dots) \quad (5.2)$$

where $a = \frac{3}{2}(B'_0 - 4)$, $b = \frac{1}{6}(9B_0 B''_0 + 9B_0'^2 - 63B'_0 + 143)$ and B_0, B'_0, B''_0 are the bulk modulus and its derivatives at zero pressure.

In principle, this analysis can be carried out to higher orders with more adjustable parameters. Commonly used versions of this EOS truncate at the third or the fourth order term. We would like to restrict ourselves to equations of states with the same number of parameters. Therefore we truncated at the third order term. The resultant EOS is called the Birch-Murnahan EOS (We label it B- EOS here) as it was first derived by Birch[82, 83]. In terms of pressure and volume, it can be rewritten as

$$P = \frac{3}{2}B_0\left[\left(\frac{V_0}{V}\right)^{2/3} - \left(\frac{V_0}{V}\right)^{5/3}\right]\left[1 + \frac{3}{4}(B'_0 - 4)\left(\left(\frac{V_0}{V}\right)^{2/3} - 1\right)\right] \quad (5.3)$$

More recently, Vinet *et al.* proposed a new formulation for the equation of state for solids based on the analysis of a large number of cohesion data and equation of state measurements[84, 85, 86]. There seems to be a universal relation between the total energy and a characteristic distance for materials ranging from metals to

Table 5.9: The result of non-linear weighted least square fitting of two sets of experimental data to three different EOS formulas. The zero pressure volume was fixed at $47.66 \text{ \AA}^3/\text{atom}$ in all cases.

Data	EOS	B_0	B'_0	χ^2
set 1	M EOS	16.76(23)	3.59(3)	122
	B EOS	14.46(23)	4.65(5)	120
	V EOS	12.45(22)	5.71(6)	125
set 2	M EOS	19.90(15)	3.15(1)	390
	B EOS	16.87(13)	4.18(2)	273
	V EOS	13.84(14)	5.34(3)	210

ionic solids. The exploitation of this relation led to the following formulation for the equation of state of solid (labeled V-EOS here):

$$P = 3B_0 \frac{(1-x)}{x^2} \exp\left(\frac{3}{2}(B'_0 - 1)(1-x)\right) \quad (5.4)$$

where $x = (V/V_0)^{1/3}$.

Most studies up to date do not cover a sufficient compression range to make a statistically meaningful comparison. The large compression range ($(V/V_0)_{min} = 0.28$ and $(P/B_0)_{max} = 25$) achieved in this CsI case offers new opportunities in comparing the quality of these equation of state formulations. Since only data for non-hydrostatic compression are available to ultra high pressures, we restrict ourselves to the data in this category. Specifically, using the pressure volume data presented in Table 5.3 and 5.6, we fitted the three equations of state as discussed above to the experimental data. The detail of the fitting procedure can be found in Appendix A. Two data sets were used in the current fitting procedure. They are (1) only data from the run CI where maximum pressure is 100 GPa and (2) Both data sets CI and PTCSI combined. Table 5.9 presents the results of the fitting.

It can be seen in case (1) that differences in χ^2 are very small which indicates that the fit to the three equations of state are of similar quality. But for case (2), the Vinet EOS is clearly preferred. Figure 5.13 and 5.14 also show the fitted curve along with the experimental data.

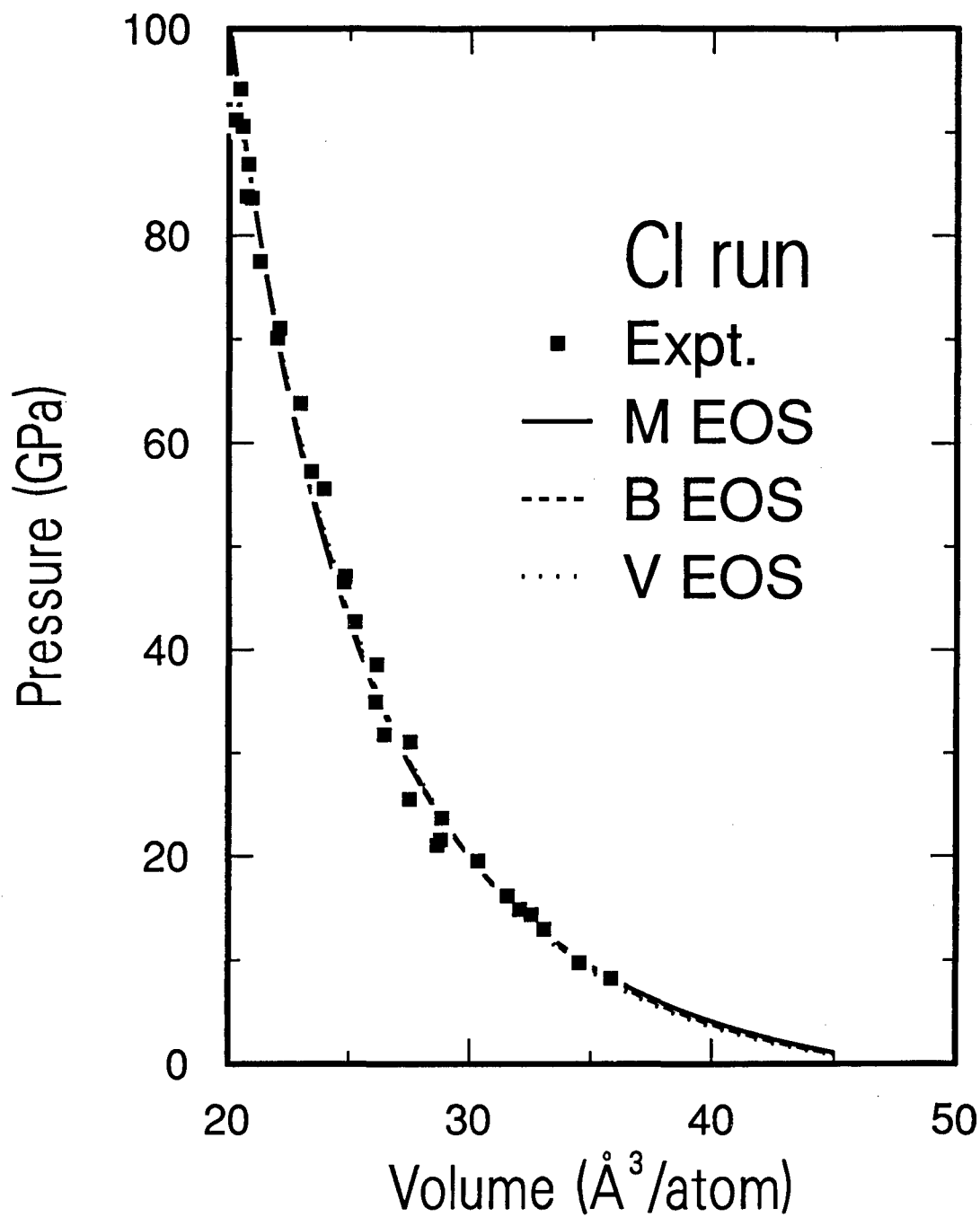


Figure 5.13: Comparison of weighted least square fits to three different EOSes with our experimental data. The residues in these three fits are comparable in magnitude which means the three different expression can describe our experimental data equally well. Note: if we include some low pressure data, it is expected that the situation will not be the same.

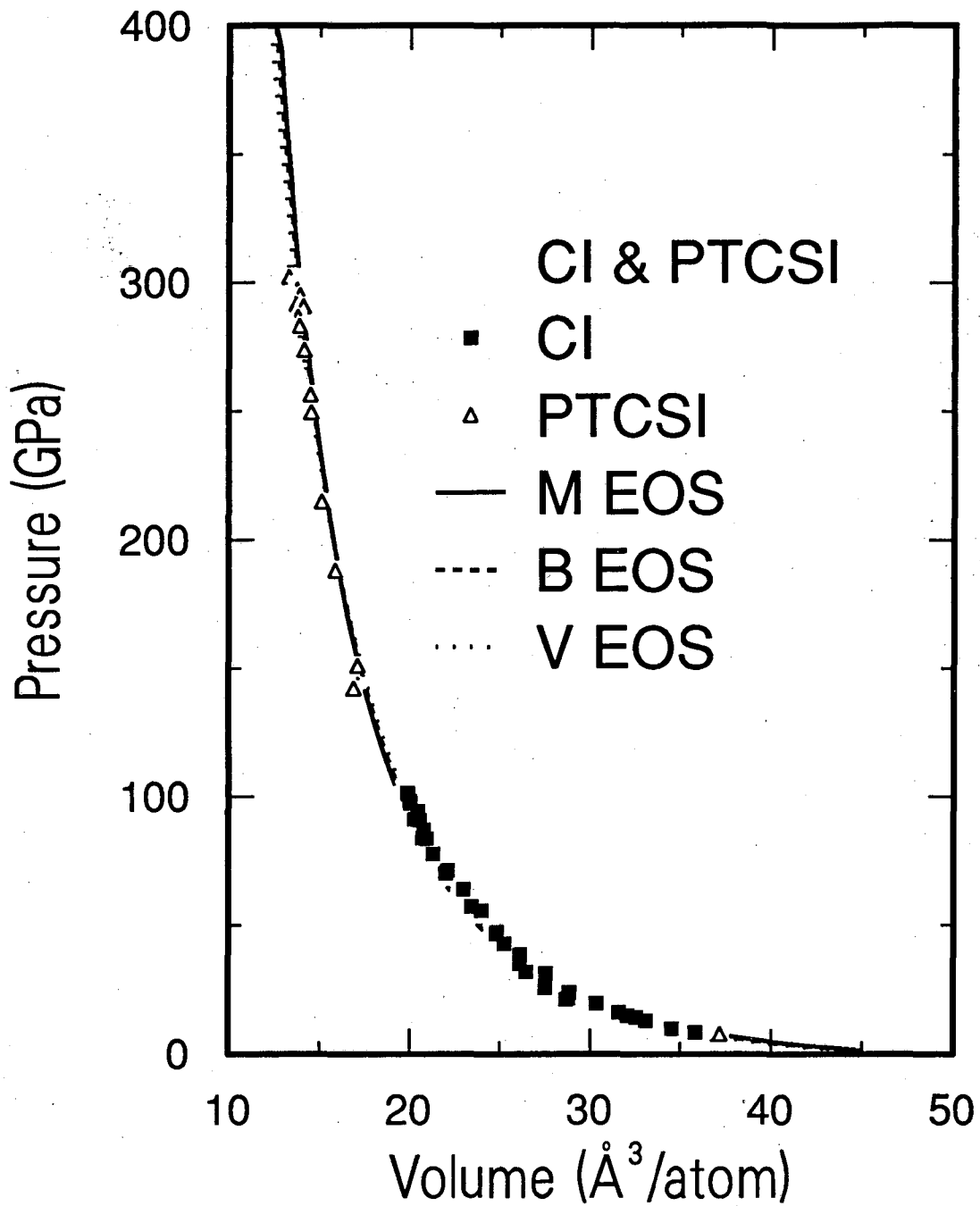


Figure 5.14: Comparison of weighted least square fits to three different EOSes with our experimental data to 300 GPa. The residues in these three fits are rather different. Of the three EOSes considered here, the Vinet EOS is preferred.

A good equation of state formulation should also have good quality in terms of extrapolation. In other words, by using parameters obtained from fitting to lower pressure data, one should be able to predict the equation of state at higher pressures. As shown in Figure 5.15, where we compared the ultra high pressure data with the EOS obtained from lower pressure studies. The Vinet EOS extrapolates the closest to the experimental value.

We can look at this point from a slightly different point of view. As we described earlier, the parameters in the EOSes are related only to the zero pressure bulk modulus and its pressure derivative at zero pressure. These values can be measured using other method (*i.e.* Ultrasonics). For CsI, they were measured by Barsch and Chang [87] and are listed in Table 5.8 for comparison. Clearly, Vinet EOS again shows the best agreement. To further illustrate this idea, we plot in Figure 5.16 the calculated pressures as a function of volume using the ultrasonic values for the zero pressure parameters in the different EOSes. The agreement between the calculated one using the Vinet EOS and experimental data is rather remarkable. On the other hand, the pressures calculated using the Birch's finite strain theory that included one more term in the expansion (Eq. 5.2) (Labeled B-EOS 2 in the figure) with the ultrasonic parameters did not show reasonable agreement. This probably shows that the ultrasonic value for B_0'' is in error.

It should be pointed out that above discussion ignores the effects of phase transitions. This can be justified by the fact that these phase transitions involve only structures which are related to each other by continuous distortion and there is no observable discontinuity in the pressure volume relation. Although a discontinuity in compressibility does exist, the effect on the pressure volume relation is probably rather small.

In conclusion, by using our compression data of CsI, we are able to compare the quality of the three most used EOSes. The Vinet EOS shows the best properties in terms of description of compression data over a large compression range, the quality

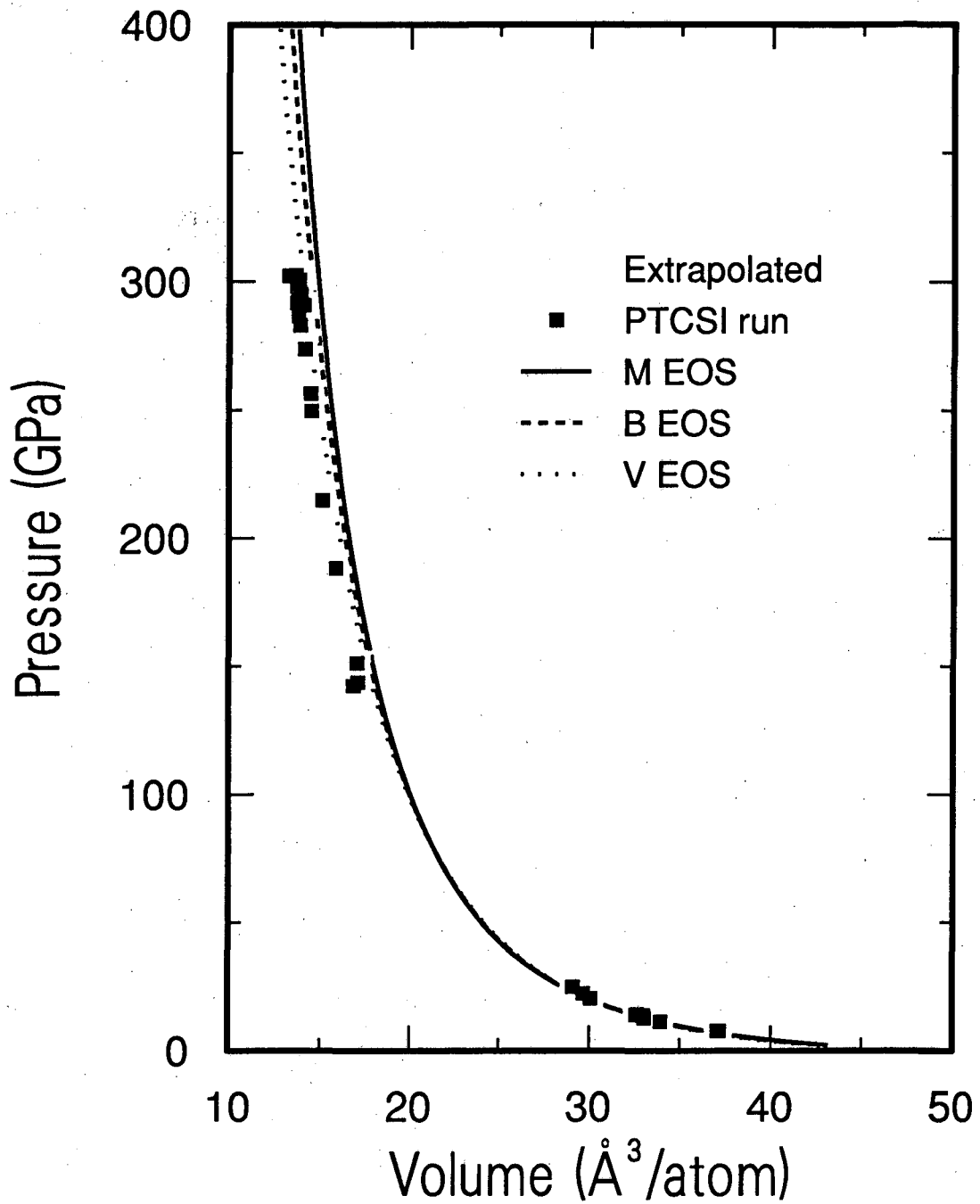


Figure 5.15: The extrapolation properties of the three EOSes are compared with our experimental data. The calculated EOSes were based on parameters we obtained from the run with 100 GPa maximum pressure. The Vinet EOS is seen to extrapolate the closest to the experimental data to 300 GPa.

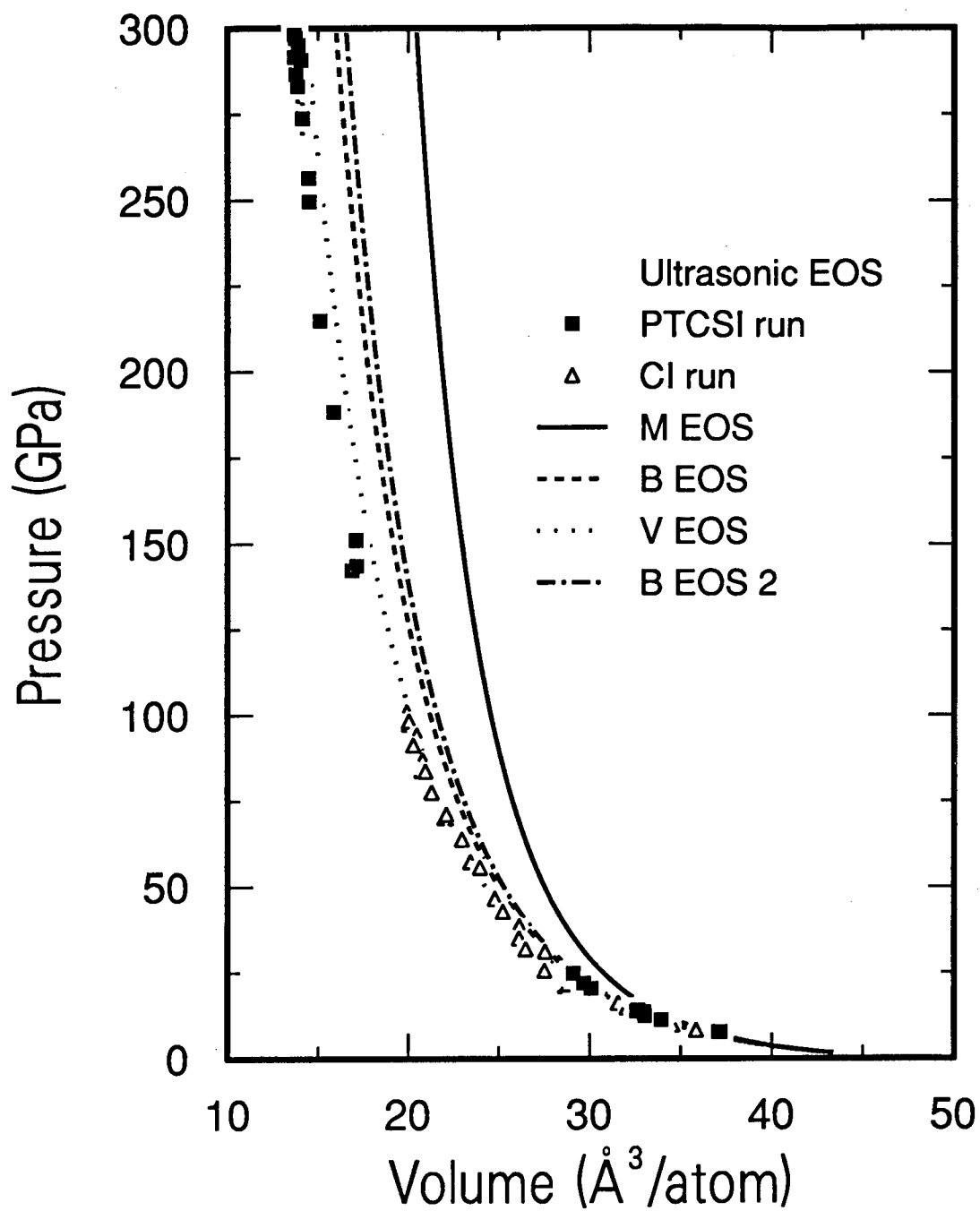


Figure 5.16: The calculated equations of state of CsI with the values of the bulk modulus and its pressure derivatives obtained from the ultrasonic study of Barsch and Chang[87]. Our experimental data is also shown for comparison.

of extrapolation, and in terms of the agreement between the fitted parameters and values derived from ultrasonic studies.

5.5.3 Comparison with previous studies

Previous equation of state studies on CsI are in three main categories. There are numerous static high pressure compression studies covering pressures up to 90 GPa. Several first principle theoretical calculations using local density functional theory are also available. Dynamic compression studies using shock wave methods have also been performed on CsI to very high pressures. It is then the purpose of this section to present a comparison between the current experimental data and the results from previous studies.

The comparison of the present data with previous static data has been made in section 5.5.1 earlier. The major difference between the current data and the previous static data is the reassignment of structures. While previous studies assumed the B2 structure is maintained up to 40 GPa, we assumed a slight distortion from this cubic phase started at a pressure as low as 15 GPa in the non-hydrostatic compression studies based on the broadening and then splitting of the diffraction peaks. For pressures between 40 GPa and 100 GPa, previous studies assigned a tetragonal distortion for pressures between 40 GPa and 65 GPa and an orthorhombic distortion for pressures above that, in the current study, we showed that the phase transition above 40 GPa is a continuous evolution within an orthorhombic unit cell which is twice as large as the original cubic B2 unit cell. In fact, this evolution may have been continuous even to the lower pressure region. The analysis of some of the earlier data in our new structure led to good agreement with our current results. All previous static compression data are now well understood and in good mutual agreement.

All static compression results presented here and most other previous studies were carried out at room temperature. In order to make comparison with theoretical

calculations which are normally for static lattices, one needs to estimate the thermal and zero point contributions. For low temperatures where there is no significant electronic excitations, these contributions are mainly from the lattice vibrations. Within the quasi-harmonic approximation, we can write the free energy as

$$F = U + \frac{1}{2} \sum_i h\nu_i + kT \sum_i \ln(1 - e^{-\frac{h\nu_i}{kT}})$$

where U is the energy for the static lattice, ν_i are the phonon frequencies, and the summation is taken over all possible phonon modes. The second term is the zero point energy and temperature independent which arises from pure quantum effects. The pressure at a given volume and temperature is given by

$$P = -\frac{dU}{dV} - \sum_i \left(\frac{1}{2} + \frac{1}{e^{\frac{h\nu_i}{kT}} - 1} \right) h \frac{\partial \nu_i}{\partial V}$$

if we introduce the Grüneisen parameters $\gamma_i = -\frac{\partial \ln \nu_i}{\partial \ln V}$ and assume they have the same value for all phonon modes, we have

$$P = -\frac{dU}{dV} + \frac{\gamma}{V} \sum_i \left(\frac{1}{2} + \frac{1}{e^{\frac{h\nu_i}{kT}} - 1} \right) h\nu_i$$

i.e., the zero point and thermal contribution can be written as

$$P_{ZP} + P_T = \frac{\gamma}{V} (E_{ZP} + E_T).$$

Where E_{ZP} and E_T are the zero point and thermal energy respectively. Using Debye model, we can easily obtain the energies per atom

$$E_{ZP} = \frac{9}{8} k\Theta_D,$$

and

$$E_T = 3kTD(x)$$

where Θ_D is the Debye temperature with $k\Theta_D = h\nu_D$ and ν_D is the cut off phonon frequency, $x = \frac{h\nu}{k\Theta_D}$ and $D(x) = \frac{3}{x^3} \int_0^x \frac{x'^3}{e^{x'} - 1} dx'$ is the Debye integral. Remembering our assumption that γ is a constant for all modes, so in particular

$$\gamma = -\frac{\partial \ln \nu_D}{\partial \ln V} = -\frac{\partial \ln \Theta_D}{\partial \ln V}.$$

Now we can see, the zero point pressure and thermal pressure can be represented entirely in terms of $\Theta_D(V)$.

In order to find $\Theta_D(V)$, we recall that if the interaction between the atoms in the crystal can be represented by the summation of a Coulomb term and a short range central repulsive interaction which only extend to the first nearest neighbors, similar to the derivation of the Blackman's sum rule[88], we can obtain the mean square frequency

$$\langle \nu^2 \rangle = \frac{9}{24\pi^2} \left(\frac{1}{M_+} + \frac{1}{M_-} \right) \frac{1}{r^2} \left[B - \frac{1}{3}P \right] \quad (5.5)$$

where M_+, M_- are the masses of the cation and anion, r is the nearest neighbor distance, B, P are the bulk modulus and pressure at a given volume. Therefore,

$$\Theta_D = \frac{h}{k} \left(\frac{5}{3} \langle \nu^2 \rangle \right)^{\frac{1}{2}} \quad (5.6)$$

and

$$\gamma = -\frac{1}{6} - \frac{1}{2} \frac{V \frac{\partial B}{\partial V} + \frac{4}{3}B}{B - \frac{4}{3}P} \quad (5.7)$$

With these relations, it is a simple matter to estimate the zero point and thermal pressures. Of course, the experimental equation of state already contain these effects. However, if the contribution from the zero point and thermal effects at room temperature is small, we expect little error will be introduced in using the room temperature EOS in the evaluation of the these quantities. This way we have calculated Θ_D, γ and $P_{ZP} + P_T$ as a function of pressure, the result² is shown in Figure 5.17 and Figure 5.18. As one can see, for temperatures below room temperature, the pressure due to zero point motion and thermal effect is indeed rather small. These values are in close agreement with the result of Aidun *et al.*[68] who used a similar approach but started with their first principle calculations.

Now we can compare the static compression results with those from first principle calculations. Figure 5.19 present the calculated equations of state from the

²In calculating γ , we have observed a strong dependency on the equation of state formulation used because the denominator. Here we neglected the term containing P in the calculation presented here. However, this does not effect our main conclusion here.

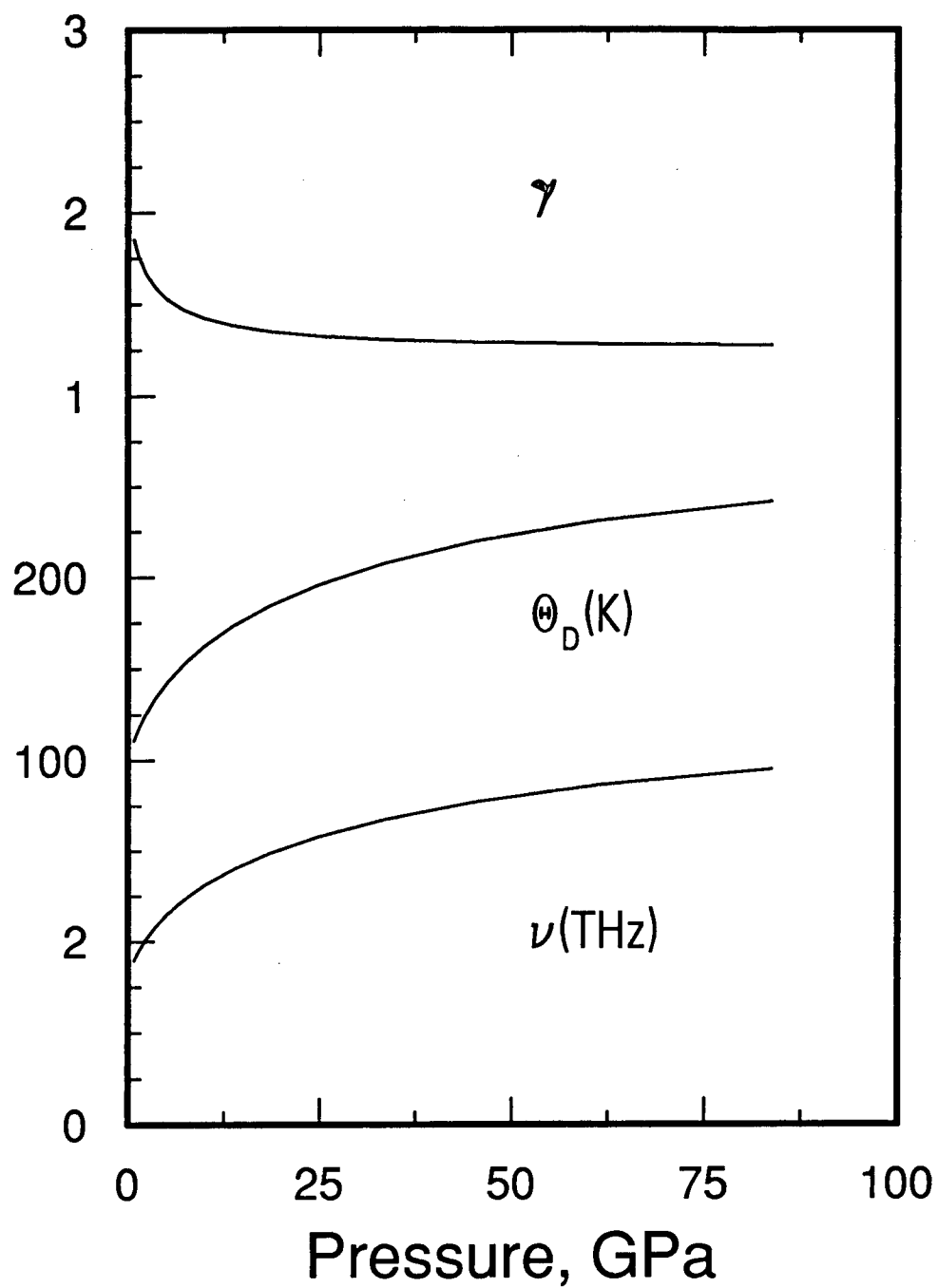


Figure 5.17: The mean square root frequency $\sqrt{\langle \nu^2 \rangle}$, Debye temperature Θ_D , and Grüneisen parameter γ as functions of pressure.

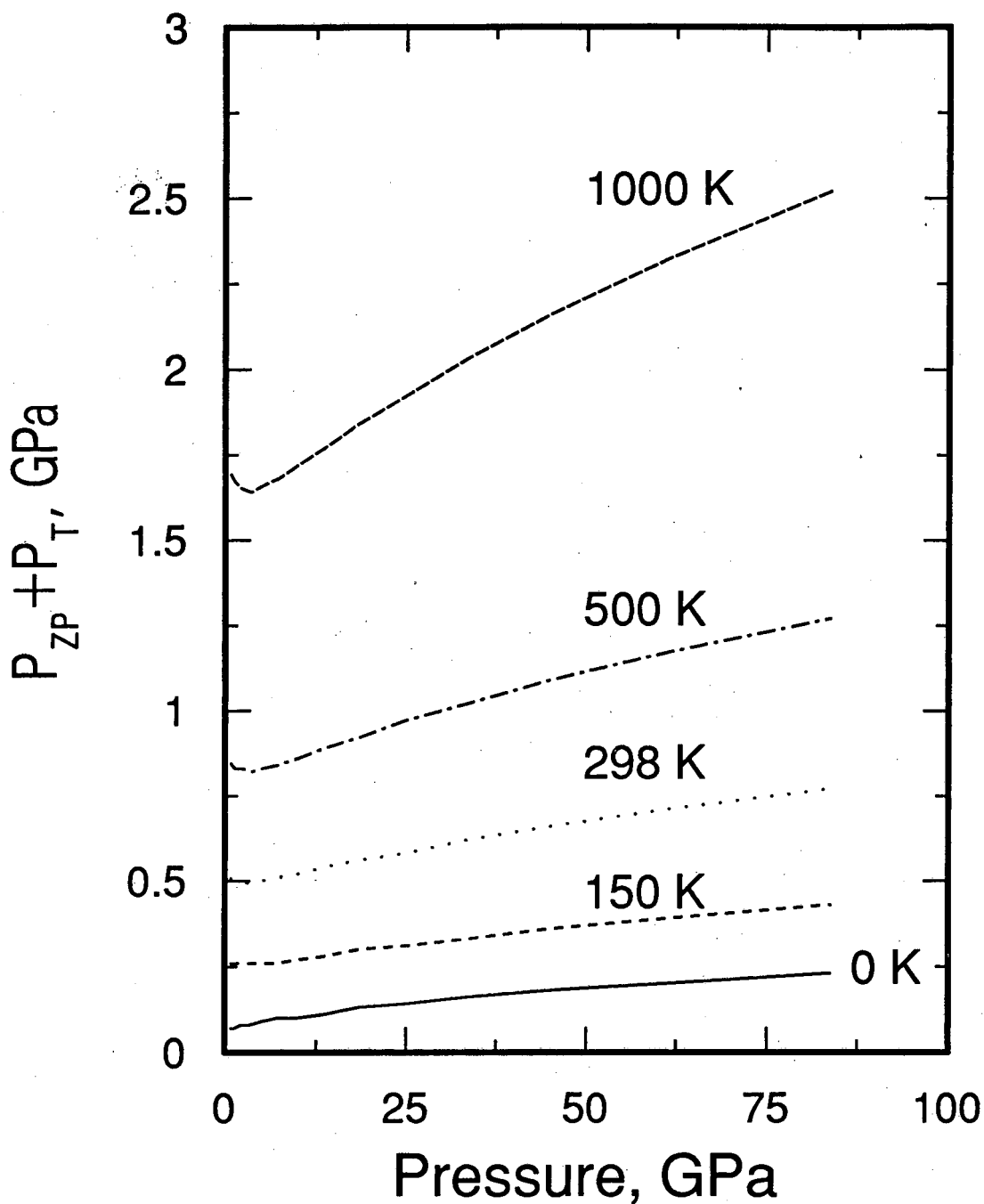


Figure 5.18: The calculated zero point pressure plus thermal pressure as a function of static pressure for several temperatures as calculated using a simple model combining the quasi-harmonic approximation and Debye approximation. For relatively high pressures (> 10 GPa) and low temperature (< 500 K), the relative magnitudes are very small.

non relativistic augmented-plane-wave (APW) studies of Aidun *et al.*[68], and the linear-muffin-tin-orbital (LMTO) with and without relativistic corrections of Satpathy *et al.*[70], along with our experimental isotherm. In general, the agreement among all of these is quite good. In detail, the LMTO R result shows relatively large deviation in the relatively low pressure range. This is clearly reflected in the calculated equilibrium volume V_0 as well. The reason for this large deviation is not well understood. The experimental isotherm we plotted is the non-hydrostatic equation of state. The quasi-hydrostatic equation of state data overlapped with the APW results almost exactly as can be seen from Fig. 5.11. This agreement may be fortuitous and does not reflect the actual accuracy in the calculations. The LMTO calculations used the previous assigned tetragonal distorted structure for pressures higher than 40 GPa, but the effect of this on the equation of state is rather minimal. The same situation is probably true for our new structure.

No first principle theoretical calculation has been performed on the new structure proposed here yet. It would be interesting to see whether such a calculation can successfully explain the current results. As we shall see later, a simple ionic pair potential model can successfully model the phase transition sequence described here. However, the model is too crude to give an accurate equation of state and the energetics.

For comparison with shock wave data, not only the thermal contribution from the lattice vibrations as discussed above becomes important, the electronic excitation is rather significant due to the high temperature reached during the shock processes and it has a non-negligible contribution especially in the high pressure region. A proper estimation requires the knowledge of the band gap as a function of pressure. This way one can calculate the total energy of the crystal as a function of pressure and temperature. Using conservation of energy and momentum, one can solve for the relation between the pressure and temperature. Such a calculation is rather involved, here, we use the result of such a calculation[68] in our comparison. We

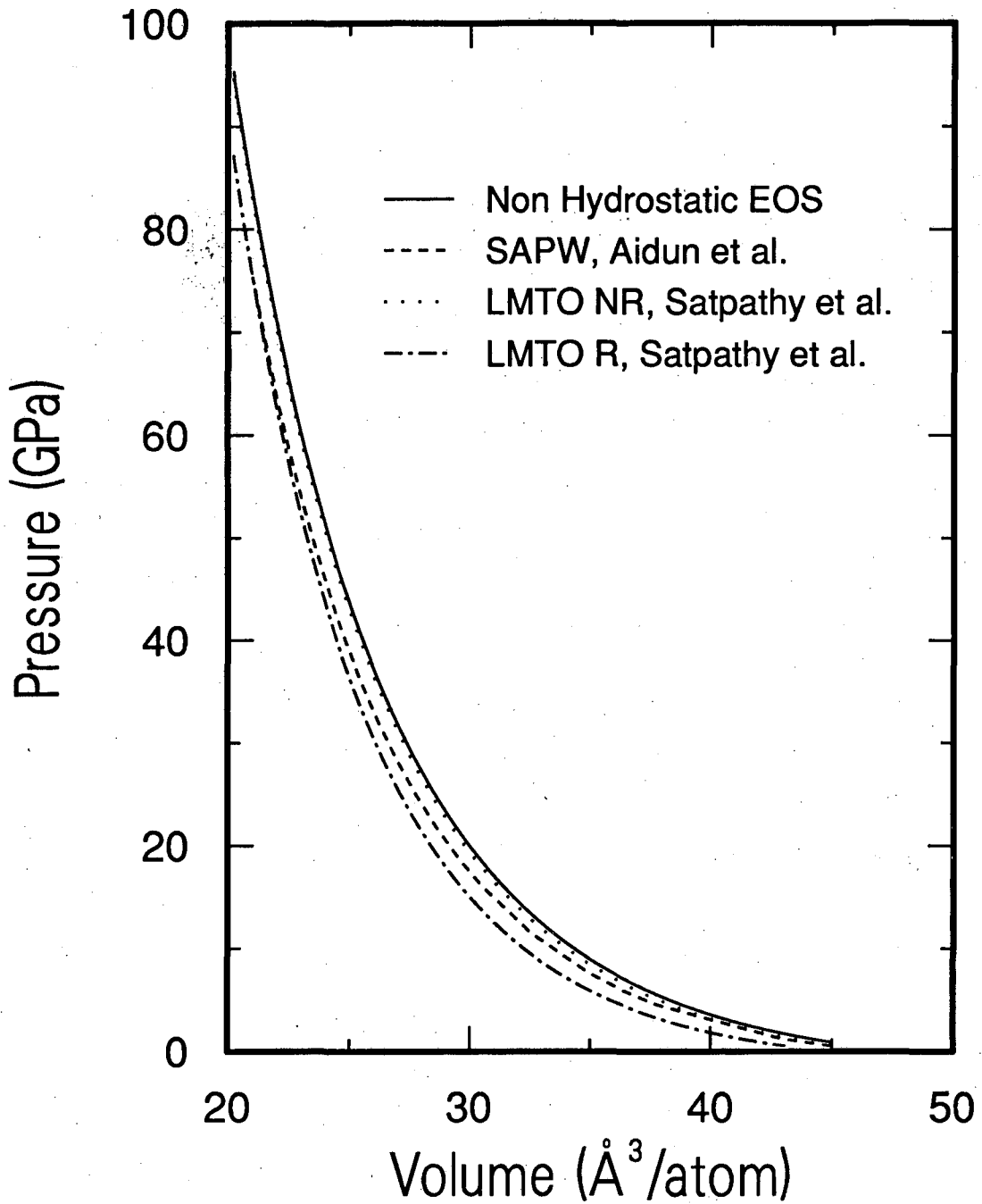


Figure 5.19: Comparison of current equation of state data with various first principle theoretical calculations. The theoretical calculations are the APW calculation of Aidun *et al.*[68] and LMTO calculations of Satpathy *et al.*[70] with and without relativistic corrections. The experiment data is taken from the non hydrostatic run. For hydrostatic compression, refer to Figure 5.11.

have seen, our quasi-hydrostatic compression data are in close agreement with the APW calculation[68], so no modification in their calculated Hugoniot is necessary. We therefore have plotted in Fig. 5.20 the shock wave data from various groups, our isotherm to 300 GPa, and two theoretical curves taken from Fig. 4 of reference [68]. One of the curves is based on the assumption that the electronic energy gap is a constant throughout the pressure range and the other assumes a linear relation between the energy gap and volume with band gap closes at $20 \text{ \AA}^3/\text{atom}$. Therefore the shaded region is where the actual Hugoniot curve is most likely located. The agreement with experimental data is good, but the accuracy of the data does not seem to render a preference for a particular model. The Hugoniot is calculated only up to a pressure of 160 GPa based on the static isotherm to about 80 GPa, the extrapolation to higher pressures using our isotherm to much high pressure is not likely to contradict the current conclusion. Although, it is known experimentally that for shock pressures higher than 25 GPa, CsI melts, the effect of this melting can not be readily seen in the current comparison.

The equation of state derived from the current study is in good agreement with previous static studies, but of course some of them must be reanalyzed in terms of our new structure, the various theoretical calculations, and the shock wave Hugoniot data. The previous controversies existed between these studies is seen to be a systematic error in the identification of the structure of CsI under high pressures. It is therefore not necessary to assume that CsI disproportionate under shock loading to understand the apparent differences that existed in the literature.

5.5.4 Implications to the insulator-metal transition

The metal-insulator transition in solids that consist of ions with closed shell electronic configurations occurs when the unoccupied conduction band start to overlap with the fully occupied valence band. Because the difficulty of measuring the band shape in a diamond anvil cell, a proper description of the process thus relies heavily

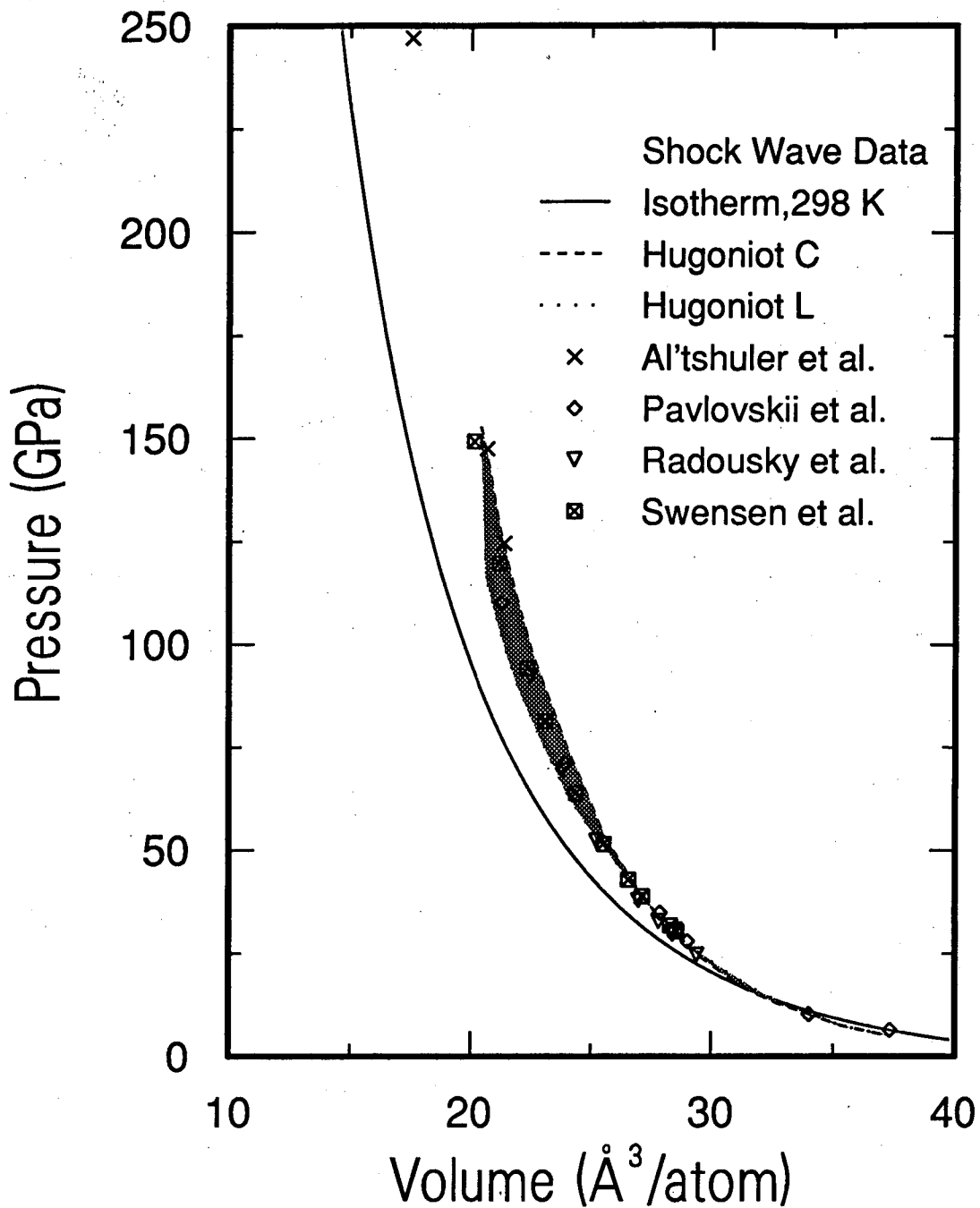


Figure 5.20: Comparison of shock wave Hugoniot data with the low temperature isotherms and calculated Hugoniot obtained from the current study. The current room temperature isotherm is significantly more compressible than the Hugoniot data. The calculated Hugoniot based on constant energy gap and a linear relation between the gap and unit cell volume shows rather good agreement with the experimental data.

on theoretical calculations. It is in this connection that the crystal structure studies under pressure is very important. Although the recent developments in theoretical methods and computation capabilities made possible calculations starting from only atomic properties, it is not yet possible to test large numbers of crystal models in ones calculation to find the most stable structures. Experimental study of crystal structures can be used as input to these theoretical calculations.

While fully quantum mechanical theoretical models will provide the ultimate information on a particular transition, other simpler models can help us to learn a great deal about the general features of the phase transitions. One such model is the dielectric model. It was first used by K. F. Herzfeld in 1927[89] to explain the origin of metallic behavior from atomic properties. We will use this model to link our equation of state studies to the observed insulator- metal transition observed in CsI at 110 GPa and the phase transition we have observed that involved the change of the crystal structure in the following discussion.

The dielectric model is based on a mostly classical electrostatics argument. The polarizability α of an atom or ion is defined in terms of the local electric field at the atom or ion:

$$p = \alpha E_{loc}$$

where p is the dipole moment. The use of atomic or ionic polarizabilities depends on the actual state that the atom is in. For brevity, we will not carry both the words atom and ion in the following discussion, it is understood that the word atom should refer to the appropriate state. The polarization of an assembly of atoms can be expressed approximately as a summation of the dipole moments from all of the atoms:

$$P = \sum_j N_j p_j = \sum_j N_j \alpha_j E_{loc}(j),$$

where N_j is the number density and α_j is the polarizability of atom j , and $E_{loc}(j)$ is the local field at atom site j .

In a dielectric material, the local field is different from the applied external field

by a depolarization field which arises because of the polarization of atoms nearby. If the medium is isotropic, the depolarization field is given by [18]

$$E_{dep} = \frac{1}{3\epsilon_0}P.$$

The polarization of an assembly of atom due to an external field E can be written as

$$P = \sum N_j \alpha_j (E + \frac{1}{3\epsilon_0}P)$$

and the susceptibility

$$\chi = \frac{P}{E} = \frac{\sum N_j \alpha_j}{1 - \frac{1}{3\epsilon_0} \sum N_j \alpha_j} \quad (5.8)$$

The dielectric constant is defined as $\epsilon = 1 + \chi$, so by rearrange Eq. (5.8), we can obtain the famous Clausius-Massotti relation:

$$\frac{\epsilon - 1}{\epsilon + 2} = \frac{1}{3\epsilon_0} \sum N_j \alpha_j \quad (5.9)$$

This gives the relationship between the dielectric constants of materials to the atomic polarizabilities.

The total polarizability of an atom (or ion, molecule, whichever is appropriate) may usually be separated into three parts (electronic, ionic and dipolar) in the static to optical frequency region as shown in Fig. 5.21. The electronic polarizability is pertinent to each atom or ion, which comes from the distortion of the electronic charge around an nucleus. The ionic contribution comes from the relative displacement of positive and negative ions which is important in all ionic materials. The dipolar contribution comes from molecule with a permanent electric dipole moment that can change its orientation under the influence of an electric field.

Classical dispersion theory based on simple harmonic oscillators can give both the electronic and ionic polarizability. For a particle with mass m and charge e in a harmonic well with force constant $\beta = m\omega_0^2$, the equation of motion under an

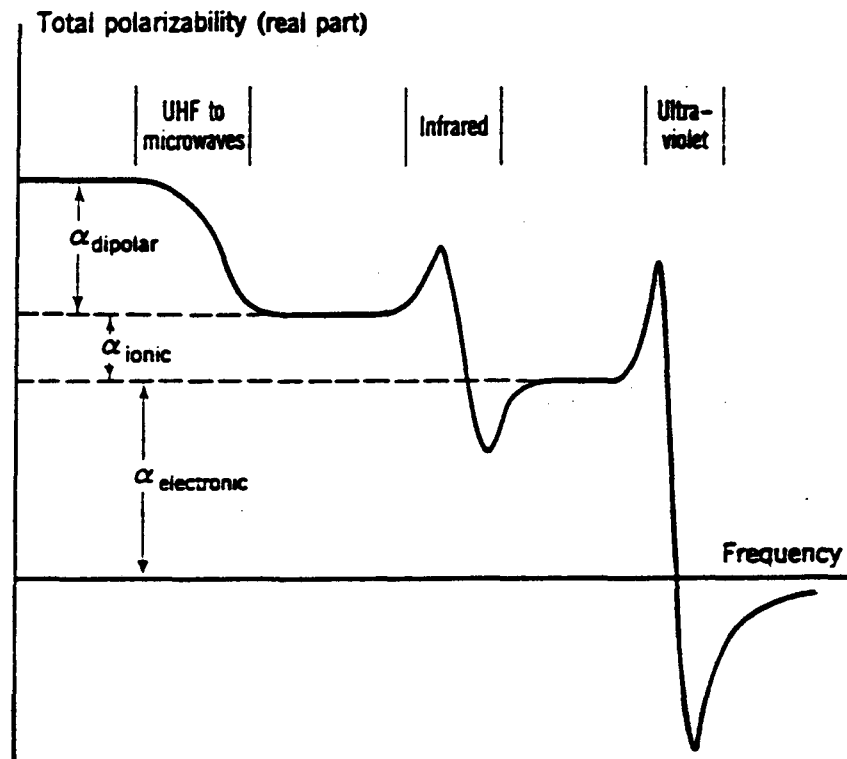


Figure 5.21: The polarizability as a function of frequency of excitation for a typical dielectrics. Figure adopted from Kittel[41], page 411.

external field $E_{loc} \sin(\omega t)$ is

$$m \frac{d^2 x}{dt^2} + m\omega_0^2 x = -eE_{loc} \sin(\omega t),$$

the dipole moment due to the electric field has the amplitude

$$p = \frac{e^2 E_{loc}}{m(\omega_0^2 - \omega^2)},$$

thus

$$\alpha = \frac{e^2/m}{(\omega_0^2 - \omega^2)}.$$

In the situation where both the electronic and ionic polarizabilities are important, one needs to sum over both contributions. In an insulator or semiconductor, the electronic polarizability can be described approximately by the above model with a characteristic frequency $\omega_0 = E_g/\hbar$, where E_g is the energy gap.

In Equation (5.8), if the number density is so high that the denominator is zero, then the susceptibility is infinite. This is called a *polarization catastrophe*. At the critical concentration, the excitation frequency is reduced to zero[89]. If this happens for electronic excitations, it means that the solid is metallic. The equation of state of a given material can be used to predict the pressure at which it will transform into a metal in this connection. For CsI, the number densities of both ions at ambient conditions are $N = 1.05 \times 10^{22}/\text{cm}^3$, the electronic polarizabilities for Cs^+ and I^- can be found on page 411 of Kittel[41], we obtain

$$\frac{1}{3\epsilon_0} \sum N_j \alpha_j = 0.39.$$

Under compression, the number density increases, it is clear that we need a $V/V_0 = 0.39$ in order to reach the insulator-metal transition.

Another estimate is possible if we use the electronic polarizabilities of ions as determined when they are in the crystalline form. They are related to the index of reflection n of solid CsI under ambient conditions by the Clausius- Mossotti relation (Eq. 5.9) and $\epsilon = n^2$. Since $n = 1.7876$ at $\lambda = 5893\text{\AA}$ [90], we obtain

$$\frac{1}{3\epsilon_0} \sum N_j \alpha_j = \frac{\epsilon - 1}{\epsilon + 2} = 0.42.$$

From our experimental equation of state for CsI, we find the two volume fractions correspond to pressures of 126 GPa and 98 GPa respectively, which is close to the experimentally determined value of 110 GPa. The estimate using the free ion polarizability gives higher pressure, as illustrated in Fig. 5.22.

The difference between them can be attributed to the effect of crystal field. So the value obtained from the refractive index should represent a better estimate of the metallization transition fractional volume.

In view of the good agreement between the experimental value with those estimated based on the simple Herzfeld model, it is of interest to carry out such calculations for all alkali halides. Table 5.10 lists the optical reflective indices for all twenty compounds. By using relation (Eq. 5.9), we can calculate the fractional volumes at which the insulator-metal transition should occur. They are presented in Table 5.11. We have also used the values of bulk moduli listed in Table 5.1 and assumed $B' = 5.7$ to calculate the pressures at the corresponding volumes. It should be pointed out that most of those compounds that exist in the B1 structure at ambient conditions are expected (some of them have already been shown) to go through phase transitions before these volume fractions are reached. In general, pressure induced phase transitions will involve a decrease in the volume if there is any, so the calculated pressures represent upper estimates. Of course, the assumption of the validity of the Vinet EOS and $B' = 5.7$ should be examined case by case, but the current assumption should represent a good estimate. The result is presented in Table 5.12. It is seen, most of these transitions now fall in the range of current experimental capabilities. So a systematic study should be possible.

5.5.5 Comparison of EOS of CsI with that of Xe and BaTe

The charge distributions around each ion in the isoelectronic sequence Xe, CsI, and BaTe should be rather similar, therefore the repulsive interactions arising from charge overlaps should also be similar. The major difference between these com-

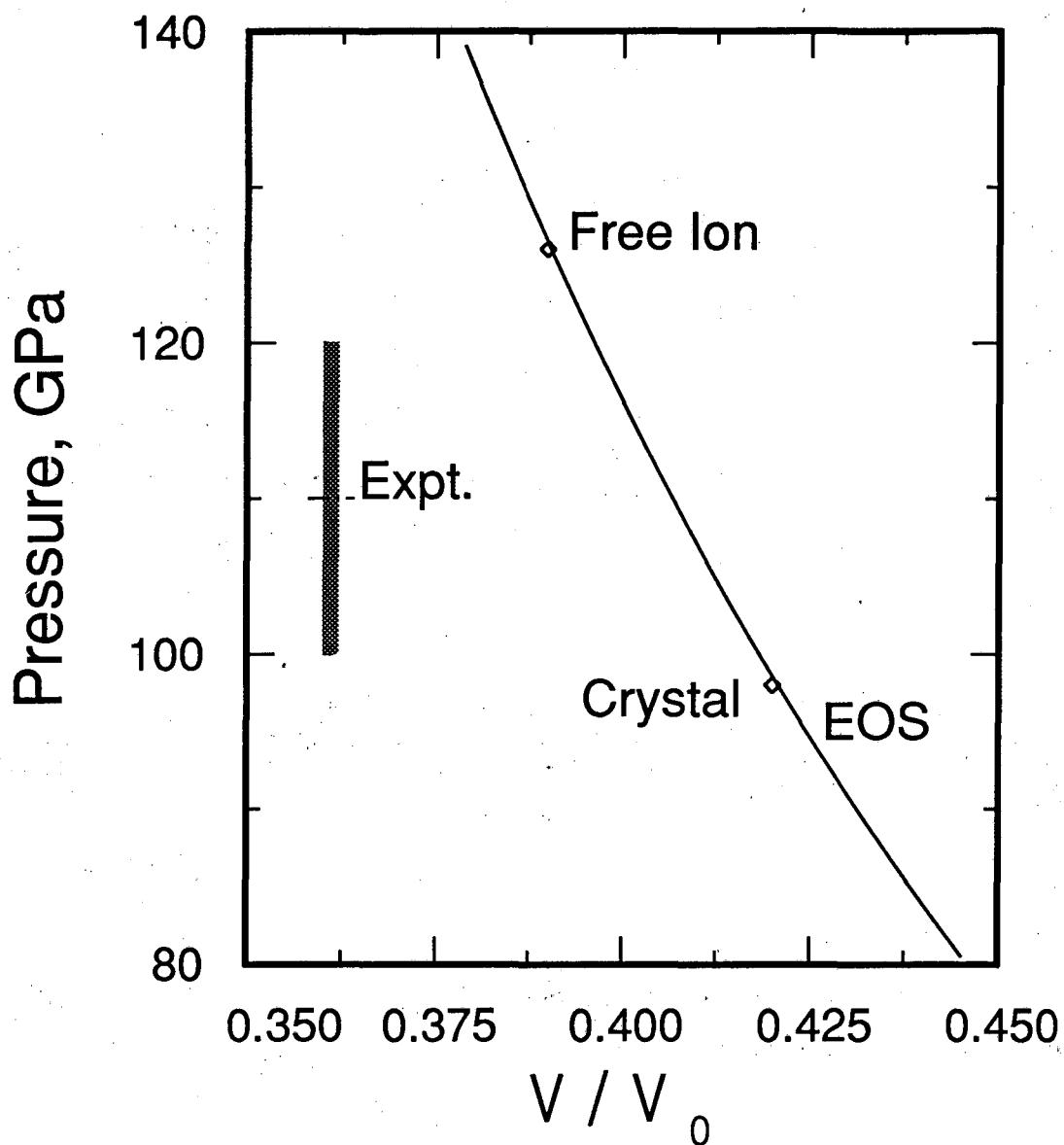


Figure 5.22: A comparison of metalization pressure of CsI at room temperature based on the current equation of state and the Herzfeld criteria with the experimentally observed value. The lower and upper bounds in pressure of the shaded area represent the experimental error estimates. Two estimates based on free ion polarizability and crystal polarizability closely bracket the experimentally measured metallization pressure.

Table 5.10: Indices of refraction for alkali halides*

	Li	Na	K	Rb	Cs
F	1.392	1.336	1.363	1.398	1.478
Cl	1.662	1.544	1.49	1.493	1.642
Br	1.784	1.641	1.559	1.553	1.698
I	1.955	1.775	1.677	1.647	1.788

*from reference [90].

Table 5.11: Fractional volume at which insulator-metal transition is expected for the alkali halides

	Li	Na	K	Rb	Cs
F	0.238	0.207	0.222	0.241	0.283
Cl	0.370	0.316	0.289	0.291	0.361
Br	0.421	0.361	0.323	0.320	0.386
I	0.485	0.418	0.377	0.363	0.423

Table 5.12: The approximate pressures (in GPa) corresponding to the volume fraction in the previous table

	Li	Na	K	Rb	Cs
F	2906	2886	1582	1095	
Cl	357	470	441	389	236
Br	186	259	271	244	166
I	81	122	133	135	92

*Assume the Vinet equation of state with $B' = 5.7$ is adequate and no phase transition before the metallization transition.

Table 5.13: The parameters used to calculate the equations of state of Xe, CsI, and BaTe

	EOS	B(GPa)	B'	reference
Xe	Birch	10.17	4.03	[44]
CsI	Birch	12.45	5.71	Present study
BaTe	Birch	27.5	4.6	[46]

pounds is the attractive force that bonds the atoms together. While the van de Waals force is responsible for the cohesion of solid Xe, much stronger Coulomb forces exist in the other two compounds. The room pressure equilibrium volumes per atom for these compounds decrease monotonically due to increases in the strength of the attractive force. The electronic structure also follows an interesting sequence with the fundamental gap decreasing as one traverses the sequence.

There are differences in the crystal structure at room pressure as well because the varying strengths of the attractive interaction. The van de Waals force is extremely weak and short ranged so a close packed fcc structure is found for Xe. For BaTe, the strong long range Coulomb interaction is responsible for the experimentally observed B1(rocksalt) structure. CsI, with a weaker Coulomb interaction, exists in the B2(CsCl) structure. Upon applying only a small pressure, BaTe transforms to the B2 structure which signifies a quick loss in the strength of Coulomb attraction.

As the pressure is further increased, one expects the role of the attractive force to be significantly reduced due to the rapid increase in the repulsive interaction. Under sufficiently high pressure, it is expected that the equations of state for all three compounds should be identical. Figure 5.23 shows a comparison of the three equations of state curves. Although for BaTe, only data with a limited pressure range is available, one had to resort to extrapolation to obtain the equation of state over the pressure range illustrated, the agreement at high pressures is indeed quite good. This validates the assumption that at high pressures, the repulsive force in these compounds are indeed very similar.

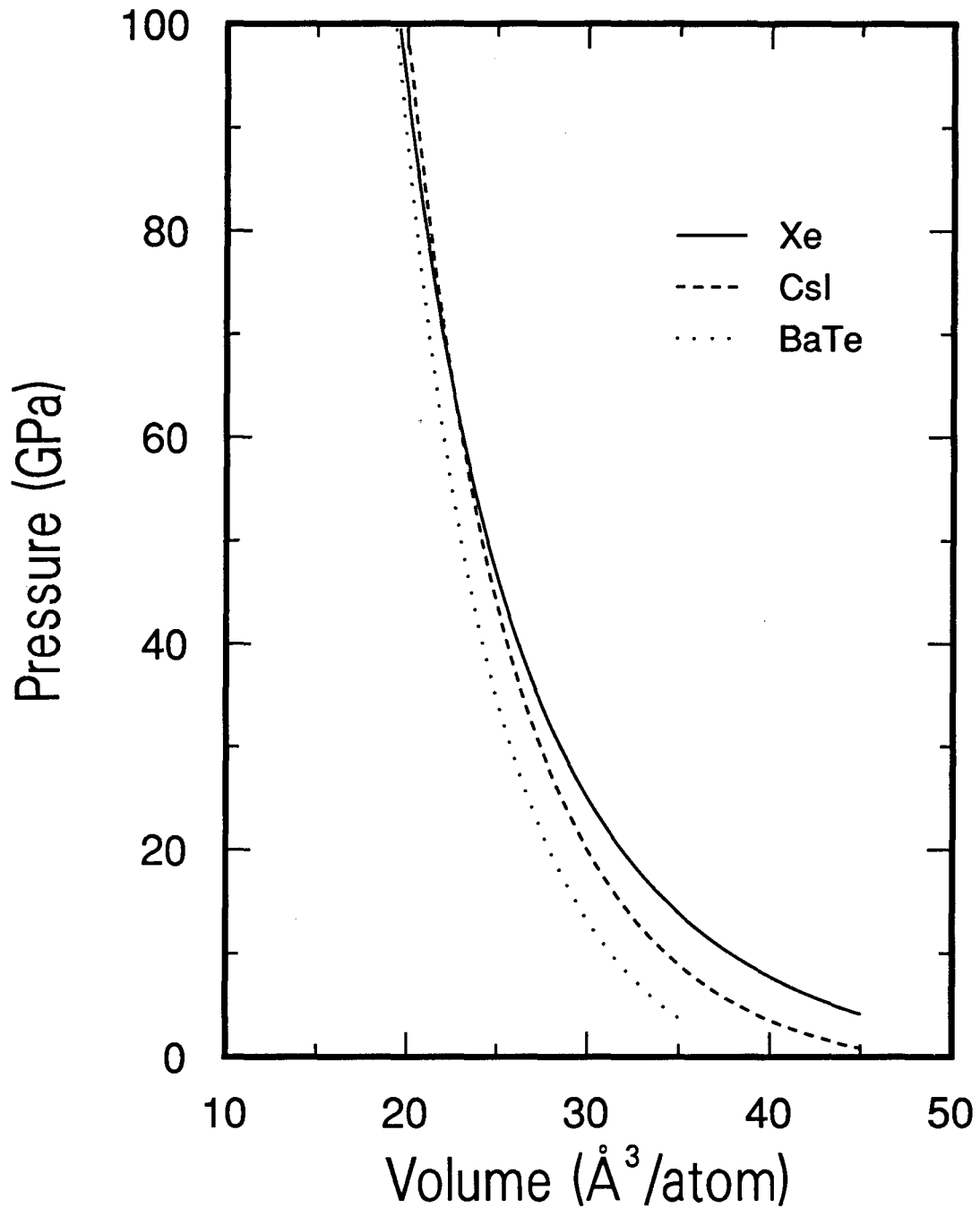


Figure 5.23: The equations of state of the isoelectronic compounds Xe, CsI, and BaTe. Only the EOS for the B2 phase of BaTe is plotted here and it was extrapolated to cover the whole pressure region. At low pressures, the volume per ion in CsI and BaTe are much smaller than that of Xe. As the pressure is increased, the EOSes approach each other, which indicates that the charge distributions around each ions are similar. The parameter for the curves are listed in Table 5.13.

The differences in volume at low pressures are mainly the result of the attractive interactions. An interesting result can be derived from some simple assumptions.

Assume the total energy for Xe as a function of volume per atom is given by a function of the form $U_0(v)$, then the total energy for CsI and BaTe, assuming the ions have charges $\pm Ze$, can be written approximately as (The difference in $U_0(v)$ for different crystal structures and the same pair potential is rather small in the present case and they are ignored)

$$U = U_c(v) + U_0(v),$$

where $U_c(v)$ is the Coulomb interaction energy. For the B2 structure, it can be shown

$$U_c(v) = -\frac{1}{2} \frac{\alpha}{(2v)^{1/3}} Z^2 e^2$$

where $\alpha = 2.03537$ is the Madelung constant for the B2 structure in terms of the cubic lattice constant a .

The pressure is obtained by taking the derivative with respect to v ,

$$P = -\frac{\partial U}{\partial v} = -\frac{1}{6} \frac{1}{2^{1/3}} \frac{\alpha Z^2 e^2}{v^{4/3}} + P_0(v) \quad (5.10)$$

where $P_0(v)$ is the equation of state for Xe. Here we assumed that the contribution from the term containing $\frac{\partial Z}{\partial v}$ can be neglected. Alternatively, if we normalize the pressure in units of the Coulomb pressure to obtain the normalized pressure,

$$P_{nc} = P \frac{6}{\alpha} \frac{2^{1/3}}{e^2} v^{4/3},$$

we obtain

$$P_{nc} = -Z^2 + P_{nc0}(v).$$

Now it is clear that if we form the differences of the EOSes for Xe, CsI, and BaTe, we should have approximately a constant for the region where equation (5.10) is valid. Using the available experimental EOSes (The parameters are listed in Table 5.13), we have plotted $P_{nc}(\text{CsI}) - P_{nc}(\text{Xe})$, $\frac{1}{4}(P_{nc}(\text{BaTe}) - P_{nc}(\text{Xe}))$ and $\frac{1}{2^2-1}(P_{nc}(\text{BaTe}) - P_{nc}(\text{CsI}))$ in Fig. 5.24, where the prefactors were calculated based

on formal ionic charges(1 for CsI, 2 for BaTe) so the result have the same data range. It is clear that for larger v , each of these differences are approximately a constant. From this we can derive that the actual charge transfer in CsI is approximately 0.65 electrons, rather than close to 1. This is surprising at first glance, however, it agrees well with the theoretical result of 0.6 obtained by Satpathy *et al.*[70]. We can also obtain the ionic charge for Ba⁺ and Te⁻ in BaTe in the B2 structure at an hypothetical volume of 45 Å³ per atom is approximately $\sqrt{0.35} \times 2 = 1.2$ electrons.

As the pressure is increased, the charge transfer is expected to decrease since more charge will be in the interstitial region instead of being close to the ions. So the constancy in Fig. 5.24 should not be expected to cover too large a volume range. In fact, qualitatively, the trend of smaller charge transfer is well reflected in Fig. 5.24.

The normalization of pressure with respect to the Coulomb pressure also illustrates that the relative importance of the Coulomb term decreases very quickly. Figure 5.25 shows the normalized pressure as a function of volume compression for CsI. At a volume fraction of 0.39, the Coulomb term is less than 10% of the repulsive term. This is in accord with our earlier observation that at high pressures, the three EOSes approach each other and also explains why no distortion from the hcp structure can be observed under ultra high pressure.

In summary, the comparison of EOSes for the isoelectronic compounds Xe, CsI, BaTe shows at high volume compressions, the differences among the EOSes diminish. This reflects a similar charge distribution exists in these compounds. The difference between the three EOSes at low pressures can be used to obtain the amount of charge transfer in the ionic compounds.

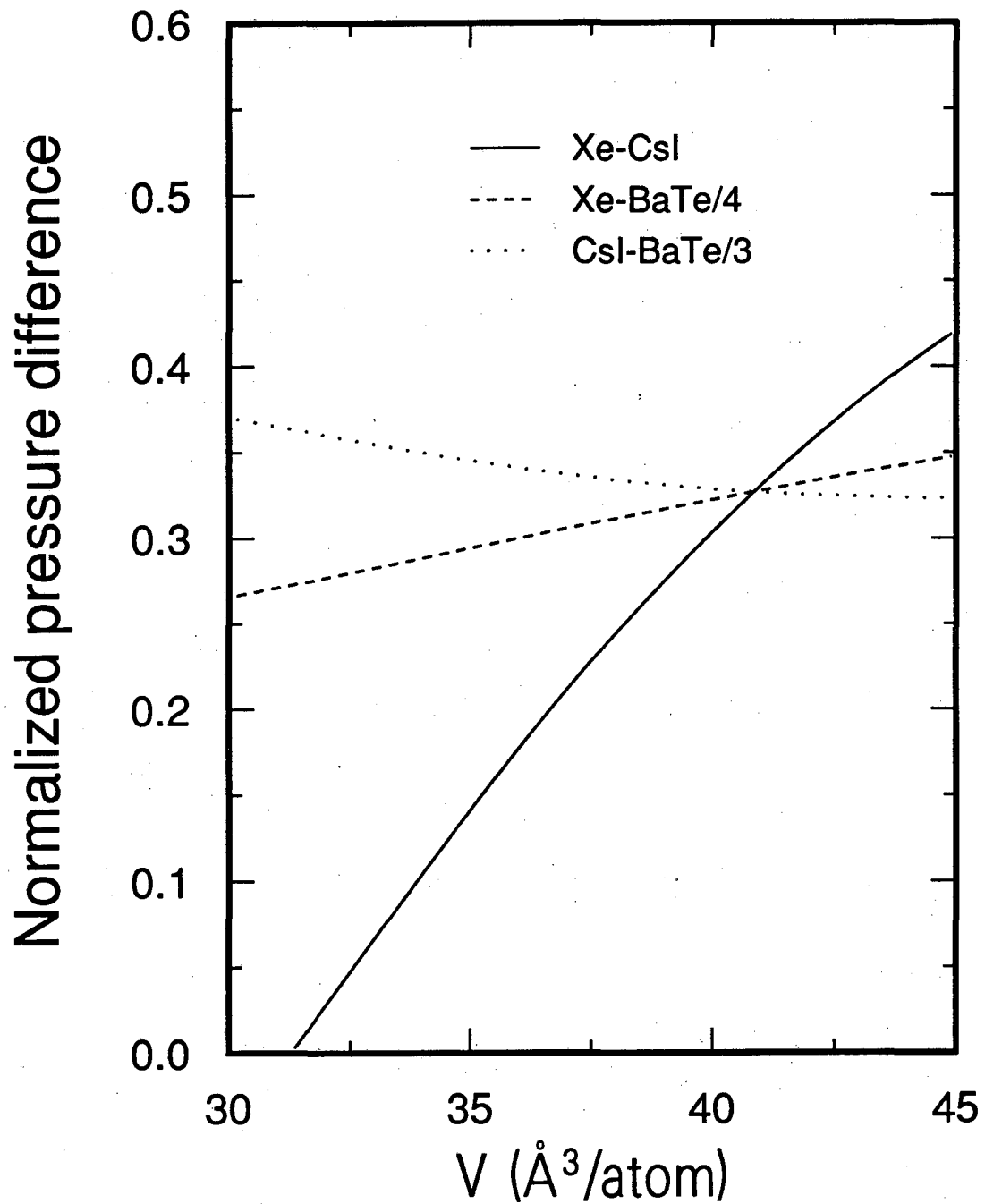


Figure 5.24: The differences between the normalized equations of state of Xe, CsI, and BaTe. These differences at large volume give approximate values to the ionic charges on the ions.

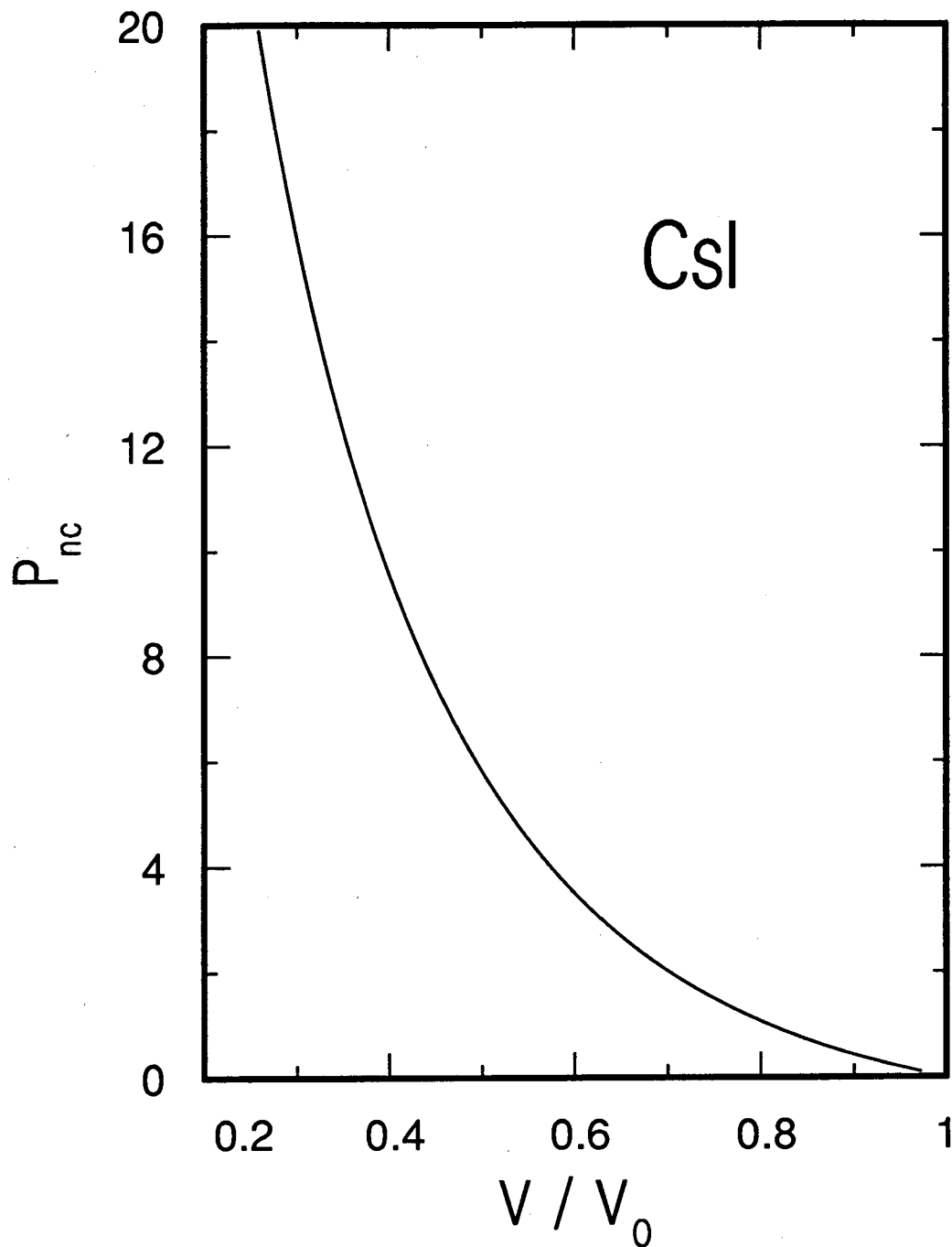


Figure 5.25: The relative magnitude of total pressure over the Coulomb pressure for CsI under different volume compressions.

5.6 An ionic model for phase transitions of CsI under pressure

In this section, we describe a simple ionic model for CsI under pressure using pair potentials. Despite its simplicity, we can describe rather successfully the phase transitions that have been observed experimentally. The lattice parameters calculated from such a model are in excellent agreement with the measured values.

5.6.1 The pair potential model

For ionic solids at low temperatures, the most important contribution to the cohesive energy of a crystal comes from the electrostatic Coulomb interaction between the ions and the short range repulsive force due to charge overlap. If we use the Born-Mayer form b/r^n to represent the short range interaction, the resultant pair potential can be written as

$$U_{ij} = Z_i Z_j e^2 / r_{ij} + b / r_{ij}^n \quad (5.11)$$

where Z_i, Z_j are the charges of the ions in the unit of electrons, r_{ij} is the distance between them. For AB type ionic solids, $|Z_i| = |Z_j| = Z$, the total energy of a lattice can be written as the summation of the long and short range potential over all ion pairs,

$$U = -Z^2 e^2 \alpha / a + \beta / a^n \quad (5.12)$$

where α, β refers to the Madelung constant and the constant that comes from summing over the short range interaction on a given lattice, where the units of distance have been scaled to a . Normally, the summation for the latter term only requires including the nearest and second nearest neighbor terms.

The equilibrium condition for the crystal with known structure and lattice constants at ambient pressure can be used to determine the value of b in the repulsive

term. When this is done for the CsCl structure and substituted back into Eq. (5.12), we obtain the following formula

$$U = -\frac{Z^2 e^2}{a_0} \alpha_0 \left[\frac{\alpha a_0}{\alpha_0 a} - \frac{1}{n} \frac{\beta}{\beta_0} \left(\frac{a_0}{a} \right)^n \right] \quad (5.13)$$

where a_0 is the lattice constant for the CsCl structure at zero pressure, α_0, α and β_0, β refers to the Madelung constants and the constants in the repulsive term for the zero pressure crystal structure and high pressure structure which may or may not be the same. a is chosen so that in the zero pressure phase, it coincides with a_0 .

Our model uses U as an approximation to the total energy of the crystal and neglects, the effects due to possible directional bonding, incomplete charge transfer, many body interactions, and lattice vibrations. We also implicitly neglected the difference of repulsive potentials between different type ion-pairs in the above discussion. This may break down for other ionic solids where the size of the cation is very different from that of the anion. The Madelung constants are evaluated by using Ewald's method[91]. Both the repulsive term and the Coulomb term can be calculated very accurately. The approximation of treating U as the total crystal energy, although it seems very crude, gives a rather good approximation of the cohesive energy of most alkali halides at ambient pressure. For example, the experimentally measured cohesive energy with respect to free ions for CsI is[92] 145.3 kcal/mole, while the calculated value varies from 135.5 to 146.8 kcal/mole for $n=13$ to ∞ . The applicability of this approximation to the high pressure regions relies on whether the pair potential approximation in Eq. (5.11) is still valid at the pressure of interest. We note that for CsI, which is the only alkali halide where the metallic transition has been observed[76], the pressure of the transition is around 120 GPa. So for pressures substantially lower than that, we expect that the charge distributions around each ion are not significantly distorted and the electrostatic interaction is not significantly screened. The effect of pressure on the repulsive term can be partly taken into account by choosing the appropriate parameter n . On the other extreme, for

Table 5.14: Different crystal structures that can be described within our orthorhombic unit cell

	hcp	orthorhombic	B2	tetragonal	CuAu I
b/a	$\sqrt{8/3}$	b/a	$\sqrt{2}$	b/a	1
c/a	$\sqrt{3}$	c/a	$\sqrt{2}$	$= b/a$	1
x	1/3	x	0	0	0

very high pressures, the contribution from the Coulomb interaction is much smaller than the repulsive term and this pair potential approximation may again be rather accurate provided a suitable repulsive potential is known.

In the present calculation, we have chosen $n = 13$ for the Born-Mayer term. As pointed out above, n should be chosen to best represent the interaction in the range of interest. We note that for $n = 13$, the bulk modulus calculated by differentiating Eq. 5.13 for CsI in the CsCl structure gives $B_0 = 14.3$ GPa, which is slightly larger than the ultrasonic value of 11.89 GPa[87] and the value of 12.4 GPa that we obtained by fitting the experimental equation of state data up to 100 GPa. It is well known that while the pair potential approximation well represents the cohesive energies, it does not give an accurate description of the equation of state in an extended pressure range. Since we are primarily interested in understanding the phase transitions that occur in CsI, the exact value will not change the mechanism very much. A different choice of n will give a different value for the volume fraction where the phase transitions occur(see the discussion below).

We have chosen a unit cell that is twice as large as the B2 unit cell, the relation between the two cells is depicted in Fig. 5.26. With this bigger unit cell, if we allow the axis ratio b/a , c/a , and the internal parameter x to vary from the starting values that correspond to the B2 structure, we can obtain a variety of crystal structures. Table 5.14 gives the corresponding parameters for the B2, the orthorhombic distortion, the hcp, the tetragonal distortion[60], and the CuAu I structure.

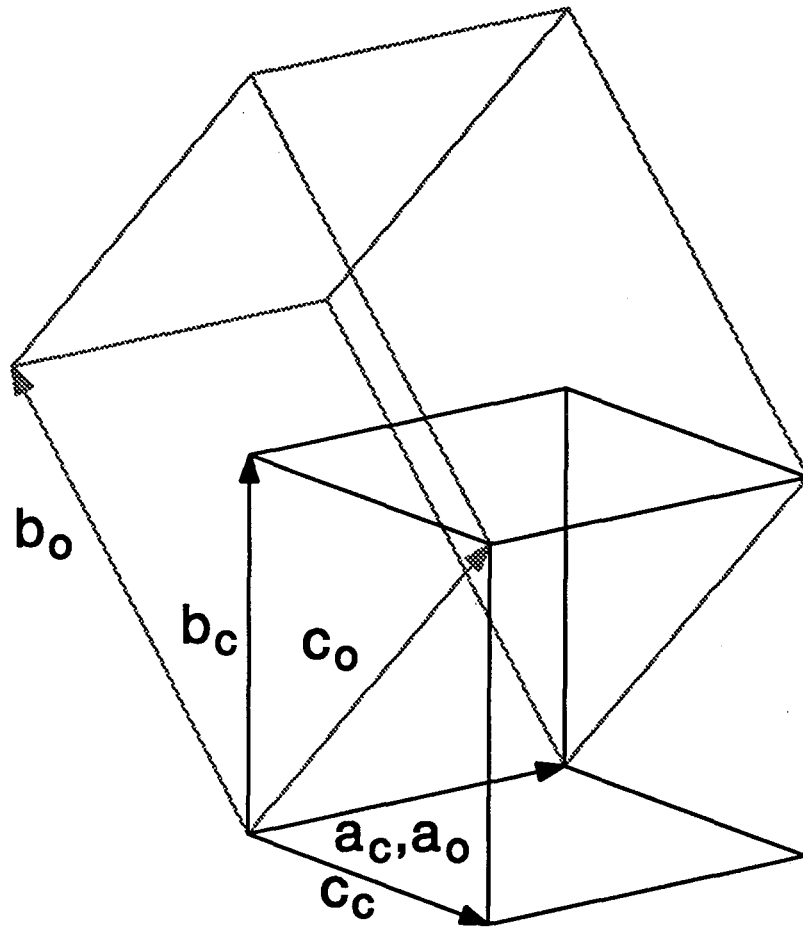


Figure 5.26: The relation between the general orthorhombic unit cell and the cubic B2 unit cell. The orthorhombic cell is twice as large as the B2 cell. As the axis ratio varies, the structure changes from a B2 structure to a hcp like structure. See text for details.

5.6.2 Calculated phase transitions

The minimization of energy for a given fractional volume V/V_0 gives the stable form of the crystal structure under that compression (strictly speaking, one should minimize the free energy under a given pressure, however, for continuous phase transitions, the two approaches should yield the same results). There may be more than one local minimum in the parameter space b/a , c/a , and x for certain fractional volumes. In this case, the energies corresponding to these local minima are calculated and compared with each other. For volume fractions greater than 0.53, the B2 structure is the most stable structure with respect to all possible distortions in this model. Below this volume fraction, the B2 structure becomes unstable with respect to two possible distortions. In one distortion, the ratio of b/a and c/a remain equal but decrease from the value of $\sqrt{2}$ that corresponds to the B2 structure, while the value of x remains unchanged. This is easily seen as the same distortion discussed by Vohra *et al.*[60] which is termed a tetragonal distortion in terms of the smaller cubic unit cell. Another distortion occurs at a slightly lower volume fraction (0.51) with changes in all the three parameters which correspond to an orthorhombic structure in terms of our larger unit cell. This distortion doubles the size of the original cubic unit cell and therefore can not be accommodated in the smaller cubic unit cell. The difference in energy between the tetragonal distortion and the orthorhombic distortion is very small (on the order of 0.06 eV/molecule when the distortions first appears and becomes increasingly smaller as the volume fraction is reduced). The small difference between the two energies suggests that other contribution which are not considered in the present model can easily reverse the order of stability between these two structures.

It is interesting to note that these two possible distortions lead to the fcc type and hcp type lattices under extreme compression, which agrees well with the intuitive picture that these ions behave very much like hard spheres with equal radii and close packing is expected. The difference in energy between these two lattices for

Lennard-Jones type interaction is known to be very small because each ion in the two structure has the same number of nearest neighbors.

In order to show more clearly the phase transition sequence, we have plotted the energy contours in the parameter space b/a and c/a for several different volume fractions in Fig. 5.27. The energy at each point has been minimized with respect to x . For $V/V_0 = 1$, the shapes of energy contours are very close to being circles centered at $b/a = c/a = \sqrt{2}$ which agrees well with the fact that the B2 structure is stable under ambient conditions. Although no other minimum in energy is found until a volume fraction of 0.53, as the volume fraction is reduced the energy contours become more like ellipses with their longer axes in the direction $b/a = c/a$, which indicates that any small contribution from an other source of interaction could easily drive the B2 structure to be unstable with respect to a tetragonal distortion. At even higher compression, the formation of two local minima is evident from Fig. 5.27(c). These correspond to the two possible distortions discussed above.

5.6.3 Comparison with the experimental results

Experimentally, under non-hydrostatic compressions, significant broadening of the diffraction peaks was observed at pressures as low as 15 GPa, which corresponds to a volume fraction of 0.63. At a slightly higher pressure, the broadened peak can be deconvoluted into two peaks, which suggests that a distortion from the cubic cell must be present. We assigned this distortion to have $b/a = c/a > \sqrt{2}$ in our larger unit cell. This distortion is tetragonal in nature in the smaller cubic unit cell but is different from the one discussed by Vohra *et al.*[60]. The existence of such a distortion facilitates a continuous transition from the B2 structure to the orthorhombic structure. The non-hydrostatic environment is probably the reason for the stabilization of such a structure. In our present model, this was not taken into account.

With this in mind, we have examined the transition path of CsI under high

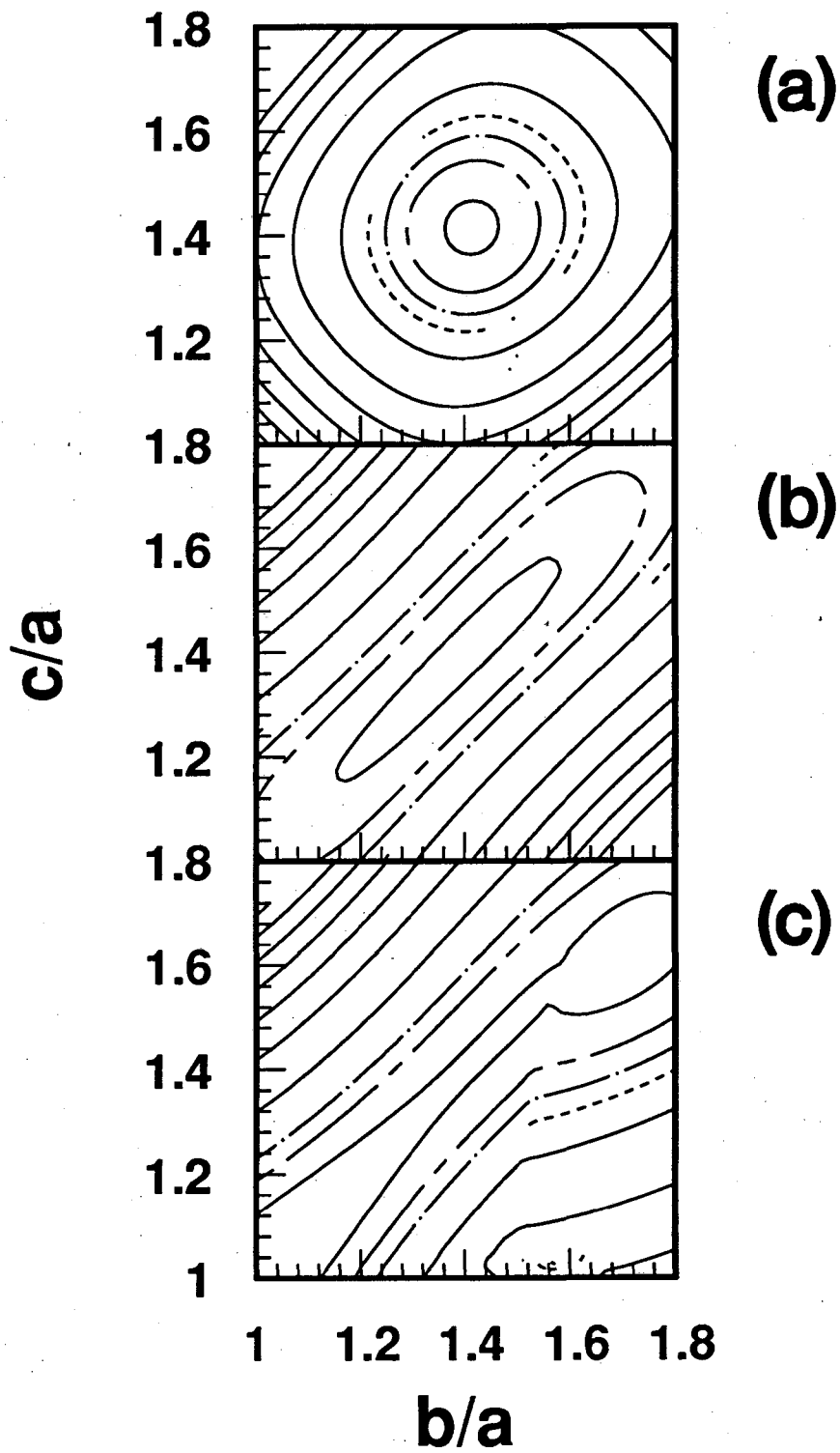


Figure 5.27

Figure 5.27: The energy contours in the $b/a, c/a$ space for (a) $V/V_0 = 1$, (b) $V/V_0 = 0.55$, and (c) $V/V_0 = 0.40$. The energies were minimized with respect to the internal parameter x . Two possible distortions from the B2 structure can be seen within this model. One corresponds to the new distortion we identified. The other corresponds to the previously assigned tetragonal distortion to CsI. Note the energy values on the contour are not equally spaced. Some contours have been removed for clarity as the density of the contours gets too high.

pressure from the B2 structure to the hcp structure. The experimental data below 40 GPa were fitted to a tetragonal cell with $b = c \geq a$ as explained before. Above 45 GPa, the orthorhombic structure was assumed. The theoretical calculation involved minimizing the total energy U with respect to b/a , c/a , and x for a series of volume fractions ($0.2 \leq V/V_0 \leq 1.0$). Two starting points with values $b/a = \sqrt{3}$, $c/a = \sqrt{8/3}$, $x = b/6$ and $b/a = c/a = 1$, $x = 0$ were used to find the two local minima. Fig. 5.28 compares the experimental data with the calculated path. Excellent agreement with the orthorhombic distortion is seen.

Good agreement is also found between the calculated lattice parameters and experimental values as a function of volume compression. The only noticeable difference is the onset of the phase transition. The above model with $n = 13$ gave a transition volume that is slightly too small, the calculated lattice spacings just next to the transition point therefore differ from the experimentally measured values but is in good agreement elsewhere. A better agreement near the onset of phase transition can be obtained with $n = 14$ in the model.³ Fig. 5.29 presents such a comparison. As one can see, the agreement between the calculated lattice spacings and experimentally measured values is excellent. The width of shading around each curve in Fig. 5.29 is proportional to the diffraction intensity. Only the scattering factor and multiplicity have been taken into account, therefore it is not to be compared directly with the experimentally observed intensity, rather, it is meant to show the relative intensities of the nearby lines. The extinction of certain lines in the low pressure cubic phase is clearly seen. This excellent agreement is in contrast to the results of the model calculation (Fig. 3 of [60]) and a first principle total energy calculation (Fig. 3 of [70]). In retrospect, these calculations were limited to the tetragonal distortion of the cubic cell which have now been shown to be an incorrect assignment, it is probably not surprising that good agreement should not be expected.

³With $n = 14$, a slightly larger transition volume than the experimental value is obtained.

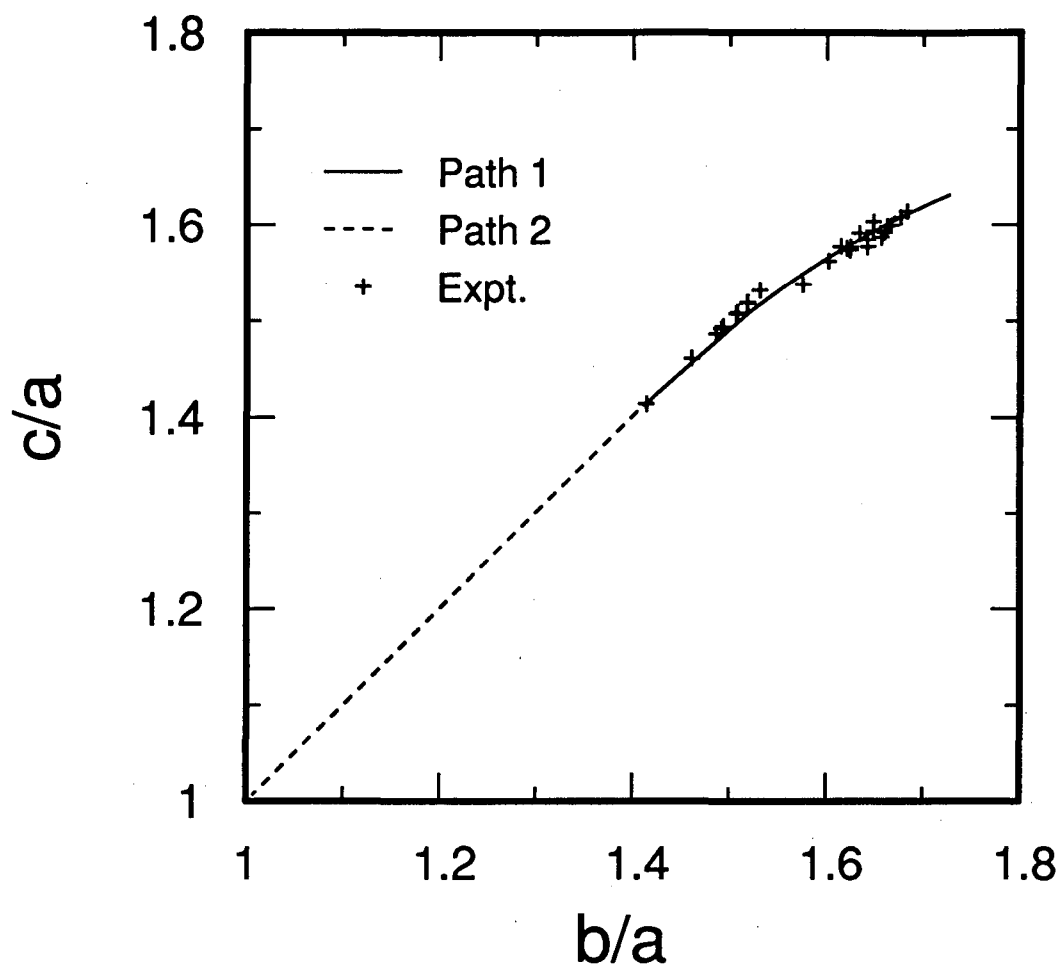


Figure 5.28: The structure phase transition path for CsI under compression in the compressional range $0.2 \leq V/V_0 \leq 1$ along with the observed experimental data. Path 1 corresponds to the orthorhombic distortion calculated in this study. Path 2 corresponds to the tetragonal distortion that was previously assigned to the high pressure phase of CsI.

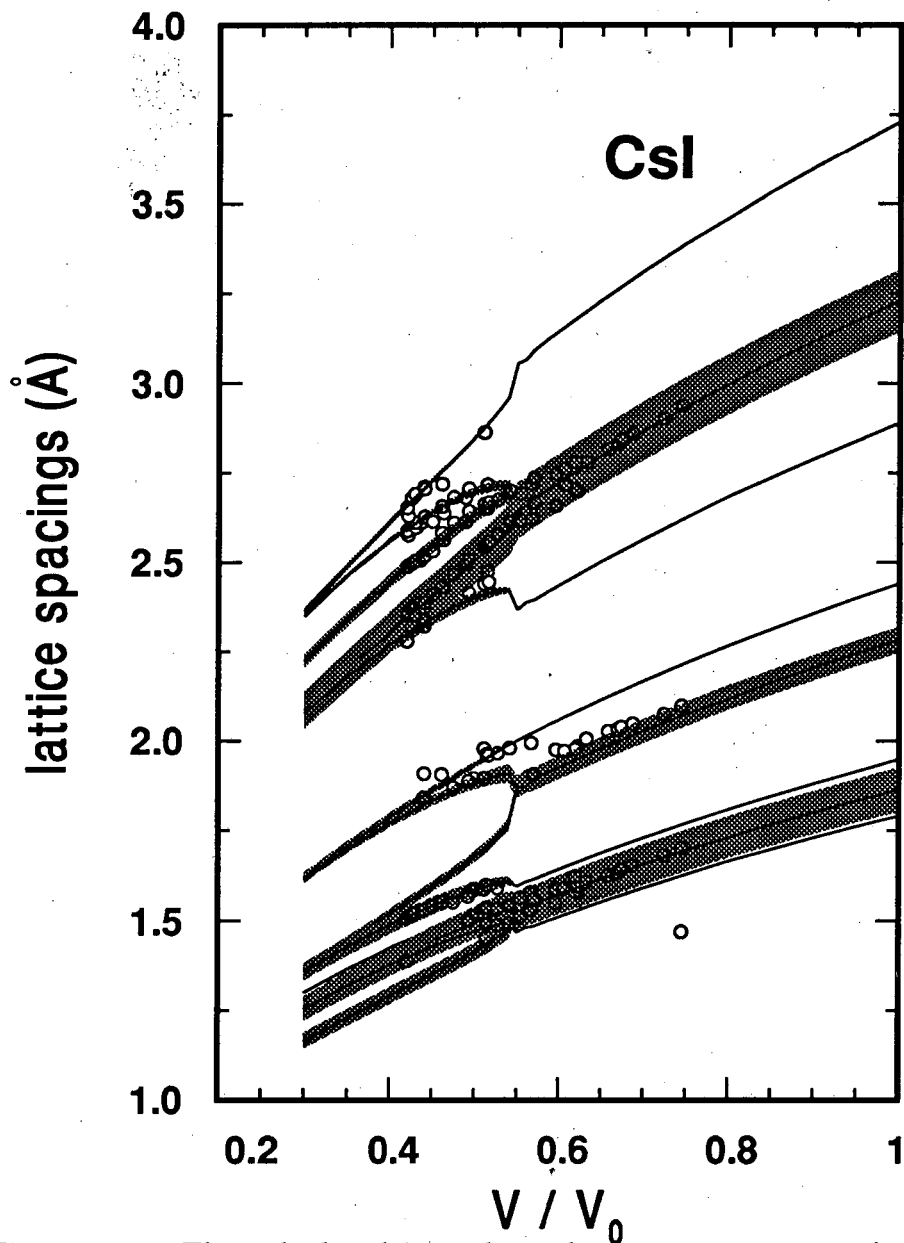


Figure 5.29: The calculated interplanar lattice spacings as a function of volume fraction for CsI under high pressure. The width of the shaded area around each curve is proportional to the product of the multiplicity factor and scattering factors for the given line calculated using the lattice parameters obtained in our model. The extinction of certain lines in the cubic phase is easily seen. The small discrepancies between the calculated and experimental values in the larger V/V_0 region are due to a distortion of the cubic structure prior to the phase transition which was not taken into account in the current model.

In the larger V/V_0 region, there are some small discrepancies between the calculated and experimental values. We believe that this is due to the tetragonal distortion prior to the phase transition which we have not taken into account in our model. The distortion is likely induced by the non-hydrostatic environment in the experiment. The non-hydrostatic environment can also produce preferred orientation in the sample. This is probably the reason why one of the diffraction line with reasonable calculated intensity but was not actually detected in the experiment.

5.6.4 The nature of the phase transition

In the above discussion, we assumed that the phase transition occurs when the static energies of the two phases become equal to each other at a given volume. Strictly speaking, this is not valid since there is the possibility of coexistence of the two phases at a given pressure and there might be a discontinuity in the volume. However, in the case where the phase transition is second or higher order, the difference disappears. We would like to show this is the case for the transitions we have considered.

In general, at low temperature, if the two phases involved in the phase transition can be described by two energy versus volume per atom curves, $U_1(v)$ and $U_2(v)$ as shown in Fig. 5.30 with the minimum of $U_1(v)$ lies below the minimum of $U_2(v)$, then $U_1(v)$ is the thermodynamically most stable phase. The proper description of the static compression process can then be described in the following manner. As the pressure is increased from 0, the volume decreases according to the requirement

$$P = -\frac{\partial U_1}{\partial v},$$

i.e. it will move along curve U_1 to where the slope of U_1 is equal to the pressure P . As the volume is further reduced, at a volume of v_1 the tangent for the curve U_1 at v_1 also becomes the tangent of curve U_2 at v_2 . At this point a first order phase transition occurs and yields a discontinuous change in the volume per atom. It is clear that the point where $U_1(v) = U_2(v)$ should lie above this common tangent, and with a

volume between v_1 and v_2 . There is no value v such that at v , $\frac{\partial U_1}{\partial v}|_v = \frac{\partial U_2}{\partial v}|_v$. In the case of second order phase transitions, there is no discontinuity in the transition volume, which implies that the slopes of the two curves at the phase transition point must be equal. The first order term in the expansion of the difference of the two energies near the transition volume must therefore vanish. In Fig. 5.31, we have plotted $\sqrt{|U_2(v) - U_1(v)|}$ as a function of v near the phase transition for both possible phase transitions. They can be fitted very well by two separate straight lines. This indicates that both phase transitions are of the second order and there is a discontinuity in the compressibility associated with the phase transition. This is in disagreement with the model calculation of Vohra *et al.*[60] who concluded the phase transition to the tetragonal structure was first order based on the apparent discontinuity of the axis ratio c/a as a function of v . However we note that since even for a second order phase transition there is a singularity in the lattice parameters. Because of this it is difficult if not impossible to show that these parameters are actually continuous.

The onset of transition to the orthorhombic structure is marked by a non-zero value of x , and simultaneously the change of the axis ratios. The change of x represents a sliding of alternate $\{110\}$ planes in the $[\bar{1}10]$ direction when referenced to the cubic B2 unit cell. This is probably the result of softening of the LA phonons at the M(1,1,0) point.

In a similar context, Lee and Ray[93] carried out a molecular dynamics study using three different potentials to study the bcc to hcp phase transition under high pressure for single element solids. For two of the potentials, the phase transition is observed. For the third, a transformation to a distorted structure was observed because the repulsive potential was too soft. Interestingly, with one of the potentials (modified Lennard-Jones), they observed a pretransformation which is rather similar to the orthorhombic phase that we have described, although not enough detail of the phase transition was analyzed in their study. It is unclear whether

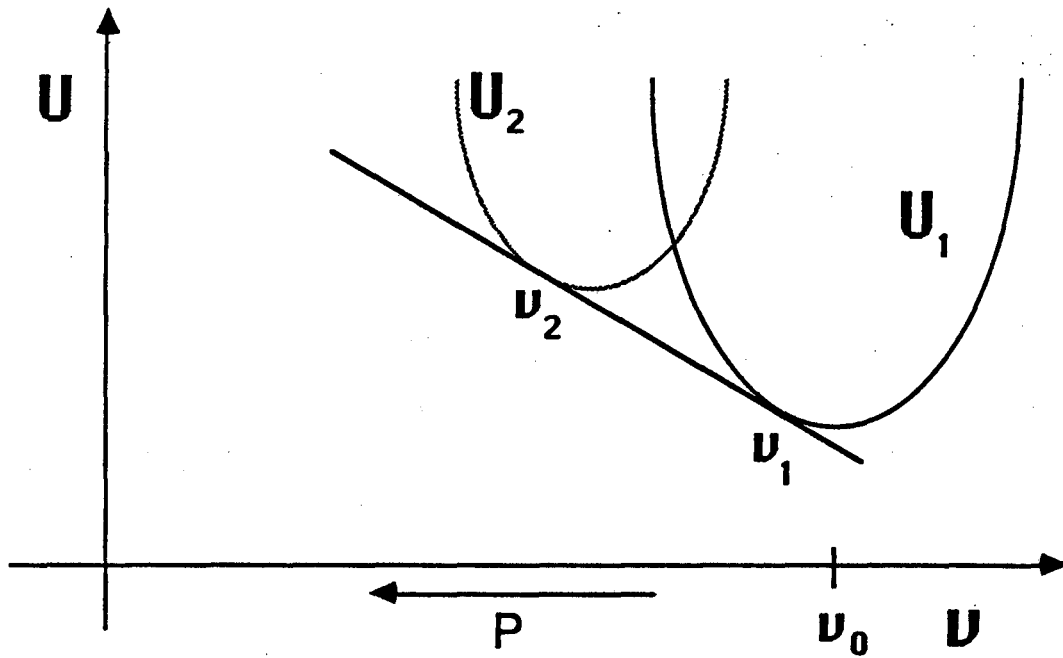


Figure 5.30: A first order phase transition usually involve a discontinuous change in volume.

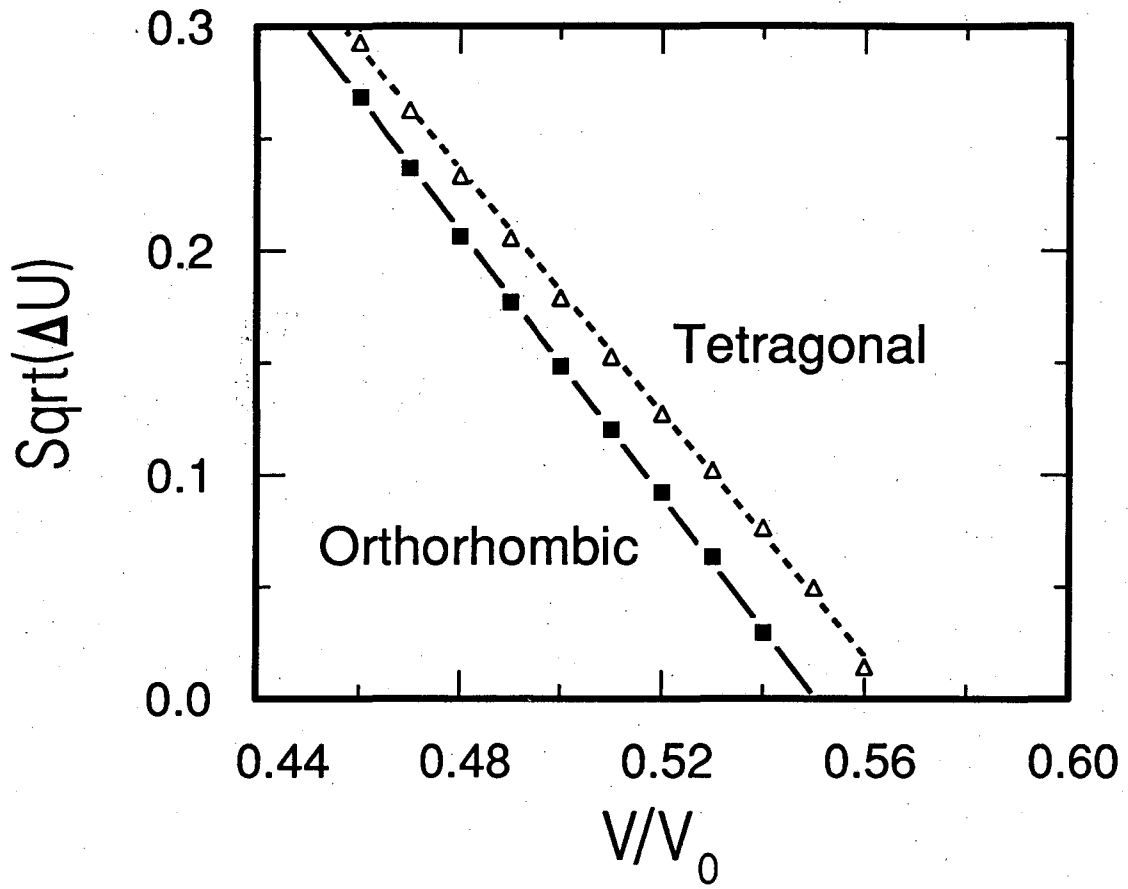


Figure 5.31: The square root of the energy difference between the two new structures and the original B2 structure as a function of volume fraction. In both cases, a straight line fits the data very well which indicates the phase transitions are of the second order.

this pretransformation was derived from the same mechanism as the orthorhombic structure observed in the present study.

In summary, we found a new possible distortion of the B2 structure of CsI under high pressure within a simple ionic pair potential model. This distortion is identical to the orthorhombic structure that we identified in the high pressure experimental studies of CsI. In this model calculation, this orthorhombic distortion has slightly higher energy than a tetragonal distortion with $c > b = a$ from the original cubic cell. The energy difference between the two likely new high pressure structures is very small. A small contribution from other interactions not considered here can easily stabilize one or the other. The calculated lattice parameters based on the orthorhombically distorted cell are in very good agreement with the experimental values. This suggests that a pair potential model is still useful in describing the crystal structure of solids under rather high pressures in some cases. However, a more exotic model is necessary to resolve the absolute stability of the orthorhombic phase with respect to the tetragonally distorted phase.

5.7 Conclusion

From our extensive high pressure diffraction data, both in hydrostatic and non-hydrostatic environment, the prototypical ionic solid CsI is shown to undergo through slightly different transformation sequences as the pressure is increased. For the non-hydrostatic compression case, a tetragonal distortion appears at a pressure as low as 15 GPa, and increases as the pressure is further raised. At a pressure about 40 GPa, it transforms continuously into an orthorhombic structure that is intermediate between the B2 and an hcp like lattice. There is no observable volume discontinuity associated with this phase transition. This orthorhombic structure is continuously transformed into an close packed hcp-like structure at ultra high pressure(> 200

GPa). For the case of quasi-hydrostatic compression, depends on the degree of the isotropy in the pressure environment, the distortion observed in the non-hydrostatic compression is greatly reduced, the cubic structure seems to be stable up to the phase transition pressure of 40 GPa. The difference between the non-hydrostatic equation of state and the hydrostatic equation of state is rather small but clearly distinct. With this observation, we can reconcile all previous static compression results.

The equation of state derived from the current studies agrees very well with that derived from theoretical calculations and dynamic compression studies. Therefore, a major inconsistency that existed among these previous studies is resolved.

The new compression data also allowed us to make comparisons of the quality of the existing equation of state formulations to described compression data to large compressions. We found that the Vinet equation of state gave the best description among the equation of state examined.

A simple ionic model is used to investigate the phase transition sequence. Despite the simplicity of the model, good agreement between the calculated and experimental results is obtained.

Appendix A

Equation of State Fitting Procedure

We present a new scheme for fitting an equation of state. It puts the error estimates of both the pressure and volume on an equal footing. Two methods of calculation are described. One of them is more exact but requires more computation, the other represents a good approximation to the more exact one but it is significantly faster. To illustrate the importance of proper weighting, an example is given where different error estimates are used in the fitting algorithm.

The experimentally measured equation of state data consisted of a series of pressure and volume data pairs (V_i, P_i) , with associated error estimates (σ_i^V, σ_i^P) . We would like to extract a few physical parameters (e.g. the zero pressure volume V_0 , the isothermal bulk modulus at zero pressure B_0 , and its pressure derivative B'_0 , etc.) by fitting these data to an empirical equation of state of the form $P = f(V, V_0, B, B')$.

In most cases where a least square fitting procedure is performed, the relative standard deviation of one physical variable is much less than that of the other, and therefore one normally considers the measured value of that variable as its true value. However, in the present equation of state measurements, it turns out that the standard deviations for pressure and volume do not satisfy the above condition. They need to be taken into account on an equal footing. For a linear model, the error on one variable can be transferred easily to the other, but it is unclear to what

extent the transfer will be valid for an highly non-linear model. This provides the motivation for the discussion below.

If the true values of volume and pressure under a given loading are V_i^t and P_i^t , and the measurement of V and P are independent and if the measured values obey normal distributions, then the probability of obtaining a pair of values (V_i, P_i) is

$$\exp\left(-\left(\frac{V_i - V_i^t}{\sigma_i^V}\right)^2\right) \cdot \exp\left(-\left(\frac{P_i - P_i^t}{\sigma_i^P}\right)^2\right). \quad (\text{A.1})$$

For all the experimental points, the possibility of obtaining the observed values is the product of the probabilities at all individual points,

$$P_{prob} = \prod_{i=1}^N \exp\left(-\left(\frac{V_i - V_i^t}{\sigma_i^V}\right)^2 - \left(\frac{P_i - P_i^t}{\sigma_i^P}\right)^2\right). \quad (\text{A.2})$$

If the true values obey an equation of the state of the form $P = f(V, V_0, B_0, B'_0)$, where one or more of the parameters are to be determined, then it is natural to require that their values give the largest value for the probability in equation (A.2). Therefore the problem of best fitting reduces to maximize P_{prob} with respect to the parameters in an appropriate way. Since neither the true value V_i^t or P_i^t is known at each data point, we must derive a way of estimating them. A most obvious way is to require that V_i^t and P_i^t give the maximum for the expression (A.1). This requires solving a two dimensional optimization problem at each data point. This is time consuming and impractical.

Fortunately, we can find a much more elegant method to approach this problem. If we consider the equal value contours of the expression (A.1), they are a series of ellipses centered at (V_i, P_i) , The probability decreases monotonically as the size of each ellipse increases. As shown in Fig. A.1.1, it is clear that the best estimate of V_i^t and P_i^t is achieved when the ellipse first touches the curve that represents the relation between V and P . With this in mind, the value of P_i^t can be calculated in

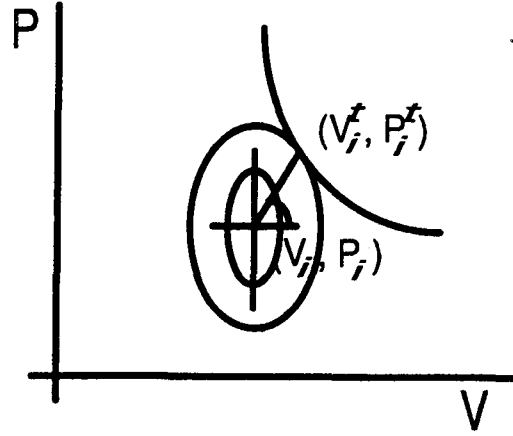


Figure A.1: Schematics for solving the least square fitting of a non-linear model.

the following manner. We represent the coordinates of the points on the contour by

$$V = V_i + k_i \sigma_i^V \cos \theta$$

$$P = P_i + k_i \sigma_i^P \sin \theta.$$

At the point where the contour touches the curve $P = f(V)$, the slope of the curve and contour must be the same. This can be used to find the value of θ easily,

$$-\frac{\sigma_i^P}{\sigma_i^V} \cot \theta = \frac{dP}{dV} \quad (\text{A.3})$$

the value of k_i can be determined by the requirement that $P_i^t = f(V_i^t)$, *i.e.*

$$P_i + k_i \sigma_i^P \sin \theta = f(V_i + k_i \sigma_i^V \cos \theta),$$

from this and equation (A.3), we can solve for both θ and k_i . It is now clear how we could achieve our goals.

We start with a set of initial parameters and the experimental data. At each experimental point, we find the value k_i , then the total probability in formula (A.2) as $\exp(-\sum_{i=1}^N k_i^2)$. What's left is to vary the parameters until the maximum is found.

There is a drawback in such an approach, however. In cases there are many data points, this algorithm requires a fair amount of computing time. This is due to the fact that for each evaluation of the formula (A.2), we need to solve for k_i for each of the data points and this increases significantly the computing time. In these cases, a less computation intensive method is desired. The following approximate method is developed for this purpose. First, we pick θ such that

$$\left| \frac{V_i - V_i^t}{\sigma_i^V} \right| = \left| \frac{P_i - P_i^t}{\sigma_i^P} \right|,$$

and after solving for k_i initially, we then assume that the true value $V_i^t = V_i + k_i \sigma_i^V \cos \theta$. At this point, we use the standard least square procedure to obtain the optimized parameters. These values are used to recalculate k_i 's and the above process continues until convergence is achieved. This procedure is significantly faster and gives very good results compared with the first approach. So this method is used throughout the work presented here. In this case, the normally defined χ^2 is still applicable.

To illustrate the effect of error estimation on the results of fitting, we considered the data in table A.1.

Three fitting procedures were performed. One assumes the error estimates as given. The second one assumes the error estimate on pressure is 1% of the given value. The last one assumes the error estimate on volume is 1% of the given value. The results are presented in table A.2. It is clear that proper weighting is necessary in order to get accurate values for the parameters.

Table A.1: The pressure volume data used in the fitting procedures

Pressure (GPa)	σ^P (GPa)	V/V_0	$\sigma^{(V/V_0)}$
4.4	0.03	.9731	.0004
6.1	0.3	.9759	.00181
9.5	0.2	.9626	.00066
12.5	0.4	.9441	.00184
18.8	1.3	.9190	.00256
20.3	1.0	.9095	.00044
28.3	0.6	.8950	.00057
31.7	1.8	.8781	.00070
36.4	1.4	.8635	.00138
39.8	1.7	.8545	.00008
48.4	1.3	.8374	.00046
48.8	2.2	.8365	.00099
54.9	.8	.8193	.00068
60.3	1.0	.8128	.00145
63.5	1.5	.8086	.00122
70.1	2.2	.7962	.00032

Table A.2: Fitted parameters for different error estimation methods

	B_0	B'_0	χ^2
case 1	161.4	5.94	106
case 2	163.5	5.77	379
case 3	154.5	6.37	353

Bibliography

- [1] A. P. Jephcoat, H. K. Mao, and P. M. Bell, "Operation of the megabar diamond-anvil cell", in *Hydrothermal Experimental Techniques*, edited by G. C. Ulmer and H. L. Barnes, (Wiley Interscience, New York, 1987).
- [2] M. Seal, "Diamond anvils", *High Temp.-High Press.*, **16**, 573-579(1984).
- [3] M. Seal, "Diamond anvil technology", in *High Pressure Research in Mineral Physics*, edited by M. H. Manghnani and Y. Syono, 35-40(1987).
- [4] J.E. Field, ed., *The properties of diamond*, (Academic, London, 1979).
- [5] C.E. Weir, E. R. Lippincott, A. van Valkenburg, E. N. Bunting, "Infrared studies in the 1 to 15-micron region to 30000 atmospheres", *J. Res. Nat. Bur. Stand., Sect. A*, **63**, 55-62(1959).
- [6] H. K. Mao and P. M. Bell, "Design of a diamond-windowed, high pressure cell for hydrostatic pressures in the range 1 bar to 0.5 Mbar", *Year Book, Carnegie Inst. Washington*, **74**, 402-405(1975).
- [7] C. J. Piermerini and S. Block, "An ultra high pressure diamond-anvil cell and several semi-conductor phase transition pressures in relation to the fixed point pressure scale", *Rev. Sci. Instrum.*, **46**, 973-979(1975).
- [8] A. Jayaraman, "Diamond anvil cell and high pressure physical investigations", *Rev. Mod. Phys.*, **55**, 65(1983).

- [9] H. K. Mao, R. J. Hemley, Y. Wu, A. P. Jephcoat, L. W. Finger, C. S. Zha and W. A. Bassett, "High-pressure phase diagram and equation of state of solid helium from single-crystal x-ray diffraction to 23.3 GPa", *Phys. Rev. Lett.*, **60**, 2649(1988).
- [10] R. L. Mills, D. H. Liebenberg, J. C. Bronson and L. C. Schmidt, "Procedure for loading diamond cells with high-pressure gas", *Rev. Sci. Instrum.*, **51**, 891-895(1980).
- [11] J. D. Barnett, S. Block, G. J. Piermerini, "An optical fluorescence method for quantitative pressure measurement in the diamond anvil cell", *Rev. Sci. Instrum.*, **44**, 1-9(1973).
- [12] H. K. Mao and P. M. Bell, "Design and varieties of the megabar cell", *Year Book, Carnegie Inst. Washington*, **77**, 904-913(1978).
- [13] H. K. Mao, J. Xu and P. M. Bell, "Calibration of the ruby pressure gauge to 800 kbar under quasihydrostatic conditions", *J. Geophys. Res.*, **91**, 4673-4676(1986).
- [14] P. M. Bell, H. K. Mao and K. Goettel, "Ultrahigh pressure: beyond 2 megabars and the ruby fluorescence scale", *science*, **226**, 542(1984).
- [15] P. M. Bell, J. A. Xu and H. K. Mao, "Static compression of gold and copper and calibration of the ruby pressure scale to pressures to 1.8 megabars", in *Shock Waves in Condensed Matter*, Y. M. Gupta, Ed.(Plenum, New York, 1986).
- [16] H. K. Mao, C. G. Hadidiacos, P. M. Bell and K. Goettel, "Automated system for heating and for spectral measurements in the diamond-window, high-pressure cell", *Year Book, Carnegie Inst. Washington*, **82**, 421-424(1983).
- [17] N. C. Holmes, J. A. Moriarty, G. R. Gathers, and W. J. Nellis, "The Equation of State of Platinum to 660 GPa (6.6 Mbar)", *J. Appl. Phys.*, **66**, 2962(1989).

- [18] J. D. Jackson, *Classical Electrodynamics*, 2nd edition, (Jonh Wiley & Sons, New York, 1976).
- [19] S. Gasiorowicz, *Quantum Physics*, (Jonh Wiley & Sons, New York, 1974).
- [20] J. H. Hubbell, Wm. J. Veigele, E. A. Briggs, R. T. Brown, D. T. Cromer, and R. J. Howerton, "Atomic Form Factors, Incoherent Scattering Functions, and Photon Scattering Cross Sections", *J. Phys. Chem. Ref. Data*, **4**, 471(1975).
- [21] L. Kissel, R. H. Pratt, and S. C. Roy, "Rayleigh scattering by neutral atoms, 100 eV to 100 MeV", *Phys. Rev. A*, **22**, 1970(1980).
- [22] B. E. Warren, *X-Ray Diffraction*, (Addison-Wesley, Reading, Mass., 1969).
- [23] B. Buras and L. Gerward, "Relations between integrated intensities in crystal diffraction Methods for X-ray and Neutrons", *Acta. Cryst. A*, **31**, 372(1975).
- [24] D. W. Aitken, "Recent advances in x-ray detection technology", *IEEE Trans. Nucl. Sci.*, **15**, 10(1968).
- [25] B. Buras, N. Niimura, and J. Staun Olsen, "Optimum Resolution in X-ray Energy-Dispersive Diffractometry", *J. Appl. Cryst.*, **11**, 137(1978).
- [26] M. A. Baublitz, Jr., V. Arnold, and A. L. Ruoff, "Energy Dispersive X-ray Diffraction from High Pressure Polycrystalline Specimens Using Synchrotron Radiation", *Rev. Sci. Instrum.*, **52**, 1616(1981).
- [27] K. E. Brister, Y. K. Vohra, and A. L. Ruoff, "Microcollimated energy-dispersive x-ray diffraction apparatus for studies at megabar pressures with a synchrotron source", *Rev. Sci. Instrum.*, **57**, 2560(1986).
- [28] H. K. Mao and R. J. Hemley, "Optical studies of hydrogen above 200 gigapascals: evidence for metalization by band overlap", *Science*, **244**, 1462(1989).

- [29] J. A. Xu, H. K. Mao and P. M. Bell, "High-pressure ruby and diamond fluorescence: observation at 0.21 and 0.55 terapascal", *Science*, **232**, 1404(1986); W. C. Moss, J. O. Hallquist, R. Reichlin, K. A. Goettel and S. Martin, "Finite element analysis of the diamond anvil cell: achieving 4.6 Mbar", *Appl. Phys. Lett.*, **48**, 1258(1986).
- [30] SSRL user's guide, Oct. 1988.
- [31] K. Saitoh, K. Oishi, A. Iida, "X-ray microbeam by multilayer zone plate", Photon Factory Activity Report, **7**, 147(1989).
- [32] K. Saitoh, K. Oishi, A. Iida, "Characterization of sliced multilayer zone plates for hard x rays", *Rev. Sci. Instrum.*, **60**, 1519(1989).
- [33] H. H. Johann, *Z. Phys.*, **69**, 185(1931).
- [34] T. Johansson, *Z. Phys.*, **82**, 507(1933).
- [35] A. Guinier and G. Tennevin, *Acta Cryst.*, **2**, 133(1949).
- [36] A. Guinier and G. Tennevin, *Progress in Metal Physics*, **2**, 177. (New York: Interscience, 1950).
- [37] P. Kirkpatrick and A. V. Baez, "Formation of optical images by x-rays", *J. Opt. Soc. Am.*, **39**, 766(1948).
- [38] T. W. Barbee and D. C. Keith, "Layered synthetic microstructures - application as x-ray dispersion elements", Stanford SSRL report No. 79/02, 185(1979).
- [39] E. Spiller, "Evaporated multilayer dispersion elements for soft x-rays", in *Low Energy X-Ray Diagnostics*, (AIP, NY 1981), edited by D. T. Attwood and B. L. Henke.
- [40] J. R. Chelikowsky, "Nonclassical origin of the rocksalt-cesium chloride structure transition", *Phys. Rev. Lett.*, **58**, 714(1987).

- [41] C. Kittel, *Introduction to Solid State Physics*, 5th ed.(Wiley, New York, 1976).
- [42] J. W. Edington, *Practical Electron Microscopy in Material Science*, (Von Nostrand Reinhold Co., New York, 1976).
- [43] A. P. Jephcoat, H. K. Mao, L. W. Finger, D. E. Cox, R. J. Hemley, and C. S. Zha, "Pressure-induced structural phase transitions in solid Xenon", *Phys. Rev. Lett.*, **59**, 2670(1987).
- [44] R. Reichlin, K. E. Brister, A. K. McMahan, M. Ross, S. Martin, Y. K. Vohra, and A. L. Ruoff, "Evidence for the insulator-metal transition in Xenon from optical, x-ray, and band-structure studies to 170 GPa", *Phys. Rev. Lett.*, **62**, 669(1989).
- [45] K. A. Goettle, J. H. Eggert, and I. F. Silvera, and W. C. Moss, "Optical evidence for the metallization of Xenon at 132(5) GPa", *Phys. Rev. Lett.*, **62**, 665(1989).
- [46] T. A. Grzybowski and A. L. Ruoff, "Band-overlap metallization of BaTe", *Phys. Rev. Lett.*, **53**, 489(1984).
- [47] P. W. Bridgeman, *Proc. Am. Acad. Arts Science*, **74**, 21(1940).
- [48] P. W. Bridgeman, *Proc. Am. Acad. Arts Science*, **76**, 1(1945).
- [49] S. N. Vaidya and G. C. Kennedy, "Compressibility of 27 halides to 45 kbar", *J. Phys. Chem. Solids.*, **32**, 951(1971).
- [50] D. E. Hammond, thesis, University of Rochester, Rochester, New York, 1969.
- [51] Bassette, in *Advances in High-pressure Research*, edited by R. H. Wentorf, Jr. (Academic, New York, 1974), Vol. 4.
- [52] K. Asaumi, "Pressure-induced successive phase transitions in CsI and its equation of state in relation to metallization", *Phys. Rev.*, **B 29**, 1118(1984).

- [53] E. Knittle and R. Jeanloz, "Structural and bonding changes in cesium iodide at high pressures", *Science*, **223**, 53(1984).
- [54] E. Knittle and R. Jeanloz, "High-pressure x-ray diffraction and optical absorption studies of CsI", *J. Phys. Chem. Solid*, **46**, 1179(1985).
- [55] T.-L. Huang and A. L. Ruoff, "Equation of state and high-pressure phase transition of CsI", *Phys. Rev.*, B **29**, 1112(1984).
- [56] T.-L. Huang and A. L. Ruoff, "High pressure x-ray diffraction study on cesium iodide", *Mater. Res. Soc. Symp. Proc.*, **22**, 11(1984).
- [57] T.-L. Huang, K. E. Brister, and A. L. Ruoff, "Pressure-induced structural transition of CsI and CsBr", *Phys. Rev.*, B **30**, 2968(1984).
- [58] A. N. Zisman, I. V. Aleksandrov, and S. M. Stishov, "X-ray study of equation of state of solid xenon and cesium iodide at pressures up to 55 GPa", *JETP lett.*, **40**, 1029(1984).
- [59] A. N. Zisman, I. V. Aleksandrov, and S. M. Stishov, "X-ray study of equation of state of solid xenon and cesium iodide at pressures up to 55 GPa", *Phys. Rev. B*, **32**, 484(1985).
- [60] Y. K. Vohra, S. J. Duclos, and A. L. Ruoff, "Instability of the CsCl structure in ionic solids at high pressure", *Phys. Rev. Lett.*, **54**, 570(1985).
- [61] Y. K. Vohra, K. E. Brister, S. T. Weir, S. J. Duclos, and A. L. Ruoff, "Crystal structures at megabar pressures determined by use of the Cornell synchrotron source", *Science*, **231**, 1136(1986).
- [62] R. H. Christian, Ph.D thesis, University of California, 1957.
- [63] L. V. Al'tshuler, M. M. Pavovskii, L. V. Kuleshova, and G. V. Simakov, "Investigation of alkali-metal halides at high pressures and temperatures produced by

- shock compression”, *Fiz. Tverd. Tela (Leningrad)*, **5**, 279(1962). [*Sov. Phys. Solid State*, **5**, 203 (1963)]
- [64] M. N. Pavlovskii, V. Ya. Vashchenko, and G. V. Simakov, “Equation of state for cesium iodide”, *Fiz. Tverd. Tela (Leningrad)*, **7**, 972(1965). [*Sov. Phys. Solid State*, **7**, 72(1965).].
- [65] H. B. Radousky, M Ross, A. C. Mitchell, and W. J Nellis, “Shock temperatures and melting in CsI”, *Phys. Rev. B*, **31**, 1457(1985).
- [66] C. A. Swenson, J. W. Shaner, and J. M. Brown, “Hugoniot overtake sound-velocity measurements on CsI”, *Phys. Rev. B*, **34**, 7924(1986).
- [67] J. Aidun and M. S. T. Bukowinski, “First-principles calculation of the insulator-to-metal transition pressure in CsI”, *Solid State Commun.*, **47**, 855(1983).
- [68] J. Aidun, M. S. T. Bukowinski, and M. Ross, “Equation of state and metallization of CsI”, *Phys. Rev. B*, **29**, 2611(1984).
- [69] N. E. Christensen and S. Satpathy, “Pressure induced cubic to tetragonal transition in CsI”, *Phys. Rev. Lett.*, **55**, 600(1985).
- [70] S. Satpathy, N. E. Christensen, and O. Jepsen, “Metallization of CsI under pressure: Theoretical results”, *Phys. Rev. B*, **32**, 6793(1985).
- [71] K. Asaumi and Y. Kondo, “Effect of very high pressure on the optical absorption spectra in CsI”, *Solid State Commun.*, **40**, 715(1981).
- [72] J. P. Itie, A. Polian, and J.M. Besson, “Optical-absorption edge of CsI up to 58 GPa”, *Phys. Rev. B*, **30**, 2309(1984).
- [73] I. N. Makarenko, A. F. Goncharov, and S. M. Stishov, “Optical absorption spectra of cesium iodide (CsI) at pressures up to 60 GPa”, *Phys. Rev. B*, **29**, 6018(1984).

- [74] Y. K. Vohra, S. T. Weir, K. E. Brister, and A. L. Ruoff, "Band overlap metal-
lization of cesium iodide", *Phys. Rev. Lett.*, **55**, 977(1985).
- [75] Q. Williams and R. Jeanloz, "Measurements of CsI band-gap closure to 93
GPa", *Phys. Rev. Lett.*, **56**, 163(1986).
- [76] R. Reichlin, M. Ross, S. Martin, and K. A. Goettel, "metallization of CsI",
Phys. Rev. Lett., **56**, 2858(1986).
- [77] Q. Williams and R. Jeanloz, "Pressure induced disproportionation of cesium
iodide", *Phys. Rev. Lett.*, **59**, 1132(1987).
- [78] R. J. Hemley, C. S. Zha, A. P. Jephcoat, H. K. Mao, L. W. Finger, and
D. E. Cox, "X-ray diffraction and equation of state of solid neon to 110 GPa",
Phys. Rev. B, **39**, 11820(1989).
- [79] I. V. Aleksandrov, A. N. Zisman, and S. M. Stishov, "An investigation of the
equation of state of the isoelectronic substances CsI-Xe and RbBr-Kr: phase
transitions in CsI and RbBr", *Sov. Phys. JETP*, **65**, 371(1987).
- [80] I. V. Aleksandrov, A. F. Goncharov, I. N. Makarenko and S. M. Stishov, "New
data on the equation of state and the phase transitions in cesium iodide",
Preprint.
- [81] F. D. Murnaghan, *Proc. Nat. Acad. Sci.*, **30**, 244(1944).
- [82] F. Birch, "Finite elastic strain of cubic crystals", *Phys. Rev.*, **71**, 801(1947).
- [83] F. Birch, "Finite strain isotherm and velocities for single crystal and polycrys-
talline NaCl at high pressures and 300 K", *J. Geophys. Res.*, **83**, 1257(1978).
- [84] P. Vinet, J. Ferrante, J. R. Smith, and J. H. Rose, "A universal equation of
state for solids", *J. Phys. C*, **19**, L467(1986).
- [85] P. Vinet, J. R. Smith, J. Ferrante, and J. H. Rose, "Temperature effects on the
universal equation of state of solids", *Phys. Rev. B*, **35**, 1945(1987).

- [86] P. Vinet, J. Ferrante, J. H. Rose, and J. R. Smith, "Compressibility of solids", *J. Geophys. Res.*, **92**, 9319(1987).
- [87] G. R. Barsch, Z. P. Chang, in *Accurate Characterization of the High Pressure Environment*, edited by E. C. Lloyd, National Bureau of Standards Publication No. 326(U.S. GPO, Washington, D.C., 1971), p. 173.
- [88] A. A. Maradudin, E. W. Montroll, and C. H. Weiss, *Theory of Lattice Dynamics in the Harmonic Approximation*, 2nd ed.(Academic Press, New York, 1971).
- [89] K. Herzfeld, "On atomic properties which make an element a metal", *Phys. Rev.*, **29**, 701(1927).
- [90] *CRC Handbook of Chemistry and Physics*, 64th ed. (CRC press, 1988).
- [91] J. M. Ziman, *Principle of the Theory of Solids*, 2nd edition, (Cambridge University Press, Cambridge, 1979), p. 39.
- [92] M. J. Sinnott, *The Solid State for Engineers*, (John Wiley & Sons, New York, 1958), p. 146.
- [93] K. Y. Lee and J. R. Ray, "Mechanism of pressure-induced martensitic phase transformations: A molecular-dynamics study", *Phys. Rev. B*, **39**, 565(1989).

LAWRENCE BERKELEY LABORATORY
UNIVERSITY OF CALIFORNIA
INFORMATION RESOURCES DEPARTMENT
BERKELEY, CALIFORNIA 94720